1   **Complementary environmental analysis and functional characterization of a**

2   **plastid diatom lower glycolytic-gluconeogenesis pathway**

3

4   **Short Title: Probing Diatom Chloroplast Lower Glycolysis**

5

6   Richard G. Dorrell[1,2,3], Youjun Zhang[4,5,6], Yue Liang[7,8], Nolwenn Gueguen[9], Tomomi

7   Nonoyama[1,10], Dany Croteau[11], Mathias Penot[1,2,3], Sandrine Adiba[1], Benjamin

8   Bailleul[11], Valérie Gros[9], Juan José Pierella Karlusich[1,2,12], Nathanaël Zweig[1,2],

9   Alisdair R. Fernie[4,5], Juliette Jouhet[9], Eric Maréchal[9] and Chris Bowler[1,2]

10

11   [1]Institut de Biologie de l'ENS (IBENS), Département de Biologie, École Normale

12   Supérieure, CNRS, INSERM, Université PSL, 75005 Paris, France

13   [2]CNRS Research Federation for the study of Global Ocean Systems Ecology and

14   Evolution, FR2022/Tara Oceans GOSEE, 3 rue Michel-Ange, 75016 Paris, France

15   [3]Laboratory of Computational and Quantitative Biology (LCQB), Institut de Biologie

16   Paris-Seine (IBPS), CNRS, INSERM, Sorbonne Université, 75005 Paris, France

17   [4]Center of Plant Systems Biology and Biotechnology, 4000 Plovdiv, Bulgaria

18   [5]Max-Planck-Institute of Molecular Plant Physiology, Am Mühlenberg 1, 14476,

19   Potsdam-Golm, Germany

20   [6]Key Laboratory of Seed Innovation, Institute of Genetics and Developmental

21   Biology, Chinese Academy of Sciences, Beijing, China

22   [7]Center of Deep Sea Research, Institute of Oceanology, Center for Ocean Mega-

23   Science, Chinese Academy of Sciences, Qingdao 266071, China

24   [8]Laboratory for Marine Mineral Resources, Pilot National Laboratory for Marine

25   Science and Technology, Qingdao 266237, China

26   [9]Laboratoire de Physiologie Cellulaire et Végétale, CNRS, Univ. Grenoble Alpes,

27   CEA, INRAE, IRIG, 17 rue des Martyrs, 38000 Grenoble, France

28   [10]Division of Biotechnology and Life Science, Institute of Engineering, Tokyo

29   University of Agriculture and Technology, 2-24-16, Naka-cho, Koganei, Tokyo 184-

30   8588, Japan

31   [11]Institut de Biologie Physico-Chimique (IBPC), Université PSL, 75005 Paris, France

32   [12]Present address: FAS Division of Science, Harvard University, Cambridge, MA,

33   USA

34

35 The authors responsible for distribution of materials integral to the findings presented

36 in this article in accordance with the policy described in the Instructions for Authors

37 (https://academic.oup.com/plcell/pages/General-Instructions) are: Richard G. Dorrell

38 (richard.dorrell@sorbonne-universite.fr) and Chris Bowler (cbowler@bio.ens.psl.eu)

39

40 **Abstract**

41

42 **Organic carbon fixed in chloroplasts through the Calvin Cycle can be diverted**

43 **towards different metabolic fates, including cytoplasmic and mitochondrial**

44 **respiration; gluconeogenesis; and synthesis of diverse plastid metabolites via**

45 **the pyruvate hub. In plants, pyruvate is principally produced via cytoplasmic**

46 **glycolysis, although a plastid-targeted lower glycolytic pathway is known in**

47 **non-photosynthetic tissue. Here, we characterize a lower plastid glycolytic-**

48 **gluconeogenesis pathway in diatoms, ecologically important marine algae**

49 **distantly related to plants. We show that two reversible enzymes required to**

50 **complete diatom plastid glycolysis-gluconeogenesis, Enolase and PGAM (*bis-***

51 **phospho-glycerate mutase), originated through duplications of mitochondria-**

52 **targeted respiratory isoforms. Through CRISPR-Cas9 mutagenesis, integrative**

53 **'omic analyses, and measured kinetics of expressed enzymes in the diatom**

54 ***Phaeodactylum tricornutum*, we present evidence that this pathway diverts**

55 **plastid glyceraldehyde-3-phosphate into the pyruvate hub, and may also**

56 **function in the gluconeogenic direction. Considering experimental data, we**

57 **show that this pathway has different roles dependent in particular on day**

58 **length and environmental temperature, and show that it is expressed at**

59 **elevated levels in high latitude oceans where diatoms are abundant. Our data**

60 **provide evolutionary, meta-genomic and functional insights into a poorly**

61 **understood yet evolutionarily recurrent plastid metabolic pathway.**

62

63 **Keywords:** chloroplast; *Tara* Oceans; meta-genomics; post-endosymbiotic evolution;

64 plastid-mitochondria crosstalk; RNAseq; GC and LC-MS; photophysiology

65

66 **Introduction**

67

68   Each year, over 250 gigatonnes of atmospheric carbon dioxide is assimilated through

69   photosynthesis, with effectively equal contributions from terrestrial plants and aquatic

70   algae (Friedlingstein, Jones et al. 2022). This activity is essential for maintaining

71   planetary climate homeostasis, supporting the entire Earth ecosystem. Carbon

72   assimilated through photosynthesis via the Calvin cycle is diverted into multiple

73   metabolic fates (Raines 2003). In plants, these include gluconeogenesis of glucose-

74   6-phosphate directly in plastids (or chloroplasts), which can then be used in leaf

75   tissue for starch storage (Scialdone, Mugford et al. 2013). Additional metabolites

76   including fatty acids and lipids, amino acids, chlorophyll and carotenoid pigments are

77   synthesised directly in the plastid (Tanaka and Tanaka 2007, Bromke 2013,

78   Maréchal and Lupette 2020, Bai, Cao et al. 2022) (**Fig. 1A**). Many of these plastid

79   metabolic reactions utilize pyruvate, or its adjacent metabolic precursor phospho-

80   *enol*-pyruvate (or PEP), and are referred to collectively as the pyruvate hub (Shtaida,

81   Khozin-Goldberg et al. 2015). In addition, plant photosynthate is exported from the

82   plastids to the cytosol for subsequent glycolysis and respiration in the mitochondria

83   (Moog, Rensing et al. 2015), or for transport to non-photosynthetic tissue (Carrera,

84   George et al. 2021) (**Fig. 1A**).

85

86   Plants are classically thought to generate PEP and pyruvate through glycolysis in the

87   cytoplasm, then reimport these metabolites into the plastids (**Fig. 1A**) (Moog,

88   Nozawa et al. 2020). Alongside this, certain plants may synthesize pyruvate hub

89   substrates directly from the Calvin cycle inside the plastid. This conversion is

90   performed by two enzymes, plastid-targeted phospho-glycerate mutase and enolase

91   (henceforth referred to as cpPGAM and epEnolase), which allow the conversion of

92   1,3-bis-phosphoglycerate from the Calvin cycle to PEP (**Fig. 1A**) (Raines 2003,

93   Andriotis, Kruger et al. 2010). Both Enolase and PGAM have been shown

94   experimentally to be fully reversible enzymes, with bidirectional functions that we

95   henceforth refer to as glycolysis-gluconeogenesis, contrasting with glycolysis and

96   gluconeogenesis to signify enzymatic activities in one direction only (Sutherland,

97   Posternak et al. 1949). Documented plant cpEnolase and cpPGAM enzymes are

98   associated with non-photosynthetic tissues such as seeds and roots (Prabhakar,

99   Löttgert et al. 2009, Fukayama, Masumoto et al. 2015, Troncoso-Ponce, Rivoal et al.

100   2018). *Arabidopsis thaliana* cpEnolase and cpPGAM knockout lines have limited

101   phenotypes under replete growth conditions (Prabhakar, Löttgert et al. 2009,

102   Andriotis, Kruger et al. 2010, Anoman, Flores-Tornero et al. 2016), raising questions

103   of their overall function.

104

105   Diatoms are a eukaryotic algal group that is distantly related to plants, with over one

106   billion years of evolutionary separation between the nuclear and mitochondrial

107   genomes of each species (Nonoyama, Kazamia et al. 2019, Strassert, Irisarri et al.

108   2021). In contrast to the primary plastids of plants, surrounded by two membranes

109   and of bacterial origin, diatoms possess complex plastids surrounded by four

110   membranes and derived from a eukaryotic red alga, which is likewise ancient

111   (Nonoyama, Kazamia et al. 2019, Liu, Storti et al. 2022). Diatoms are extraordinarily

112   successful in the modern ocean, comprising nearly half of total algal abundance e.g.,

113   in environmental sequence data from the *Tara* Oceans expedition (Malviya, Scalco et

114   al. 2016, Behrenfeld, Halsey et al. 2021). Diatoms are particularly abundant in high-

115   latitude and temperate oceans (i.e., the North Atlantic, North Pacific and Southern

116   Oceans) that are characterised by stresses including low temperatures and

117   elongated photoperiods (long days in the summer, and long nights in the winter)

118   (Gilbertson, Langan et al. 2022, Joli, Concia et al. 2024). Previous studies,

119   particularly of the transformable coastal and mesophilic species *Phaeodactylum*

120   *tricornutum*, have identified multiple strategies that allow diatoms to tolerate photo-

121   stress, including complex inter-organelle metabolite trafficking (Bailleul, Berne et al.

122   2015, Broddrick, Du et al. 2019, Smith, Dupont et al. 2019) and extensive

123   photoprotective capabilities (reviewed in (Lepetit, Campbell et al. 2022). These data

124   are further supported by extensive environmental (meta-genomic) sequence data

125   such as those of the *Tara* Oceans mission. While the data from these studies relate

126   fundamentally to different species to *Phaeodactylum* (i.e., open-ocean diatoms,

127   including from polar habitats) they may allow us to understand how individual diatom

128   chloroplast proteins function at ecosystem scales, as well as under laboratory

129   conditions (Kazamia, Sutak et al. 2018, Liu, Storti et al. 2022).

130

131   Diatom carbon metabolism is highly different to that of plants (Kroth, Chiovitti et al.

132   2008). Differences include the storage of sugars in cytoplasmic vacuoles (as

133   chrysolaminarin) as opposed to plastidial starch, and the synthesis of most lipid

134   groups (e.g., galactolipids and part of triacylglycerol pathway) directly in the plastid

135   (Zhu, Shi et al. 2016, Huang, Pan et al. 2024). Diatom plastids furthermore possess

4

136   no known plastid hexose phosphate transporters, which in plants are implicated in

137   plastidial sugar import in storage tissue. Diatoms are instead inferred to exchange

138   sugars with the cytoplasm via triose phosphates only (Moog, Nozawa et al. 2020, Liu,

139   Storti et al. 2022) (**Fig. 1A**). The lower half of respiratory glycolysis-gluconeogenesis

140   in diatoms occurs in the mitochondria, as opposed to the cytoplasm (Kroth, Chiovitti

141   et al. 2008, Río Bártulos, Rogers et al. 2018); and a complete plastid lower half

142   glycolysis-gluconeogenesis, including cpEnolase and cpPGAM proteins, has been

143   inferred from sequenced diatom genomes (Kroth, Chiovitti et al. 2008, Smith,

144   Abbriano et al. 2012, Hippmann, Schuback et al. 2022) (**Fig. 1A**). As diatoms are

145   unicellular and colonial species, plastid glycolysis presumably occurs organelles that

146   perform photosynthesis, contrasting with its predominant association with non-

147   photosynthetic tissues in plants (**Fig. 1A**).

148

149   Here, we profile sequence datasets from cultivated and environmental diatoms,

150   perform characterization of *P. tricornutum* CRISPR-CAS9 knockout mutants and

151   measure kinetic activities of expressed enzymes, to infer possible functions of diatom

152   cpEnolase and cpPGAM enzymes. We demonstrate that the genes encoding these

153   enzymes arose from diatom mitochondria-targeted and respiratory isoforms in a

154   common ancestor of all species, contrasting to other algae and plants in which it has

155   a sporadic distribution. We further show that the genes encoding these proteins are

156   most highly expressed at high latitudes in environmental sequence data from *Tara*

157   Oceans, and indeed their expression is induced in *Phaeodactylum* in response to

158   continuous light and low temperature. From *Phaeodactylum* knockout phenotypes,

159   we present evidence that this pathway may have different functions in cells grown

160   under continuous illumination as opposed to light-dark cycling, and at low compared

161   to moderate temperature. We use mutant phenotypes and measured kinetic activities

162   to propose metabolic functions of diatom cpEnolase and cpPGAM under different

163   illumination and temperature regimes. Overall, our data position lower half glycolysis-

164   gluconeogenesis as a modulator of diatom plastid metabolic poise, providing insights

165   into its physiological roles for photosynthetic organisms beyond plants.

166

167   **Results**

168

169 *Distribution and phylogeny of cpEnolase and cpPGAM across photosynthetic*

170 *eukaryotes*

171

172 To evaluate the occurrence of plastid-targeted glycolysis across the algal tree of life,

173 we searched for plastid-targeted homologues of *Phaeodactylum tricornutum* and

174 *Arabidopsis thaliana* enolase and PGAM enzymes in 1,673 plant and algal species,

175 considering genomes from JGI PhycoCosm, and transcriptomes from the MMETSP

176 (Marine Microbial Eukaryotic Transcriptome Sequencing Project) and OneKp (One

177 Thousand Plant Transcriptomes) initiatives (Keeling, Burki et al. 2014, Initiative 2019,

178 Grigoriev, Hayes et al. 2021). Plastid-targeting sequences were inferred using both

179 PFAM domain presence and the combined *in silico* predictions of HECTAR,

180 ASAFind, WolfPSort, TargetP and PredAlgo (Emanuelsson, Brunak et al. 2007,

181 Horton, Park et al. 2007, Gschloessl, Guermeur et al. 2008, Tardif, Atteia et al. 2012)

182 (**Table S1,** sheet 1). Plastid lower glycolysis-gluconeogenesis was frequently inferred

183 in diatoms, with 60/101 (59%) libraries with identified enolase and PGAM sequences

184 possessing plastid-targeted versions of each. A lower occurrence (22/69 libraries,

185 32%) was found amongst close relatives in the stramenopiles (e.g., pelagophytes,

186 dictyochophytes) and other algae with secondary red plastids (cryptomonads,

187 haptophytes; 25/94 libraries, 27%) (**Fig. S1A**). Within primary plastid-harbouring

188 lineages, only angiosperms were inferred to frequently possess plastid-targeted

189 copies of both enzymes (47/537 libraries, 9%). Notably, only 4/127 (3%) occurrences

190 were inferred in primary green algae and none in primary red algae, suggesting that

191 diatom plastid glycolysis does not derive from the secondary red chloroplast ancestor

192 (**Fig. S1A**).

193

194 Considering collection sites, diatom species with either plastid glycolysis enzyme

195 typically derive from higher latitudes (mean absolute latitude 45.6°, standard

196 deviation 13.5°, n = 81) than ones that possess neither (mean absolute latitude

197 38.9°, standard deviation 24.3°, n = 10; one-way ANOVA P = 0.19; **Fig. S1B**). This

198 difference was deemed to be significant for certain diatom groups (e.g., araphid

199 pennate diatoms, **Supplemental Dataset S1**, sheet 1; one-way ANOVA P = 0.012),

200 but was not observed in other algal groups.

201

202   Next, we explored the specific origins of *P. tricornutum* plastid Enolase and PGAM

203   sequences from diatoms by building phylogenies of the closest orthologs obtained

204   from other diatoms, the broader taxonomic group to which they belong, the

205   stramenopiles, and two other algal groups, the cryptomonads and haptophytes.

206   These lineages all possess plastids of secondary red endosymbiotic origin,

207   surrounded by four membranes, which are likely to be closely related to one another

208   (Strassert, Irisarri et al. 2021), but also contain non-photosynthetic members (e.g.,

209   oomycetes in stramenopiles) which only possess respiratory (i.e., mitochondria-

210   targeted) lower half glycolytic enzymes (Río Bártulos, Rogers et al. 2018). Single-

211   gene trees were made for the conserved domains of all organelle-targeted Enolase

212   and PGAM sequences from 289 cryptomonad, haptophyte and stramenopile

213   genomes and transcriptomes, plus all orthologs from 85 further genomes selected

214   from across the tree of life, based on a previously defined pipeline (**Supplemental**

215   **Dataset S1**, sheet 2-9). **Figs. 1B** and **1C** show consensus MrBayes trees realised

216   with GTR, Jones and WAG substitution matrices for species with both identifiable

217   plastid- and mitochondria- targeted orthologs of each protein.

218

219   The obtained topologies revealed multiple evolutionary origins for plastid Enolase

220   and PGAM sequences from mitochondria-targeted (respiratory) enzymes, with

221   diatom plastid isoforms typically having recent and/or diatom-specific evolutionary

222   origins. Diatom cpEnolase sequences resolve in a well-supported clade with plastid-

223   targeted enzymes from bolidophytes, dictyochophytes and pelagophytes, which are

224   sisters to diatoms in the stramenopiles (Río Bártulos, Rogers et al. 2018, Nonoyama,

225   Kazamia et al. 2019), followed by mitochondria-targeted proteins from these groups

226   (MrBayes PP = 1.0 under all studied matrices, **Fig. 1B**), other photosynthetic

227   (chrysophytes) and non-photosynthetic stramenopiles (oomycetes; MrBayes PP = >

228   0.95 under GTR and Jones matrices, **Fig. 1B**). This indicates a duplication and

229   recruitment of the host-derived mitochondria-targeted protein to the plastid within a

230   common ancestor of the diatoms, pelagophytes and dictyochophytes. A broader

231   evaluation of cpEnolase distribution suggests further duplications and plastid

232   retargeting of mitochondria-targeted enolase proteins in both the chrysophytes and

233   cryptomonads (**Fig. S2**).

234

235 The PGAM phylogeny revealed at least two closely-related families of plastid-

236 targeted diatom enzymes, both likely derived from host mitochondrial isoforms. The

237 cpPGAM1A clade (typified by the *P. tricornutum* protein Phatr3_J17086) was closely

238 related to mitochondrial-targeted proteins found across the stramenopiles (MrBayes

239 PP = 1.0 under all studied matrices, **Fig. 1C**), followed by plastid-targeted proteins

240 from chrysophytes and mitochondria-targeted oomycete proteins. Similarly, the

241 cpPGAM1B (Phatr3_J51404) clade included mitochondrial-targeted proteins from

242 pelagophytes and dictyochophytes (MrBayes > = 0.85 under all studied matrices,

243 **Fig. 1C**), and plastid- and mitochondria-targeted enzymes from the chrysophytes

244 (**Fig. S3**). Further duplications and plastid recruitments of mitochondria-targeted

245 PGAM proteins were again visible in the haptophytes and cryptomonads (**Fig. S3**).

246

247 A final plastid-targeted protein annotated as PGAM in the version 3 *P. tricornutum*

248 genome (Rastogi, Maheswari et al. 2018), hereafter termed PGAM2, was identified

249 exclusively in diatoms, pelagophytes, and haptophytes (**Fig. S4**), with limited

250 homology to PGAM1 (BLASTp e-value > 1.0 in pairwise protein-protein searches).

251 Only PGAM1 contain an annotated phospho-glyceromutase active site (IPR005952)

252 per InterProScan, while both PGAM1 and PGAM2 contain the same PFAM (histidine

253 phosphatase, PF03000) per PFAMscan (Jones, Binns et al. 2014, Mistry,

254 Chuguransky et al. 2020). PGAM2 enzymes were predominantly mitochondria-

255 targeted, with plastid- or dual-targeted isoforms amongst diatoms only identified in *P.*

256 *tricornutum* (Phatr3_J37201, and a more divergent copy Phatr3_J47096) and three

257 species in which it is inferred to have evolved independently (**Fig. S4**).

258

259 *Plastidial localisation and expression dynamics of* Phaeodactylum *lower glycolysis*

260 *enzymes*

261

262 To confirm plastid localization of *P. tricornutum* cpEnolase and cpPGAM, eGFP-

263 tagged copies of three proteins (Phatr3_J41515, cpEnolase; Phatr3_J17086,

264 cpPGAM1A; Phatr3_J37201, cpPGAM2) were expressed in *P. tricornutum* Pt1.86

265 cells via biolistic transformation. The observed GFP fluorescence patterns were

266 coincident with chlorophyll autofluorescence, consistent with *in silico* targeting

267 predictions in each case and confirming plastid localization (**Figs. 1D, S5**). We note

268 that both cpEnolase (named per its previous annotation Phatr2_J56418) and

8

269   cpPGAM1B (named Phatr2_J42857) have been independently localised with GFP to

270   the *P. tricornutum* plastid in a separate study (Río Bártulos, Rogers et al. 2018).

271

272   Next, we considered previously published experimental proteomic data of plastid-

273   enriched and *Phaeodactylum* total cellular fractions, following (Huang, Pan et al.

274   2024). Both cpEnolase and cpPGAM1A were detected in multiple plastid-enriched

275   and total cell proteome samples, respectively forming 0.040% and 0.0033% of the

276   mean plastid-enriched total proteome (**Fig. S6A**). These abundances were

277   analogous to the total abundances and plastid enrichment ratios found for other

278   Calvin cycle and plastidial carbon metabolism enzymes, e.g. pyruvate kinase

279   (Phatr3_J22404), ribose-5-phosphate isomerase (Phatr3_J13382), and ribulose-5-

280   phosphate epimerase (Phatr3_J53395). Both mtEnolase (Phatr3_draftJ1572) and

281   mtPGAM (Phatr3_J33839) were also detected in plastid-enriched fractions, which

282   may relate to close associations observed between the *Phaeodactylum* plastid and

283   mitochondria, (Bailleul, Berne et al. 2015, Uwizeye, Decelle et al. 2020). No other

284   organelle-associated enolase or PGAM enzymes were detected, including

285   cpPGAM1B and cpPGAM2, suggesting that they are present at low abundances in

286   the *Phaeodactylum* cell (**Fig. S6A; Supplemental Dataset S2,** sheet 1).

287

288   We further considered the transcriptional dynamics of *Phaeodactylum* lower plastid

289   glycolysis proteins, using a pooled and ranked dataset of normalised microarray and

290   RNAseq data to identify genes that are co-expressed with one another and which

291   may perform linked cellular functions (Ashworth, Turkarslan et al. 2016, Ait-

292   Mohamed, Novák Vanclová et al. 2020, Liu, Storti et al. 2022) (**Fig. S6B**;

293   **Supplemental Dataset S2**, sheet 2-3). From these data, cpEnolase and cpPGAM1A

294   showed strong, positive coregulation to one another (r = 0.868, P < 10^{-05}), with

295   cpPGAM1A the second most strongly coregulated gene to cpEnolase across the

296   entire *Phaeodactylum* genome. Other cpPGAMs showed much weaker coregulation

297   to both cpEnolase and cpPGAM1A, including cpPGAM1B (cpEnolase *r*= 0.432;

298   cPGAM1A *r* = 0.473) and cpPGAM2 (cpEnolase *r*= 0.490; cPGAM1A *r* = 0.478; **Fig.**

299   **S6B**). The coexpression of cpEnolase and cpPGAM1A and accumulation of both

300   encoded proteins in the plastid suggest that they possess linked metabolic functions.

301

9

302   We then explored under what conditions cpEnolase and cpPGAM genes are likely to

303   be highly expressed, considering RNAseq (**Fig. S7A-C**) and microarray (**Fig. S7D**)

304   data (**Supplemental Dataset S2**, sheet 4). These data suggested that nutrient

305   limitation does not directly induce the expression of the chloroplast-targeted

306   glycolysis proteins, with the ratio of expression of genes encoding chloroplast- versus

307   mitochondria-targeted copies of each enzyme either remaining unchanged in

308   published nitrate limitation (nitrate reductase knockout) and iron limitation data (**Fig.**

309   **S7A, B;** one-way ANOVA P < 0.05 (Smith, Gillard et al. 2016, McCarthy, Smith et al.

310   2017)). In an analogous study of phosphate limitation, we even observed a lower

311   ratio of plastid to mitochondrial glycolysis gene expression in phosphate-starved

312   versus -replete and -replenished cell lines (ptEnolase/ mtEnolase ratio one way

313   ANOVA P = 0.009, ptPGAM/ mtPGAM ratio one-way ANOVA P = 0.049 (**Fig. S7C**;

314   (Cruz de Carvalho, Sun et al. 2016)).

315

316   In contrast, we observed clear impacts of light quality and daylength on plastidial

317   glycolysis gene expression. In an RNAseq study of the effects of the Circadian cycle

318   on Fe-limited and -replete *Phaeodactylum* cells (Smith, Gillard et al. 2016), a much

319   higher ratio of plastid to mitochondrial Enolase gene expression was identified in

320   samples harvested twelve hours post-illumination than other time points (**Fig. S7B**;

321   one-way ANOVA P = 4 x 10^{-05}). From a similar meta-analysis of microarray data

322   (Ashworth, Turkarslan et al. 2016), cpEnolase showed greatest relative fold-change

323   in RNA samples (one-way ANOVA P < 10^{-05}) collected between 8 and 16h after the

324   light onset, and were strongly suppressed following 30 minutes of white, red, green

325   and blue light treatment (**Fig. S7D**). cpPGAM showed the same trends albeit with

326   lower expression in normal light 10.5 h after the light induction period than 16h (**Fig.**

327   **S7D; Supplemental Dataset S2,** sheet 4). Both cpEnolase and cPGAM1A showed

328   strong suppression in microarray data obtained following four hours compared to

329   thirty minutes dark incubation (one-way ANOVA, P 0.05); and two days dark

330   incubation compared to two-days high light treatment (one-way ANOVA P < 10^{-05};

331   **Fig. S7D**) suggesting that these effects relate to light perception.

332

333   Finally, we performed quantitative RT-PCR of cpEnolase and cpPGAM1A genes

334   from wild-type *Phaeodactylum* cells under different conditions (**Fig. 2B**). qRT-PCRs

335   were performed on RNA collected from late exponential phase cells at the subjective

336   day mid-points at 19°C and 12 h: 12 h light: dark cycling (19C LD); the same time but

337   for cells grown under 19°C and 24 h continuous light (19C CL); and the same time

338   but for cells grown under 8°C and 24 h continuous light (8C CL), considering *Tara*

339   Oceans sampling data (see below; **Supplemental Dataset S2**, sheet 4). qRT-PCRs

340   were performed using two RT-PCR amplicons for each gene and two normalisation

341   references (RPS, and TBP) previously shown to have invariant expression under

342   Circadian cycles in *Phaeodactylum* (Sachse, Sturm et al. 2013).

343

344   Both cpEnolase and cpPGAM1A showed transcriptional responses to light and

345   temperature, with different responses dependent on normalisation reference. The

346   expression of cpEnolase was inferred to be increased in 19C CL relative to 19C LD

347   when normalised to RPS (fold-change: 2.31, one-way ANOVA P = 0.028) although

348   no difference was measured by normalisation to TBP. In contrast, the expression of

349   cpEnolase was found to be significantly higher under 8C CL than 19C CL conditions

350   considering both RPS (fold-change: 2.74, P = 0.015) and TBP (fold-change: 4.17, P

351   = 0.001; **Fig. 2B**). cPGAM1A expression was inferred to be increased in 19C CL

352   relative to 19C LD conditions normalised to both RPS (fold-change: 6.33, P = 0.003)

353   and TBP (fold-change: 2.50, P = 0.002); but was only inferred to increase in 8C CL

354   relative to 19 CL conditions normalised to TBP (fold-change: 1.96, P = 0.005; **Fig.**

355   **2B**). In total these data suggest additive effects of both continuous light and low

356   temperature on *Phaeodactylum* cpPGAM1A and cpEnolase expression.

357

358   *Environmental roles of diatom cpEnolase and cpPGAM inferred from meta-genomics*

359

360   Next, we considered general patterns of transcriptional co-regulation of diatom

361   cpEnolase and cpPGAM sequences in environmental sequence data from *Tara*

362   Oceans. First, we used a previously benchmarked pipeline, based on combined

363   hmmer, reciprocal BLAST and phylogenetic filtration (Liu, Storti et al. 2022) to identify

364   *Tara* Oceans meta-genes that reconcile exclusively with plastid-targeted proteins

365   from cultured diatom species, to the exclusion of non-diatom and non-plastid

366   homologs (**Fig. S8A**). Amongst the retained meta-genes likely to be N-terminally

367   complete (BLAST homology within the first 40 residues of a *P. tricornutum*

368   sequence), a majority have consensus plastid-targeting sequences (enolase: 38/ 78-

369   49%, PGAM: 58/ 97- 60%). Only a very small number (one enolase, 10 PGAM)

370 possess mitochondrial or endomembrane localizations, suggesting that they

371 principally correspond to plastid-targeted environmental homologs of each protein

372 (**Fig. S8B, Supplemental Dataset S3**, sheet 11).

373

374 Within *Tara* Oceans data, the greatest relative abundances of diatom cpEnolase and

375 cpPGAM1 were observed in meta-transcriptome (metaT) data in stations from both

376 high northern and southern latitudes (**Fig. 3**). We observed these trends concordantly

377 in both surface and deep chlorophyll maximum (DCM) samples from 0.8 - 2000 μm

378 size filtered (**Fig. 3A**); and in individual size fractions (0.8-3/5 μm, 5-20 μm, 20-180

379 μm, 180-2000 μm (**Fig. S9**), suggesting broad reproductibiilty across diatoms

380 independent of cell size and depth. These levels were notably greater than

381 equivalent levels in meta-genome (metaG) data (**Figs. 3B, S9**).

382

383 To confirm that this was due to a greater expression of cpPGAM and cpEnolase

384 genes, as opposed to being purely driven by the greater relative abundance of

385 diatoms in high latitude *Tara* Oceans stations, we performed multiple normalization

386 tests (**Fig. S10**; **Supplemental Dataset S3**, sheet 10). First, metaT abundances

387 calculated for each gene in the 0.8-2000 μm size fraction were divided by the total

388 relative abundance of all diatom metaT sequences, providing the total proportion of

389 each diatom meta-transcriptome occupied by cpEnolase and cpPGAM. These

390 normalisations showed positive correlations to latitude in both surface and DCM

391 depth fractions, with the greatest relative abundances (> 0.1% total diatom mapped

392 transcripts) typically occurring in stations > 60° (**Fig. S10A**). The observed Pearson

393 correlations to latitude were significantly positive (surface cpEnolase R^2 = 0.18, P <

394 10^{-05}, cpPGAM1A R^2 = 0.23, P < 10^{-05}; DCM cpEnolase R^2 = 0.53, P < 10^{-05},

395 cpPGAM1A R^2 = 0.59, P < 10^{-05}) (**Supplemental Dataset S3**, sheet 10). More

396 broadly across, the metaT-normalised relative abundance levels showed clearest

397 positive correlations to daylength and negative correlations to temperature. No other

398 parameters (e.g., nutrient concentrations) showed as clear correlations to chloroplast

399 glycolysis metaT relative abundances (**Supplemental Dataset S3**, sheet 10).

400

401 Alongside this, the metaT abundances obtained for diatom cpEnolase and cpPGAM

402 genes were compared (via log normalisation, to allow the inclusion of zero values) to

403 the relative abundances calculated for the meta-genomic (metaG) sequences of the

12

404   same genes (**Fig. S10B**). This can be taken as an indicative measurement of the

405   relative ratio of transcript versus gene abundances for each meta-gene, i.e. in effect

406   its expression level. These measurements showed a weaker but still significant

407   positive correlation to latitude for cpEnolase surface fractions ($R^2 = 0.10$, one-tailed

408   *F*-test, P < 0.05) and for both genes in DCM fractions (cpEnolase $R^2 = 0.28$, one-

409   tailed *F*-test P < 0.05, cpPGAM1 $R^2 = 0.29$, one-tailed *F*-test P< 0.05 (**Supplemental**

410   **Dataset S3**, sheet 10). For both genes and in both depth fractions, two individual

411   stations within the Arctic (Station 173, 78.93-78.96°N; Station 188, 78.25°-78.36°N)

412   were observed to have extremely high metaT to metaG ratios (($\log_{10}(1+$metaT$)-$

413   $\log_{10}(1+$metaG$)$) > 3-5) that disrupted the linear relationship between normalised

414   metaT and latitude and point to specifically high expression of chloroplast glycolysis

415   genes in polar waters. To correct for the impacts of these stations, ranked

416   (Spearman) correlation values were also calculated for normalised chloroplast

417   glycolysis metaT expression levels. Significant positive correlations with latitude were

418   detected in multiple individual size fractions and depths (0.8-5, 3/5-20, 20-180, 180-

419   2000 µm), including for cpPGAM1 metaT normalised against metaG in surface 3/5-

420   20 (one-tailed *F*-test, P < 10^{-05}), 20-180 (one-tailed *F*-test; P < 10^{-05}) and 180-2000

421   (one-tailed *F*-test, P < 0.05) µm fractions (**Supplemental Dataset S3**, sheet 10).

422

423   The transcriptional preference of diatom cpEnolase and cpPGAM1 for high latitudes

424   contrasted strongly with PGAM2, which showed equivalent relative abundance in

425   stations from the temperate South Pacific and Atlantic as stations from the Arctic and

426   Southern Oceans (**Fig. S11**; **Supplemental Dataset S3**, sheet 10). In certain size

427   fraction and depth combinations (e.g., DCM 0.8-3, and 3/5-20 µm fractions,

428   normalised against metaG abundances; and surface and DCM 180-2000 µm

429   fractions normalised against all diatom metaT abundances) PGAM2 metaT

430   abundances even demonstrated significant negative correlations to latitude

431   (**Supplemental Dataset S3**, sheet 10).

432

433   Finally, we tested whether the occurrence of plastidial lower glycolysis may correlate

434   to algal abundance at high latitudes. For this, we screened single-cell and meta-

435   genome assembled genomes (sMAGs) from *Tara* Oceans for potential plastid-

436   targeted Enolase and PGAM enzymes, using similar reciprocal BLAST best hit,

437   PFAM annotation and *in silico* targeting prediction techniques as previously used for

438   cultured algae (**Fig. S12**; **Supplemental Dataset S**3, sheet 11) (Delmont, Gaia et al.

439   2022). We emphasise these results are preliminary, as many of these genomes are

440   incomplete, and gene non-detection does not formally confirm absence (Delmont,

441   Gaia et al. 2022, Pierella Karlusich, Nef et al. 2023). For each sMAG, we considered

442   presence or absence of possible plastid-targeted Enolase and PGAM sequences;

443   taxonomic assignation of the MAG; and mean mapped vertical coverage of each

444   MAG in each station (i.e., depth and breadth of the coverage of sequences recruited

445   to each genome), as a proxy for abundance, regardless of whether the plastid-

446   targeted glycolysis genes associated with each sMAG were detected (**Fig. S12**).

447

448   Across 291 eukaryotic algal sMAGs, 32 were found to possess both plausible

449   cpEnolase and cpPGAM proteins, and a further 84 could be assigned either one or

450   the other (**Fig. S12**). As expected, diatoms were found to possess plastid-targeted

451   glycolysis much more frequently than other groups, with 17/ 49 of the diatom sMAGs

452   found to possess both chloroplast-targeted Enolase and PGAM enzymes, and a

453   further 20 one of the two only (**Fig. S12**). We also detected probable complete plastid

454   glycolysis pathways in 10 further sMAGs belonging to lineages (pelagophytes,

455   dictyochophytes, haptophytes, chrysophytes, and bolidophytes) previously inferred to

456   possess complete plastid-targeted glycolysis pathways amongst cultured species

457   (**Fig. S2, S3**). Surprisingly, given the relative paucity of this pathway in cultured

458   primary green algae, we finally identified fiuve putative chlorophyte sMAGs with both

459   plausible cpEnolase and cpPGAM1A proteins (**Fig. S12**). All five of these sMAGs

460   (TARA_AON_82_MAG_00297, AOS_82_MAG_00181, ARC_108_MAG_00063,

461   ARC_108_MAG_00100, and PSW_86_MAG_00289) are assigned as novel

462   members of the genus *Micromonas* which is abundant at high latitudes (Lovejoy,

463   Vincent et al. 2007, Worden, Lee et al. 2009, Delmont, Gaia et al. 2022). Of note, no

464   cultured *Micromonas* are inferred to possess this pathway **(Supplemental Dataset**

465   **S1,** sheet 1). We therefore infer, in particular, that the recurrent *Micromonas* sMAG

466   isoform may be a novel plastid glycolysis pathway specific to uncultivated taxa.

467

468   Considering the biogeography of each sMAG, we note that diatoms that possess

469   complete lower half plastidial glycolysis pathways shows positive correlations

470   between mean mapped vertical coverage and absolute station latitude, albeit only in

471   DCM fractions (**Fig. S12A**; r= 0.517, P< 0.001, while positive correlations to lartitude

14

472 were observed for diatom sMAGs possessing one of cpEnolase or cpPGAM only

473 at both depths (**Fig. S12A**; surface r= 0.313, two-tailed t-test P= 0.003, DCM r= 0.614,

474 P< 0.001). This trend was not however observed for diatom sMAGs lacking plastid-

475 targeted copies of both proteins, which showed non-significant and even weakly

476 negative correlations to absolute latitude (**Fig. S12A**; surface r= -0.069, DCM r=

477 0.192, P> 0.1). No clear association between plastidial lower half glycolysis and

478 occupancy at high latitudes was observed for other algal groups, with the exception

479 of chlorophytes, in which the presence of both cpEnolase and cpPGAM1A showed a

480 strong association with abundance in high (and particularly) Arctic latitude stations

481 (surface r = 0.508, P< 0.001; DCM r = 0.386, P = 0.017; **Fig. S12B, S12C**).

482

483 *Growth and photo-physiology of* Phaeodactylum *cpEnolase and cpPGAM1A*

484 *knockouts across light and temperature conditions*

485

486 We generated homozygous CRISPR knockout lines for both cpEnolase and

487 cpPGAM1A in the model diatom *P. tricornutum*. cpPGAM1A was selected over other

488 PGAM (cpPGAM1B, cpPGAM2) isoforms because of its transcriptional co-regulation

489 to cpEnolase and occurrence in measurable quantities in plastid proteome data (**Fig.**

490 **S6**; **Supplemental Dataset S2**) and latitudinal expression correlation in *Tara* Oceans

491 (**Figs. 3, S11**).

492

493 Multiple CRISPR knockout lines were generated from two regions with unique

494 sequences in the *P. tricornutum* genome for each gene (cpEnolase CRISPR region 1

495 n= 4, CRISPR region 2 n= 3; cpPGAM1A CRISPR region 1 n= 2, CRISPR region 2

496 n= 3) (**Fig. S13A**). Each CRISPR line was verified by sequencing to be homozygous

497 and to contain a frame-shift mutation sufficient to impede translation of the encoded

498 protein (**Fig. S13A**). Commercial antibodies against enolase and PGAM were found

499 not to specifically label cpEnolase and cpPGAM1A in Western Blots, and so we

500 inferred protein relative expression level by qRT-PCR using recognised *P.*

501 *tricornutum* housekeeping genes as above (Sachse, Sturm et al. 2013, Zhang,

502 Sampathkumar et al. 2020). The measured knockout mRNA abundance in each line

503 was significantly lower (1.8-39 %) than that identified in empty vector control mRNA

504 (n = 4, one-way ANOVA, P < 0.05) 19C LD conditions, **Fig. S13B**). This is consistent

505 with effective knockdown of mutated genes e.g., via non-sense mediated decay

506 (Chang, Imam et al. 2007).

507

508 Next, we performed growth curves of cpEnolase and cpPGAM1A knockout lines

509 compared to empty vector controls (**Fig. 4**; **Supplemental Dataset S4**, sheets 3-6).

510 We chose to target changes in light and temperature, given that both show clear

511 associations observed with cpPGAM1A and cpEnolase in *Phaeodactylum* gene

512 expression and *Tara* Oceans data (**Fig. 2, 3**), using the three conditions (19C CL,

513 19C LD, and 8C CL) previously tested for qRT-PCR. We note that these conditions

514 are relevant to the environmental conditions in which the type culture of

515 Phaeodactylum (strain CCAP 1055/1) was collected (Irish Sea, 53.5°N) with

516 measured sea temperatures (1960-1999) between 3°C and 17°C ; and day lengths

517 between 7 and 17 hours (Young and Holt 2007, Gachon, Heesch et al. 2013).

518

519 Under 19C LD conditions, plastid glycolysis-gluconeogenesis knockout lines showed

520 an approximately 10-15% reduction in relative growth rate compared to empty vector

521 controls (cpEnolase growth rate 0.83± 0.06 cells day$^{-1;}$ cpPGAM1A growth rate 0.85±

522 0.07 cells day$^{-1;}$ empty vector growth rate 0.94 ± 0.05 cells day^{-1}; **Fig. 4, S14;**

523 **Supplemental Dataset S4**, sheet 3; cpEnolase growth rate 87.7% control and

524 cpPGAM1A growth rate 90.1% control, one-way ANOVA, two-tailed P < 0.05).

525 Under 19C CL, knockout lines showed a 25-30% reduction in relative growth rate

526 compared to controls (cpEnolase growth rate 0.99± 0.16 cells day^{-1}; cpPGAM1A

527 growth rate 1.08± 0.04 cells day^{-1}; empty vector growth rate 1.39 ± 0.09 cells day^{-1};

528 **Fig. 4, S14**; **Supplemental Dataset S4**, sheet 4; cpEnolase growth rate 70.7%

529 control and cpPGAM1A growth rate 77.5% control, one-way ANOVA, two-tailed P <

530 0.01). Under 8C C, overlapping growth rates were observed for knockout and control

531 lines, albeit with a possible reduction in cpEnolase knockout growth rate (cpEnolase

532 relative growth rate 0.49± 0.10 cells day^{-1}, cpPGAM1A growth rate 0.64± 0.02 cells

533 day^{-1}, empty vector growth rate 0.62± 0.07 cells day^{-1}; **Fig. 4, S14; Supplemental**

534 **Dataset S4**, sheet 5; cpEnolase growth rate 78.1% control and cpPGAM1A growth

535 rate 102.9% control; one-way ANOVA, two-tailed P non-significant).

536

537 To test the possibility of off-target effects of the CRISPR constructs, we

538 complemented mutant lines with blasticidin resistance genes linked to either

16

539   cpEnolase-GFP or cpPGAM1A-GFP modified to remove all CRISPR target

540   sequences (**Supplemental Dataset S4**, sheet 2) (McCarthy, Smith et al. 2017, Buck,

541   Río Bártulos et al. 2018). Despite an overall lower growth rate in all blasticidin-

542   resistant lines compared to primary transformants, and within-line variation,

543   comparative growth curves of 47 complemented versus placebo transformed mutant

544   lines revealed increased growth rates in complemented cpEnolase and cpPGAM1A

545   versus blank transformed knockout lines under 19C CL and 19C LD (**Supplemental**

546   **Dataset S4**, sheet 7; one-way one-way ANOVA, two-tailed P, < 0.05). By contrast,

547   complemented knockout line growth rates overlapped with empty vector controls

548   either transformed with cpEnolase or blank complementing vectors, indicating

549   effective recovery of mutant phenotypes (**Supplemental Dataset S4**, sheet 7).

550

551   Finally, we performed comparative photophysiological measurements of knockout

552   lines in the two conditions (19C LD and 19C CL) where they presented a growth

553   phenotype (see Methods). Our data indicate that the presence/ absence of these

554   enzymes does not significantly impact photosynthetic performance. The light

555   dependencies of either electron transfer rate through photosystem II (PSII) (rETR(II))

556   or photoprotection (non-photochemical quenching, NPQ) were very similar between

557   control and knock-out lines (**Fig. S15A**; **Supplemental Dataset S4**, sheets 8-11). A

558   slight but significant increase in the functional absorption cross-section of

559   photosystem II (σPSII) was found under 19C CL in both cpEnolase (319.3± 22.5) and

560   cpPGAM1A knockouts (306.6± 11.6) compared to controls (292.3± 8.2; one-way

561   ANOVA, P < 0.05) (Gorbunov, Shirsin et al. 2020). This elevation was suppressed in

562   both complemented lines (**Fig. S15B**; **Supplemental Dataset S4**, sheet 11).

563

564   *Gene expression profiling of* Phaeodactylum *cpEnolase and cpPGAM1A knockouts*

565

566   Next, we investigated the impacts of disruption of plastid glycolysis on diatom

567   metabolism beyond photosynthesis. First, we performed quantitative RNA-seq

568   analysis using 63 RNA samples drawn from multiple knockout and empty vector lines

569   under all three physiological conditions (19C LD, 19C CL, and 8C CL; **Supplemental**

570   **Dataset S5**, sheet 1; Materials and Methods). 8C CL was targeted despite the

571   absence of a growth phenotype associated with this line due to the high levels of

572   cpEnolase and cpPGAM1A gene expression inferred from qRT-PCR data (**Fig. 2B;**

17

573   **Fig. 4**) Complete results are provided in **Supplemental Dataset S5**, sheets 5-11.

574   Both cpEnolase and cpPGAM1A mRNA were found to significantly under-accumulate

575   in the corresponding knockout lines, consistent with qRT-PCR analysis (**Fig. S13B**)

576   and suggesting maintenance of the mutant genotypes throughout RNA sequencing;

577   while cpPGAM1B (Phatr3_J51404) but not cpPGAM2 (Phatr3_J37201) was

578   upregulated in cpPGAM1A knockouts but not cpEnolase knockouts under 19C CL

579   conditions, which may suggest compensatory functions between cpPGAM1A and

580   cpPGAM1B (**Supplemental Dataset S5**, sheet 12**).**

581

582   Genome-scale enrichment analyses of the *in silico* localizations of proteins encoded

583   by differentially expressed genes revealed distinctive changes in glycolysis knockout

584   organelle metabolism. These effects were most evident in 19C CL, in which 90/239

585   (38%) of the genes differentially upregulated (mean fold-change >2, P-value < 0.05)

586   in both cpEnolase and cpPGAM1A knockout lines compared to controls were

587   predicted to possess chloroplast targeting sequences based on ASAFind (Gruber,

588   Rocap et al. 2015) or HECTAR (Gschloessl, Guermeur et al. 2008). This was

589   significantly greater than the proportion of genes (1,585/11,514, 14%) across the

590   entire genome predicted to encoding chloroplast-targeted proteins that were detected

591   in RNAseq data (one-tailed chi-squared P < 10^{-05}; **Fig. 5A; Supplemental Dataset**

592   **S5**, sheet 10). These results were supported by domain enrichment analyses,

593   indicating significant (one-tailed chi-squared P < 0.05) enrichments in light-harvesting

594   complex (GO:0030076), photosynthesis (GO:0009765) and protein-chromophore

595   linkage (GO:0018298) GO terms. A more detailed resolution of gene expression

596   patterns underpinning core organelle metabolism pathways (Ait-Mohamed, Novák

597   Vanclová et al. 2020) suggested concerted upregulation of genes encoding light-

598   harvesting complexes and photosynthesis machinery and plastid fatty acid synthesis

599   machinery, alongside a probable upregulation of mitochondrial respiratory complex I

600   and ATP synthase (**Supplemental Dataset S5**, sheets 10-11). Less dramatic

601   changes were evident in 19C LD and 8C CL, although 13 of the 51 genes (25%)

602   inferred to be downregulated in both cpEnolase and cpPGAM1A knockout lines

603   under 8C CL were inferred to encode chloroplast-targeted proteins by either ASAFind

604   or HECTAR, representing likewise an enrichment compared to all genes identified

605   within the RNAseq data (one-tailed chi-squared P < 0.05; **Fig. 5A**).

606

607   To gain a more precise insight into the effects of plastid glycolysis-gluconeogenesis

608   on *P. tricornutum* metabolism, we additionally validated the differential expression of

609   eleven exemplar genes encoding chloroplast- and mitochondria-targeted proteins by

610   qPCR in knockout and empty vector control lines across all three conditions (**Fig. 5B**;

611   **Supplemental Dataset S5**, sheet 12). These genes showed relatively limited

612   differences under 19C LD, limited to a slight depression in the accumulation of *Lhcf1*

613   (Phatr3_J18049) and chorismate mutase (Phatr3_J43277) mRNA in both cpEnolase

614   and cpPGAM1A knockouts compared to control lines (~50% downregulation, two-

615   tailed *t*-test P < 0.05; **Fig. 5B**). Both knockout lines over-accumulated (>600%; two-

616   tailed *t*-test P < 10^{-05}) mRNAs encoding mitochondrial phospho-glycerate mutase

617   (Phatr3_J33839) under 19C LD compared to control lines (**Fig. 5B**).

618

619   Under 19C CL, we observed more substantial changes in plastid metabolism,

620   including the significant (two-tailed *t*-test P < 0.05) over-accumulation of mRNAs

621   encoding Lhcf1 (~150%), a plastid-targeted petB-type protein presumably involved in

622   cytochrome b_6f metabolism (Phatr3_J13558, ~90%), and a particularly strong over-

623   accumulation of plastid lysophosphatidyl acyltransferase (LPAT), involved in plastid

624   lipid synthesis (Phatr3_J20640, ~100%, two-tailed *t*-test P < 10^{-05}) in both knockout

625   lines (**Fig. 5B**). Significant over-accumulations were also observed of mRNAs

626   encoding plastid signal processing peptidase (Phatr3_J10319, 60-120%), alanine

627   transaminase (Phatr3_J34010) and coporphyrinogen oxygenase (Phatr3_J12186), in

628   either cpEnolase or cpPGAM1A knockout lines (**Fig. 5B**). Concerning mitochondrial

629   metabolism, a strong increase (>250%, two-tailed *t*-test P < 10^{-05}) was observed in

630   mRNA for NDH dehydrogenase subunit 1 (Phatr3_J43944), involved in oxidative

631   phosphorylation, but a corresponding decrease (>40%, two-tailed *t*-test P < 10^{-05}) in

632   mRNA for citrate synthase within the TCA cycle (Phatr3_J30145).

633

634   Finally, under 8C CL, contrasting and complementary changes were observed: up-

635   regulation (>60%; two-tailed *t*-test P < 10^{-05}) of genes encoding both the plastid

636   signal processing peptidase and petB-related protein, and mitochondrial PGAM and

637   citrate synthases in both knockout lines compared to controls (**Fig. 5B**). Both

638   knockout lines were found to under-accumulate *Lhcf1* mRNA (>90%; two-tailed *t*-test

639   P < 10^{-05}), while *Lhcx4* (Phatr3_J38720), encoding a dark-expressed gene of

640   unknown direct function but homologous to the Lhcx1 protein implicated in

19

641   photoprotection (Buck, Sherman et al. 2019), was found to substantially over-

642   accumulate in both cpEnolase and cpPGAM1A knockout lines (**Fig. 5B**).

643

644   *Metabolite profiling of* Phaeodactylum *cpEnolase and cpPGAM1A knockouts*

645

646   Next, we considered the compound effects of cpEnolase and cpPGAM1A knockout

647   on global metabolite accumulation under each environmental condition via GC-MS

648   profiling of 32 sugars and amino acids (**Fig. 6; Fig. S16**), across 139 samples drawn

649   from multiple knockout and control lines under 19C LD, 19C CL and 8C CL. These

650   samples were obtained from cell pellets collected from mid-exponential phase

651   cultures, and thus correspond to the long-term impacts on metabolite accumulation in

652   actively growing plastid glycolysis knockout lines. Complete outputs are tabulated in

653   **Supplemental Dataset S6**, sheets 1-2.

654

655   We were unable to directly measure the accumulation of any of the products or

656   substrates of either cpPGAM1A or cpEnolase (3-phosphoglycerate, 2-

657   phosphoglycerate, PEP), although we detected significantly diminished (one-way

658   ANOVA two-tailed P-value < 10^{-05}) pyruvate accumulation, as a metabolite

659   synthesised from PEP (by pyruvate kinase), in cpPGAM1A knockouts under all three

660   conditions, and in cpEnolase knockouts under 8C CL (**Fig. 6, S16**). We similarly

661   could not directly measure the accumulate of glyceraldehyde-3-phosphate (the

662   substrate for PGAM), but could detect an overaccumulation of glycerol-3-phosphate

663   (synthesised from glyceraldehyde-3-phosphate by glycerol-3-phosphate

664   dehydrogenase) in cpEnolase knockout lines under all three conditions (**Fig. 6**).

665

666   In all three conditions, significant reductions (one-way ANOVA two-tailed P-value <

667   0.01 in both cpEnolase and cpPGAM1A knockout lines) were observed in

668   cytoplasmic sugars and sugar derivatives (glucose, sucrose, histidine, *myo*-inositol)

669   in cpEnolase and cpPGAM1A knockouts compared to control lines (**Fig. 6**).

670   cpEnolase and cpPGAM1A knockout lines further under-accumulated citric acid in all

671   three conditions, and malic acid in 8C CL (**Fig. 6**). A probable over-accumulation of

672   phosphoric acid was observed in all knockout lines except cpPGAM1A under 19C CL

673   (**Fig. 6; S17**). Significant (one-way ANOVA two-tailed P-value < 10^{-05}) over-

674   accumulations were identified for valine in cpEnolase and cpPGAM1A knockouts

20

675   under 19C CL and 8C CL; for methionine and ornithine in 19C CL only; and an

676   under-accumulation for arginine under 19C CL only (**Fig. 6**).

677

678   Finally, specific differences were observed in the metabolite accumulation patterns

679   observed in cpEnolase and cpPGAM1A knockout lines (**Fig. 6; S16**). These include a

680   significant (one-way ANOVA two-tailed P-value $< 10^{-05}$) over-accumulation of three

681   amino acids (aspartate, leucine and phenylalanine) and one sugar phosphate

682   (glycerol-3-phosphate) specifically in cpEnolase knockout lines under all three

683   conditions, and in serine under 19C CL and 8C CL only. These differences contrast

684   to cpPGAM1A knockouts in which no significant changes were observed.

685   Surprisingly glycerol-3-phosphate and serine were found to significantly under-

686   accumulate under all three conditions in cpPGAM1A knockouts compared to controls

687   **(Fig. 6**; **S16**).

688

689   *Lipid profiling of* Phaeodactylum *cpEnolase and cpPGAM1A knockouts*

690

691   Next, we performed GC-MS (55 samples) and LC-MS (49 samples) of lipid profiles in

692   multiple knockout and control lines under 19C LD, 19C CL and 8C CL. Outputs are

693   tabulated in **Supplemental Dataset S6**, sheets 1, 3-5. While the GC-MS data project

694   significant (one-way ANOVA two-tailed P-value < 0.05) impacts of growth condition

695   on fatty acid profiles (e.g., a decrease of C20:5 side chain lipids balanced by an

696   increase of C16:1 side chain lipids in 19C CL, and an over-accumulation of C16:3

697   side chain lipids under 19C LD, and of C18:0 side chain lipids under 8C CL), no

698   substantial differences were observed between cpEnolase, cpPGAM1A and control

699   lines under any conditions studied (**Supplemental Dataset S6,** sheet 3).

700

701   In contrast to the relatively limited effects on total fatty acid profiles, LC-MS analyses

702   of lipid class distributions revealed substantial changes in lipid class distribution in

703   plastid glycolysis-gluconeogenesis knockout lines (**Fig. 7**; **Supplemental Dataset**

704   **S6,** sheet 4). Even accounting for within-line variation, both cpEnolase and

705   cpPGAM1A knockouts were found to significantly under-accumulate triacylglycerols

706   (TAG) (cpEnolase 3.98 ± 1.94%, cpPGAM1A 3.60 ± 1.72%, control 12.18 ± 7.26%;

707   one-way ANOVA, two-tailed P separation of means between knockout and control

708   lines < 0.05) and over-accumulate monogalactosyldiacylglycerols (MGDG; cpEnolase

709   63.83 ± 4.33%, cpPGAM1A 60.89 ± 5.64%, control 49.68 ± 8.88%; one-way ANOVA,

710   two-tailed P< 0.05) under 19C LD (**Fig. 7A**). Further significant (P < 0.05) under-

711   accumulations were detected in knockout lines for diacylglycerols (DAG) and

712   sulfoquinovosyl-diacylcerols (SQDG) under 19C LD. Similar tradeoffs were observed

713   under 19C CL, albeit with an over-accumulation, rather than under-accumulation of

714   DAG, and an additional under-accumulation of digalactosyldiacylglycerols (DGDG),

715   in glycolysis knockouts compared to control lines (**Fig; 6B**).

716

717   Detailed analyses of the individual fatty-acid side-chains associated with different

718   lipid classes in glycolysis knockout lines under 19C indicated increased relative

719   contributions of C16:1 fatty acids to plastid membrane lipid *sn*-1 positions

720   (**Supplemental Dataset S6,** sheet 5). These included conserved (P < 0.01) over-

721   accumulations of DGDG-16-1_16-2 under 19C LD (**Fig. S18**); and SQDG 16-1_16-0,

722   MGDG-16-1_16-2, MGDG-16-1_16-3 and DGDG-16-1_16-1, in both cpEnolase and

723   cpPGAM1A knockout lines under 19C CL (**Fig. S19**). A significant over-accumulation

724   of 16-1_16-1 side chains and under-accumulation 20-5_18-4 was also observed for

725   diacylglyceryl hydroxymethyltrimethyl-*β*-alanine (DGTA), a betaine lipid known to act

726   as a platform for the biosynthesis of 20:5 fatty acids, in both cpEnolase and

727   cpPGAM1A knockout lines under 19C LD (**Fig. S18**) (Dolch and Maréchal 2015,

728   Popko, Herrfurth et al. 2016).

729

730   Under 8C CL, quite different trends were observed in fatty acid accumulation in

731   cpEnolase knockouts compared to cpPGAM1A knockouts and controls. These

732   correlated principally with an over-accumulation of TAG (cpEnolase 20.88 ± 12.21%,

733   cpPGAM1A 9.62 ± 6.31%, control 8.15 ± 3.95%; one-way ANOVA, two-tailed P <

734   0.05) in lieu of MGDG (cpEnolase 34.20 ± 6.74%, cpPGAM1A 42.94 ± 6.01%, control

735   46.61.3 ± 6.25%; one-way ANOVA, two-tailed P < 0.5; **Fig. 7A**). An over-

736   accumulation of SQDG was observed in both cpEnolase and cpPGAM1A knockouts

737   compared to controls, albeit with greater severity in cpEnolase knockouts (**Fig. 7B**).

738   Considering side-chain distributions of individual lipid classes, a significant (one-way

739   ANOVA two-tailed P-value < 0.01) over-accumulation of short-chain (C14:0, C16:1)

740   and *sn*-1 and *sn-2* fatty acids was observed in cpEnolase knockouts (**Fig. S20A**). A

741   probable exchange of very long-chain *sn*-2 fatty acids in SQDG pools was further

742   observed in cpEnolase knockouts, with significant (one-way ANOVA two-tailed P-

22

743 value < 0.01) increases in SQDG 14-0_16-0 and SQDG-14_0-16-1 in lieu of SQDG-

744 16-2_24-0 in cpEnolase knockouts compared to cpPGAM1A and control lines (**Fig.**

745 **S20B**; **Supplemental Dataset S6**, sheet 5).

746

747 *Reaction kinetics of expressed copies of* Phaeodactylum *cpEnolase and cpPGAM1A*

748

749 Finally, we assessed the kinetics of cpPGAM and cpEnolase in both glycolytic and

750 gluconeogenic directions. Previous studies (e.g., in animal renal and liver tissue)

751 project reversible reaction kinetics for both enolase and PGAM enzymes. The

752 reaction rates of enolase and PGAM show limited difference in glycolytic versus

753 gluconeogenic directions *in vivo*, with measured enolase rates in rat kidney tissue

754 equivalent to approximately 14,000 µmol g dry weight^{-1} hr^{-1} in the glycolytic direction,

755 and 20,000 µmol g dry weight^{-1} hr^{-1} in the gluconeogenic direction (KREBS 1963,

756 Scrutton and Utter 1968, Reinoso, Telfer et al. 1997). Equally, purified enolase and

757 PGAM typically show greater affinity for 3-PGA than PEP, with a 5-8 fold difference in

758 Km measured in mammalian, yeast and *Trypanosoma brucei* enzymes (Rider and

759 Taylor, 1974; Hannaert et al., 2003).

760

761 Using a previously defined assay (Sutherland, Posternak et al. 1949, Zhang,

762 Sampathkumar et al. 2020) with modified versions of each protein (codon-optimised,

763 and lacking signal peptides) expressed in *E. coli,* alongside measured NADH

764 consumption coupled to either lactate dehydrogenase (glycolysis) or glyceraldehyde-

765 3-phosphate dehydrogenase (**Fig. S20**). Both enzymes were inferred to possess

766 reversible reaction kinetics, metabolizing NADH when supplied both with 3-PGA (in

767 the glycolytic direction) and PEP (in the gluconeogenic direction; **Fig. 8, Fig. S20**).

768 The measured reaction rates were effectively reversible, albeit marginally greater in

769 the glycolytic than gluconeogenic direction (e.g., 2.47 ± 0.43 versus 1.97 ± 0.29 nMol

770 NADH consumption per gram free weight purified enzyme per minute when supplied

771 with12 mM 3PGA or 12 mM PEP; **Fig. 8**).

772

773 **Discussion**

774

775 We characterise a lower glycolytic-gluconeogenic pathway associated with diatom

776 plastids, relating specifically to two plastid-targeted proteins, cpEnolase and

777   cpPGAM1A, and focusing on the model species *P. tricornutum*. Our data position

778   plastid glycolysis-gluconeogenesis as arising in a recent ancestor of diatoms and

779   their closest relatives (e.g., pelagophytes, dictyochophytes) (Nonoyama, Kazamia et

780   al. 2019). The presence of plastid glycolysis in haptophytes may be as a result of

781   endosymbiotic transfers into this group from a pelagophyte/ dictyochophyte-related

782   alga, as suggested in previous studies (Dorrell, Gile et al. 2017, Jiang, Cao et al.

783   2023). We further show that plastidial lower glycolysis-gluconeogenesis has a limited

784   distribution across the algal tree of life, with no examples in primary red and few in

785   primary green algae (**Fig. S1, S12**). It is possible that the occurrence of organelle-

786   targeted isoforms of these enzymes is underestimated, e.g., due to lower sensitivity

787   of diatom and plant-trained targeting predictors on other algal groups (Fuss,

788   Liegmann et al. 2013, Gruber, Rocap et al. 2015). We propose that diatom plastid

789   glycolysis most likely originated through the duplication and retargeting of

790   mitochondrial respiratory enzymes (**Fig. 1**).

791

792   Using meta-genomic data from *Tara* Oceans we demonstrate that diatom plastid

793   glycolysis is likely highly expressed at high latitudes (**Figs. 3, S8-S11**), which are

794   subject to extreme photoperiods and low temperature. These data are further

795   supported by collection sites of cultured species, with no occurrences of cultured

796   diatoms lacking plastid-targeted PGAM enzymes beyond 50°N (**Fig. S1B**), and

797   evidence from meta-genome assembled genomes, in which diatoms that possess

798   apparent plastid-targeted Enolase and PGAM enzymes show an associative

799   preference for high latitudes, while those that lack them do not (**Fig. S12**). These

800   enrichments appear to be largely specific to diatoms, with polar circle haptophytes,

801   cryptomonads and other ochrophytes lacking apparent plastidial glycolysis found

802   further than 60°N and 70°S, considering both cultured species and MAG data,

803   although with a potential parallel recruitment of plastidial glycolysis to isolates of the

804   prasinophyte genus *Micromonas* abundant in high latitude *Tara* stations (Lovejoy,

805   Vincent et al. 2007). We thus tentatively propose that lower half plastid glycolysis

806   correlates to diatom occurrence in high latitude *Tara* Oceans stations, with diatoms

807   that lack identifiable copies of these proteins absent from these stations, and other

808   algal groups (except potentially chlorophytes) showing no preference for plastidial

809   glycolysis at high latitudes.

810

811   We are hesitant to state that plastid glycolysis is an adaptive feature of diatoms

812   towards high latitudes, given it apparently originated in a common ancestor of

813   diatoms and several other algal groups (i.e., pelagophytes, and dictyochophytes),

814   and is retained in species such as *Phaeodactylum* which is typically associated with

815   intermediate latitudes (Rastogi, Vieira et al. 2020). cpEnolase and cpPGAM cannot

816   therefore have been viewed to have been gained in specific diatom species in

817   response to environmental selection. An open question, particularly given the largely

818   latitude-insensitive distributions to diatom MAGs lacking plastid glycolysis, remains to

819   what extent diatoms that have secondarily lost their plastid glycolytic pathway are

820   abundant in nature (**Fig. S12**). Ultimately, the physiological functions of diatom

821   plastid glycolysis will be best identified through competition assays e.g. between

822   diatom species with different plastid carbon metabolism arrangements, or between

823   *Phaeodactylum* knockout and empty vector control lines under each condition

824   (Siegel, Baker et al. 2020).

825

826   Nonetheless, from our analysis of published *Phaeodactylum* transcriptome data and

827   qRT-PCRs, we note that both cpEnolase and cpPGAM1A genes are transcriptionally

828   induced in response to both long day conditions and low temperatures (**Fig. 2B, S7**).

829   These biases are particularly interesting given the growth analysis of *P. tricornutum*

830   knockout lines. In particular, we observe more intense growth defects in

831   *Phaeodactylum* lines under continuous illumination than in light: dark cycles (**Figs. 4,**

832   **S9**), which alongside gene expression data suggests increased importance of plastid

833   glycolysis in diatoms subject to long days. In contrast, under low temperatures no

834   difference was observed in the growth rate of glycolysis knockouts showed to control

835   lines (**Fig. 4**). We note that the relative expression of cpEnolase and cpPGAM1A are

836   even greater at 8C than 19C under continuous light conditions, and it is possible that

837   flux occurs through plastid glycolysis at low temperature despite the absence of a

838   clear growth phenotype in knockout versus control lines. We thus tentatively propose

839   that lower glycolysis-gluconeogenesis may have multiple functions in the diatom

840   plastid, with different functions dependent on both light and temperature conditions.

841

842   Considering the observed phenotypes of knockout and control lines (**Figs. 4-7; S14-**

843   **S19**) and the reversible kinetics of expressed enzymes, we suggest potential

844   functions contributed by the lower half of plastid glycolysis-gluconeogenesis in

845 diatoms under 19C LD, 19C CL and 8C CL conditions (**Fig. 8)**. Overall, our

846 suggested roles for cpEnolase and cpPGAM1A are predominantly in favour of

847 metabolic flux in the glycolytic direction, reflecting the underaccumulation of pyruvate

848 in cpPGAM1A knockouts, and overaccumulation of 3-phospho-glycerate in

849 cpEnolase knockouts (**Fig. 6**). We also present this hypothesis based on the innate

850 metabolic activity of the Calvin cycle, which is likely to yield a high relative

851 abundance of triose phosphate in the plastid under illuminated and photosynthetically

852 active conditions; although we note that studied diatom triose phosphate transporters

853 show higher transport affinity for PEP than DHAP, which may facilitate substrate

854 supply for gluconeogenic activity (Moog, Nozawa et al. 2020) (**Fig. 8**). These results

855 are nonetheless inferential based on the long-term accumulation patterns of stable

856 metabolites and the expression of implicated metabolic genes. Whilst these would be

857 more effectively validated via direct flux measurements, e.g., comparative ^{13}C-

858 glycerol or -glucose labelling of glycolysis knockout and control lines (Zheng, Quinn

859 et al. 2013, Huang, Liu et al. 2015), this was beyond the scope of the current study.

860

861 Under 19C LD, we observe limited gene expression changes in cpPGAM1A and

862 cpEnolase knockout lines, except (as inferred from qPCR) a downregulation in

863 plastid chorismate mutase, which forms part of the plastid shikimate pathway, that

864 typically consumes PEP (Bromke 2013) and may form a primary acceptor of

865 glycolytic products (**Fig. 5B**). One of the products of chorismate mutase activity,

866 phenylalanine, does seem to overaccumulate in metabolite pools of cpEnolase

867 mutants only under these conditions, pointing to potentially more complex fluxes

868 (discussed below). We also note an upregulation of mitochondrial PGAM in both lines

869 (**Fig. 5B**), which might relate to a greater level of mitochondrial glycolysis, e.g. of

870 exported plastid glyceraldehyde-3-phosphate in the knockout lines. Strikingly, both

871 mutant lines underaccumulate TCA cycle intermediates (citric acid in both lines, and

872 fumaric and malic acid in cpPGAM1A only) which may suggest less retention of

873 metabolised sugar in the mitochondrion. Finally, both mutants also underaccumulate

874 sugars typically synthesised in the cytosol (sucrose, myo-inositol) which we interpret

875 to imply less excess fixed carbon in the knockout compared to control lines (**Fig. 6**).

876 Overall these data seem to point to less efficient carbon usage, and an overall

877 redirection of plastidial triose phosphate from plastid or cytoplasmic anabolic

878 reactions to mitochondrial catabolism in knockout lines.

879

880   We also note some evidence for lipid remodelling in glycolysis mutant lines. These

881   include a relative over-accumulation of galactolipids in lieu of TAGs, and short-chain

882   fatty acids in lieu of longer equivalents (**Figs. 7, S18**). Previous studies have noted

883   the importance of lipid metabolism in diatom stress responses (Zulu, Zienkiewicz et

884   al. 2018), and that most or all diatom lipid synthesis occurs directly in the plastid

885   (Huang, Pan et al. 2024). Many of the metabolic reactions required for lipid synthesis,

886   including acyl-coA synthesis from pyruvate (Maréchal and Lupette 2020), glycerol-3-

887   phosphate from glyceraldehyde-3-phosphate (Kroth, Chiovitti et al. 2008), and

888   glucosyl-1-phosphate from cytoplasmic glucosyl-1-phosphate (Zhu, Shi et al. 2016),

889   are likely to be Impacted by plastid carbon metabolism. Specifically, an

890   underaccumulation of TAGs and fatty acids in lieu of galactolipids would also suggest

891   a lower ratio of pyruvate (for acyl-coA synthesis) to glyceraldehyde-3-phosphate (for

892   galactosyl-phosphate synthesis) in glycolysis knockout lines (Demé, Cataye et al.

893   2014), similarly to the underaccumulation of pyruvate observed in our metabolomic

894   data (**Fig. 6**). We infer that these changes are probably driven by substrate limitation,

895   as we observe no changes in the transcription of genes involved in fatty acid

896   synthesis in glycolysis knockout lines; nor do we increased expression of cpEnolase

897   or cpPGAM1A in cellular conditions (N and P limitation) known to induce diatom lipid

898   accumulation (**Fig. 5B**; **Fig. S7**) (Abida, Dolch et al. 2015)

899

900   Under 19C CL, we observed much more dramatic remodelling of cellular transcription

901   in knockout lines compared to controls (**Fig. 5A**). These are notably concordant with

902   greater expression of cpEnolase and cpPGAM1A in wild-type cells (**Fig. 2B**), and an

903   enhanced growth defect in knockout lines, together suggesting greater potential flux

904   through this pathway than under 19C LD (**Fig. 4B**). The transcriptional changes

905   include greater overall photosynthesis gene expression, e.g., *Lhcf1* (**Fig. 5B**), which

906   was corroborated in photo-physiological analyses by larger PSII antenna size, i.e., a

907   larger functional cross-section (σPSII) (**Fig. S15**). It should be noted that the increase

908   in PSII antenna size does not necessarily change the quantum yield of individual PSII

909   reaction centres, and therefore the increased σPSII is independent of the Fv/ Fm

910   measured, which remains equivalent between knockout and control lines (**Fig. S15**).

911   We did not observe consistent differences in the expression of nitrogen or

912   phosphorus stress metabolism, or in the expression of the *P. tricornutum* biophysical

913 carbon concentration mechanisms of knockout lines, suggesting that these

914 differences were not caused by N, P or CO_2 limitation in the control lines

915 (**Supplemental Dataset S5,** sheets 4-5) (McCarthy, Smith et al. 2017, Nawaly,

916 Matsui et al. 2023). We further did not measure differences in photosynthetic

917 performance (electron transport), or an upregulation of genes encoding proteins

918 involved in photoprotection, e.g., LhcX family or xanthophyll cycle enzymes in

919 knockout lines under 19C CL (**Fig. 5B**; **Fig. S15**; **Supplemental Dataset S4,** sheet

920 12) (Buck, Sherman et al. 2019, Bai, Cao et al. 2022), suggesting that the differential

921 expression of photosynthesis genes in the knockout lines does not directly influence

922 photosynthesis.

923

924 In contrast, from RNAseq and qRPCR we observed an upregulation of multiple

925 mitochondrial NDH dehydrogenase and ATP synthase subunits; and downregulation

926 of TCA cycle enzymes in glycolysis knockout lines (**Fig. 5B; Supplemental Dataset**

927 **S5,** sheet 12). Our metabolomic data further show an underaccumulation of citric

928 acid, as per in 19LD conditions; but also arginine, synthesised in the diatom

929 mitochondria from glutamate and aspartate in the urea cycle (Allen, Dupont et al.

930 2011, Bromke 2013). We globally interpret these phenotypes to mean an increase in

931 mitochondrial respiratory electron transport in glycolysis knockout lines without

932 necessarily an increase in mitochondrial primary metabolic activity. Previous studies

933 have noted the important role of diatom mitochondria in dissipating excess plastid

934 reducing potential (Bromke 2013, Bailleul, Berne et al. 2015, Broddrick, Du et al.

935 2019), and we wonder if these phenotypes observed in knockout lines under 19C CL

936 conditions relate to the respiratory dissipation of plastidial NADPH.

937

938 It remains to be determined what routes beyond plastidial glycolysis contribute

939 substrates (e.g. PEP, pyruvate) to the *P. tricornutum* pyruvate hub. Previous studies

940 have noted that diatom plastid triose phosphate transporters may be able to transport

941 PEP directly from the cytoplasm, and one of these (Phatr3_J54017) is indeed

942 upregulated in both cpEnolase and cpPGAM1A knockout lines under 19C CL

943 (**Supplemental Dataset S5**, sheet 3) (Moog, Nozawa et al. 2020, Liu, Storti et al.

944 2022). Elsewhere our data suggest that amino acids may modify the concentrations

945 of *P. tricornutum* plastid PEP and/or pyruvate. These data include the overexpression

946 of plastid alanine transaminase in cpPGAM1A knockouts (**Fig. 5B);** and the

28

947 overaccumulation in both knockout lines of amino acids synthesised either from

948 pyruvate (valine), PEP (aspartate via PEP carboxylase, and methionine from

949 aspartate), or more broadly involved in plastid amino acid recycling (ornithine and

950 glutamate, in the diatom plastid ornithine cycle) (Levering, Broddrick et al. 2016,

951 Smith, Dupont et al. 2019, Yu, Nakajima et al. 2022) (**Fig. 6**). The direction (import or

952 export) and significance of these amino acid fluxes will be best determined e.g. with

953 an inducible knockout mutant compromised for both plastidial glycolysis and amino

954 acid incorporation (e.g., via nitrate reductase) to allow direct metabolic quantification

955 of *de novo* synthesised amino acids (McCarthy, Smith et al. 2017, Yin and Hu 2023).

956

957 Under 8C CL, we identify an over-accumulation of mRNAs encoding plastid

958 biogenesis and mitochondrial glycolytic proteins, an over-accumulation of short-chain

959 amino acids (valine) and an under-accumulation of cytoplasmic sugars and amino

960 acids (glucose, histidine) in cpEnolase and cpPGAM1A knockouts relative to controls

961 (**Figs. 5B, 5**). We further note under-accumulations of pyruvate in both knockout

962 lines (**Fig. 6**). Knockout lines under 8C conditions, however, have additional

963 phenotypes not observed at 19C. These include an overall enrichment in down-

964 regulated genes encoding plastid-targeted proteins (**Fig. 5A**); and a specific over-

965 accumulation of TCA cycle (citrate synthase) and a possible non-photochemical

966 quenching-associated mRNA (*LhcX4*) (**Fig. 5B**) (Bailleul, Berne et al. 2015, Murik,

967 Tirichine et al. 2019). Finally, specific differences are observed between cpEnolase

968 and cpPGAM1A knockout lines at 8C. These include an overaccumulation of TAGs

969 and SGDQs over glucosyl-lipids, and the over-accumulation of aspartate and

970 phenylalanine in cpEnolase knockouts only (**Figs. 6, 7; S17**).

971

972 The more complex phenotypes observed in our knockout lines at 8C, and particularly

973 the differences between cpPGAM1A and cpEnolase knockouts, may be due to

974 several reasons. PGAM is typically viewed to have a greater catalytic activity than

975 Enolase from biochemical studies, although this may be compensated by the greater

976 relative abundance of cpEnolase than cpPGAM1A in *Phaeodactylum* plastids (**Fig.**

977 **S6A**) (Scrutton and Utter 1968, Huang, Pan et al. 2024). It is true that cpPGAM1A

978 may be compensated by functionally redundant proteins (cpPGAM1B, cpPGAM2) in

979 the *Phaeodactylum* plastid in knockout lines, whereas cpEnolase is functionally non-

980 redundant, but none of these genes are specifically induced in RNAseq data of

29

981 cpPGAM1A knockouts under 8C CL (**Supplemental Dataset S5**, sheet 3)

982 suggesting an absent of specific compensation in the cpPGAM1A mutant line. We

983 note that several of the phenotypes associated with 8C CL, and with cpEnolase

984 knockouts specifically, relate to accumulation either of acyl-coA (TAGs) or PEP

985 (aspartate, phenylalanine), which may suggest impediment of the gluconeogenic

986 rather than glycolytic activity of cpEnolase and cpPGAM. The reversibility of the

987 cpPGAM1A and cpEnolase reaction is confirmed by enzymatic data (**Fig. 8**), and it

988 remains to be determined to what extent these enzymes function bidirectionally *in*

989 *vivo*. It also remains to be determined how these functions impact on growth kinetics

990 and viability of diatoms in the wild, given the limited differences in growth rate

991 observed in the lab between knockout and control lines (**Fig. 4**).

992

993 The complex phenotypes for diatom plastid glycolysis inferred from environmental

994 and experimental data contrast with those for plant plastid glycolysis, with (for

995 example) *A. thaliana* cpEnolase and cpPGAM mutants presenting relatively limited

996 phenotypes (Prabhakar, Löttgert et al. 2009, Andriotis, Kruger et al. 2010). We note

997 that the cytoplasmic and respiratory plant Enolase and PGAM1 isoforms, alongside

998 having predominant impacts on plant carbon flux, also have important moonlighting

999 roles in plant development, immune responses and even in the structural

1000 coordination of plastids and mitochondria (Zhao and Assmann 2011, Zhang,

1001 Sampathkumar et al. 2020, Yang, Wang et al. 2022). We similarly anticipate that

1002 further surprises will be identified for the functions of diatom plastid glycolysis, and for

1003 this still poorly understood pathway in the photosynthetic tree of life.

1004

1005 **Materials and Methods**

1006

1007 *Culture conditions*

1008

1009 *Phaeodactylum tricornutum* strain Pt1.86 was grown in enhanced seawater (ESAW)

1010 medium supplemented with vitamins, but without silicon or added antibiotics, in 50 μE

1011 $m^{-2} s^{-1}$ white light. Light profiles were measured with a SpectraPen photofluorometer

1012 (Photon Systems Instruments, Czech Republic); and are provided in **Supplemental**

1013 **Dataset S4**, sheet 13. Cultures were grown under one of four light, temperature and

1014 shaking regimes. For general molecular work and transformation, cultures were

30

1015 grown under 19 °C with 12h light: 12 dark cycling, shaken at 100 rpm (for general

1016 molecular work and transformation), following the established methodology of

1017 Falciatore et al. (Falciatore, Casotti et al. 1999). For comparative physiology work,

1018 we were unable to replicate shaking conditions at low temperatures, and therefore

1019 chose to use conditions without shaking: 19 °C with 12 h light: 12 h dark cycling

1020 (« LD » growth conditions and physiological analysis); 19 °C with 24 h continuous

1021 light and without shaking (« CL » growth conditions and physiological analysis); or

1022 8°C with 24h continuous light and without shaking (« 8C » growth conditions and

1023 physiological analysis). All cultures achieved measured mid exponential Fv/Fm

1024 values of > 0.6, suggesting that the absence of shaking did not impact on

1025 photosynthetic efficiency (**Supplemental Dataset S5**, sheet 8).

1026

1027 Batch culturing of *P. tricornutum* for genetic manipulation was performed under

1028 fluorescent lamps. Physiological experiments were principally performed at 19°C in

1029 an AlgaeTron AG230 (Photon Systems Instruments) with cool white LED (WIR)

1030 illumination, and technical specifications described in https://growth-

1031 chambers.com/data/algaetron-ag-230/download/AlgaeTron_AG_230_Manual2021-

1032 finalweb.pdf . Growth experiments were performed at 8°C using a low-temperature

1033 adapted cool white LED (WIR, ECCLIM). Details of all three spectra used, as

1034 measured with a SpectraPen (PSI), are provided in **Table S4**, sheet 13.

1035

1036 Mutant *P. tricornutum* lines were maintained on ½ ESAW 1% agarose plates,

1037 supplemented by 100 µg ml^{-1} each ampicillin and streptomycin, and 30 µg ml^{-1}

1038 chloramphenicol, and either 100 µg ml^{-1} zeocin (single transformants), or 100 µg ml^{-1}

1039 zeocin and 4 µg ml^{-1} blasticidin (complementation lines), as previously described

1040 (Falciatore, Casotti et al. 1999, Buck, Río Bártulos et al. 2018). All functional

1041 analyses of transformant lines were performed on transformant lines grown in the

1042 absence of antibiotic selection, to avoid secondary effects on growth or physiology.

1043

1044 *Phylogenetic identification of plastid lower half glycolysis-gluconeogenesis enzymes*

1045

1046 Plastid-targeted glycolysis lower half enzymes were searched across 1,673 plant and

1047 algal genomes and transcriptomes (**Dataset S1**, sheet 1). Briefly, this involved

1048 searching all annotated *P. tricornutum* PGAM (Phatr3_J17086, Phatr3_J51404,

31

1049   Phatr3_J5605, Phatr3_J5629, Phatr3_J8982, Phatr3_J37201, Phatr3_J47096) and

1050   enolase (Phatr3_draftJ1192, Phatr3_draftJ1572, Phatr3_J41515) peptide sequences

1051   with BLASTp and a threshold e-value of 10^{-05}, and a reciprocal BLASTp with criteria -

1052   max_target_seqs 1 to retrieve the best homologues against the entire *P. tricornutum*

1053   genome. For PGAM, where *P. tricornutum* queries failed to retrieve homologues in

1054   >50% searched libraries, a second BLASTp was performed with query peptide

1055   sequences from *A. thaliana* (AT2G17280, AT1G09780, AT3G05170, AT3G08590,

1056   AT3G50520, AT5G04120, AT5G64460), and a reciprocal BLASTp was performed

1057   with the *P. tricornutum* genome supplemented with these sequences. Similar

1058   approaches were subsequently used to identify equivalent plastid glycolysis proteins

1059   from *Tara* Oceans meta-genome assembled genomes (MAGs), as assembled in

1060   (Delmont, Gaia et al. 2022).

1061

1062   The domain content of each potential homologue was identified using hmmscan and

1063   the version 33.1 Pfam database (Mistry, Chuguransky et al. 2020). Only Enolase

1064   sequences that contained >90% predicted domain coverage to both Enolase_N and

1065   Enolase_C domains; and PGAM sequences that contained >50% domain coverage

1066   to the His_Phos domain (based on the corresponding coverage observed in *P.*

1067   *tricornutum* sequences) were viewed as being complete. Sequences for which the N-

1068   terminus of the region homologous to the PFAM domain was located within the first

1069   20 aa of the predicted sequence (i.e., less than the length of a typical plastid-

1070   targeting sequence) (Emanuelsson, Brunak et al. 2007) were viewed as lacking

1071   credible targeting sequences. All remaining proteins were scanned, considering both

1072   complete proteins and sequences trimmed to the first encoded N-terminal

1073   methionine, using targetp (using a plant scoring matrix) (Emanuelsson, Brunak et al.

1074   2007), PredAlgo (Tardif, Atteia et al. 2012), HECTAR (Gschloessl, Guermeur et al.

1075   2008) and ASAFind (with SignalP 5.0) (Gruber, Rocap et al. 2015, Almagro

1076   Armenteros, Tsirigos et al. 2019). Sequences from primary plastid-containing

1077   organisms (plants, green and red algae, glaucophytes) that were inferred to possess

1078   a plastid-targeting sequence either with TargetP or PredAlgo, and sequences from

1079   secondary plastid-containing organisms that were inferred to possess a plastid-

1080   targeting sequence with either HECTAR or ASAFind, considering both complete and

1081   N-trimmed sequence models, were annotated as putatively plastid-targeted.

1082

32

1083 A more detailed phylogenetic analysis was performed using Enolase and PGAM

1084 homologues obtained from a subset of 289 complete cryptomonad, haptophyte and

1085 stramenopile genomes and transcriptomes in the above library, alongside

1086 homologues identified from a further 85 prokaryotic and eukaryotic genomes

1087 sampled with taxonomic balance from across the remainder of the tree of life (Liu,

1088 Storti et al. 2022). Sequences were also screened for mitochondrial presequences

1089 using HECTAR (Gschloessl, Guermeur et al. 2008), and MitoFates, run with

1090 threshold value 0.35 (Fukasawa, Tsuji et al. 2015).

1091

1092 The pooled set of sequences were aligned first with MAFFT v 7.0 under the --auto

1093 setting, followed by the in-built alignment programme in GeneIOUS v 10.0.9, under

1094 default settings (Kearse, Moir et al. 2012, Katoh, Rozewicki et al. 2017). Incomplete

1095 and poorly aligned sequences, alongside taxonomically uninformative N- and C-

1096 terminal regions were removed from the alignment manually, followed by trimal with

1097 setting –gt 0.5 (Capella-Gutiérrez, Silla-Martínez et al. 2009). Phylogenetic analyses

1098 were performed with MrBayes v 3.2 and rAxML v 8, integrated into the CIPRES

1099 webserver (Stamatakis 2014, Miller, Schwartz et al. 2015). MrBayes trees were run

1100 for 10,000,000 generations with the GTR, Jones and WAG substitution matrices, 4

1101 starting chains and sumt and sump burnin fractions set to -0.5; all cold chains were

1102 confirmed to have reached a pvalue plateau below 0.1 prior to the start of the

1103 consensus building. rAxML trees were run with GTR, JTT and WAG substitution

1104 matrices, 350-400 ML generations, and automatic bootstopping. Phylogenies were

1105 either rooted between bacterial and eukaryotic sequences (Enolase); or on the mid-

1106 point (PGAM1, PGAM2) due to the absence of a single monophyletic bacterial

1107 outgroup. A summary of these analyses is provided in **Supplemental Dataset S1**.

1108

1109 Analysis of previously published *Phaeodactylum* data

1110

1111 First, the mean relative abundance of peptides corresponding to Enolase and PGAM

1112 sequences was retrieved from published mass spectrometry data of *Phaeodactylum*

1113 plastid-enriched fractions and total cell pellets, following (Huang, Pan et al. 2024).

1114 The two datasets were found to show a positive correlation with one another (r=

1115 0.891, n = 901, P < 10^{-05}) considering all proteins recovered in the plastid-associated

1116 fraction with a previously suspected plastid localisation (plastid-encoded, or plastid-

1117   targeted nucleus-encoded proteins inferred using combined ASAFind and HECTAR

1118   predictions). These data are provided in **Supplemental Dataset S2**, sheet 1.

1119

1120   Next, the expression trends of *Phaeodactylum* plastid glycolysis proteins (cpEnolase,

1121   cpPGAM1A, PGAM2) were assessed in combat normalised RNAseq data (Ait-

1122   Mohamed, Novák Vanclová et al. 2020) assembled from three prior studies, relating

1123   to induced nitrate limitation (nitrate reductase knockout), phosphate limitation and

1124   resupply, and iron limitation over a Circadian cycle (Cruz de Carvalho, Sun et al.

1125   2016, Smith, Gillard et al. 2016, McCarthy, Smith et al. 2017). A second set of

1126   comparisons were performed using normalised *Phaeodactylum* microarray data

1127   (summarised in (Ashworth, Turkarslan et al. 2016), particularly relating to changes in

1128   light quality, wavelength and Circadian time point. To enable global analyses of

1129   coregulation to cpEnolase and cpPGAM enzymes, these two datasets were

1130   converted into ranked values (i.e., for Spearman correlation) and merged, following

1131   (Liu, Storti et al. 2022). These data are summarised in **Supplemental Dataset S2**,

1132   sheets 2-4.

1133

1134   *Tara* Oceans Analysis

1135

1136   The complete *Tara* Oceans and *Tara* Oceans Polar Circle libraries of meta-genome

1137   and meta-transcriptome diversity (Carradec, Pelletier et al. 2018, Royo-Llonch,

1138   Sánchez et al. 2020) were searched for orthologues of diatom cpEnolase,

1139   cpPGAM1A and PGAM2 sequences via a phylogenetic reconciliation approach

1140   benchmarked in previous studies (Kazamia, Sutak et al. 2018, Liu, Storti et al. 2022).

1141   This approach uses the combined outputs of hmmer, BLAST best-hit, and single-

1142   gene tree topologies to only retain *Tara* Oceans meta-genes that reconcile as

1143   monophyletic with a defined query set, in these case plastid-targeted diatom isoforms

1144   of each enzyme. Exemplar tree topologies are shown in **Fig. S8.**

1145

1146   First, a HMM (hidden Markov model) was constructed for all diatom plastid-targeted

1147   sequences in the untrimmed alignments for each phylogeny, as detailed above, and

1148   searched into the complete *Tara* Oceans catalog by hmmer (http://hmmer.org) with

1149   evalue 10^{-10} to identify putative meta-gene homologues of each protein. Matching

1150   sequences were extracted, and searched by BLASTp against the complete copy of

34

1151   the *P. tricornutum* genome (Rastogi, Maheswari et al. 2018). Only sequences that

1152   retrieved a best hit against an Enolase or PGAM sequence (and therefore likely

1153   correspond to homologues of each protein) were retained. Next, the retained

1154   sequences were similarly searched by BLASTp against the complete untrimmed

1155   alignment of cultured Enolase and PGAM sequences. Only sequences that retrieved

1156   a diatom plastid-targeted isoform were retained, allowing the elimination of non-

1157   diatom and homologues of diatom non-plastid sequences. Finally, sequences were

1158   combined with the untrimmed alignment of cultured sequences from each gene and

1159   realigned using the same MAFFT, GeneIOUS and trimal pipeline as defined above.

1160   Curated alignments were screened by rAxML tree with the JTT substitution matrix, as

1161   above. Only *Tara* Oceans sequences that resolved within a monophyletic clade with

1162   diatom plastid-targeted proteins, defined as all sequences that position closer on a

1163   midpoint rooting of the tree to diatom plastid-targeted proteins than to any non-

1164   diatom or non-plastid targeted sequences, were extracted for further analyses.

1165

1166   Relative abundances were calculated for the total occurrence of all phylogenetically

1167   verified diatom plastid-targeted proteins in both meta-transcriptome and meta-

1168   genome data. Relative expression levels of each gene were estimated by reconciling

1169   the calculated meta-transcriptome abundances either to total diatom meta-

1170   transcriptome sequences using the formula $10^{\wedge 6}(\Sigma_{metaT}/ \Sigma_{DiatomT})$, i.e., expressed per

1171   million reconciled diatom reads, or to calculated meta-genome abundances, using

1172   the formula and $\log_{10}(1+ \Sigma_{metaT}) - \log_{10}(1+ \Sigma_{metaG})$, to allow inclusion of zero metaG

1173   values. Pearson and Spearman correlations were calculated between relative

1174   abundances and all quantitative measured environmental variables associated with

1175   *Tara* Oceans samples as stored within the PANGAEA repository (Pesant, Not et al.

1176   2015). All calculations were repeated independently for each depth (surface, or deep

1177   chlorophyll maximum/ DCM) and size fraction (0.8- 2000 μm, 0.8- 5 μm, 3/5- 20 μm,

1178   20- 180 μm, and 180- 2000 μm), with 3 and 5 μm filters viewed as equivalent to allow

1179   reconciliation of Arctic and non-Arctic data, respectively. All *Tara* Oceans meta-gene

1180   assignations, alongside individual and total abundance calculations are provided in

1181   **Supplemental Dataset S3**, sheets 1-10.

1182

1183   *Tara* Oceans MAGs were partitioned into those that contained credible chloroplast-

1184   targeted copies of Enolase and/ or PGAM sequences, using a similar reciprocal

35

1185   BLAST best-hit, PFAM analysis and *in silico* targeting prediction pipeline as used for

1186   cultured species data (**Supplemental Dataset S3**, sheet 11). MAGs were partitioned

1187   into those containing both identifiable chloroplast-targeted Enolase and PGAM

1188   enzymes; one only; and neither. The mean mapped vertical depth (analogous to

1189   abundance) was calculated for each MAG from 0.8-2000 μm data at DCM and

1190   surface depths, following data from (Delmont, Gaia et al. 2022), and was compared

1191   to absolute station latitude by Pearson correlation and two-tailed *t*-test.

1192

1193   *Nucleic acid isolation*

1194

1195   For DNA isolation, 150 ml early stationary phase *P. tricornutum* culture, grown under

1196   19°C with 12h light: 12h dark cycling, and shaken at 100 rpm as described above,

1197   was centrifuged at 4000 rpm for 10 minutes. The resulting cell pellet was washed in

1198   sterile growth medium three times, and incubated for four hours in 5 ml TEN buffer

1199   (0.1 M NaCl, 0.01 M Tris pH8, 0.001 M EDTA) supplemented with 2% volume:

1200   volume SDS, and 1U μl^{-1} proteinase K (Fisher Scientific). Lysed cell fractions were

1201   used for phenol: chloroform precipitation of cellular DNA, as previously described

1202   (Nash, Barbrook et al. 2007), prior to dissolution in 50 μl nuclease-free water, and

1203   quantification with a nanodrop photospectrometer.

1204

1205   For RNA isolations, 10^5 stationary phase *P. tricornutum* cells, as calculated with cell

1206   densities counted from a Malassez haemocytometer were inoculated in a 250 ml

1207   conical Erlenmeyer containing 80 ml ESAW without antibiotics. Cell cultures were

1208   harvested in mid-exponential phase, at counted densities of between 1 and 2 x 10^6

1209   cells ml^{-1}. 19C CL cultures were typically harvested eight days post-inoculation, 19C

1210   LD cultures nine days post-inoculation, and 8C CL cultures seventeen days post-

1211   inoculation, in agreement with growth curve dynamics. Cells were harvested at the

1212   mid-point of the light-induction phase of the LD growth condition (15:00 CET), per

1213   previous gene expression studies in *P. tricornutum* (Cruz de Carvalho, Sun et al.

1214   2016).

1215

1216   RNA was isolated from 10^8 cells from each culture, pelleted and washed as before,

1217   and snap-frozen in liquid nitrogen. Frozen cell suspensions were re-equilibrated with

1218   1 ml Trizol reagent (Invivogen) and 200 μl chloroform (Honeywell), prior to phenol:

1219   chloroform extraction. An additional separation step was performed in 500 µl pure

1220   chloroform to remove any residual phenol traces from the aqueous phase, and

1221   purified nucleic acids were precipitated overnight in 500 µl isopropanol at -20°C. RNA

1222   was collected by centrifugation at 10,000 rpm for 30 minutes, washed with 900 µl

1223   100% ethanol, and resupended in 50 µl RNAse-free water (Qiagen).

1224

1225   2 µg RNA, as quantified with a nanodrop photospectrometer, was subsequently

1226   treated with 2U RNAse-free DNAse (Promega) for 30 minutes at 37 °C, and the

1227   reaction was stopped with 1 µl 0.5 M EDTA. The digested RNA sample was

1228   reprecipitated in isopropanol for one hour at -20 °C, washed in ethanol, and

1229   resuspended in 20 µl RNAse-free water. Purified RNA sample concentrations were

1230   quantified with a nanodrop spectrometer, and a 3 µl aliquot was migrated on an

1231   RNAse-free 1% agarose gel stained with 0.2 µg ml^{-1} ethidium bromide to confirm

1232   RNA integrity prior to all downstream applications.

1233

1234   *GFP localization*

1235

1236   Full length mRNA sequences of cpEnolase, cpPGAM1A and cpPGAM2 were

1237   amplified from *P. tricornutum* RNA libraries grown under 19 °C, light: dark cycling and

1238   replete nutrient conditions as described above, by reverse transcription with RT

1239   Maxima First Strand synthesis kit (Thermo Fisher) from 200 ng template RNA,

1240   following the manufacturer's instructions; and gene-specific primers as shown in

1241   **Supplemental Dataset S2**, sheet 4. PCRs were performed using Pfu high-fidelity

1242   DNA polymerase, in 50 µl total reaction volume, including 1 µl cDNA template and 2

1243   µl each specific primer, following the manufacturer's protocol. Typical PCR conditions

1244   were: 10 minutes at 95 °C; followed by 35 cycles of 45 seconds at 95 °C, 45 seconds

1245   at 55 °C, and 2 minutes at 72 °C; followed by a terminal elongation phase of 5

1246   minutes at 72 °C. Amplified products were migrated on a 1% agarose gel stained

1247   with ethidium bromide, cut out, and purified using a MinElute PCR purification kit

1248   (Qiagen).

1249

1250   Purified products were cloned into linearised versions of pPhat vectors containing

1251   eGFP and a zeocin resistance gene (SHBLE). These products were amplified using

1252   an analogous PCR protocol as above, with 1 ng purified plasmid DNA, and outward-

1253   directed PCR primers extending from the start of the fluorescence protein gene

1254   sequence to the end of the FcpA promoter region (**Supplemental Dataset S2**, sheet

1255   4); cut, purified, and treated with 1U FastDigest DpnI (Thermo Fisher) to remove any

1256   residual plasmid DNA. The gene-specific primers for each cpEnolase and cpPGAM

1257   construct were modified with 15 5' nucleotides complementary to the terminal regions

1258   of the FcpA and GFP sequences, allowing cloning of complete vector sequences

1259   using a HiFi DNA assembly kit (NEB), following the manufacturer's instructions.

1260   Assembled vectors were transformed into chemically competent Top10 *E. coli*, and

1261   positive clones (as identified by Sanger sequencing of positive colony PCR products)

1262   were used to generate purified plasmid DNA with a Plasmid Midi Kit (Qiagen).

1263

1264   Subcellular localization constructs were transformed into wild type *P. tricornutum*

1265   Pt186 by biolistic transformation, as previously described (Falciatore, Casotti et al.

1266   1999). 5 x 10^7 mid-exponential phase cells were plated on a ½ ESAW- 1% agarose

1267   plate, and left to recover for two days, prior to bombardment with 10 mg 1 µm

1268   tungsten beads treated with 5 µg purified plasmid DNA in a Helios gene gun

1269   (BioRad) at 1,550 PSI. Cells were left to recover for two days, prior to replating on ½

1270   ESAW- 1% agarose plates supplemented with 100 µg ml^{-1} ampicillin, 100 µg ml^{-1}

1271   streptomycin, 30 µg ml^{-1} chloramphenicol and 100 µg ml^{-1} zeocin. Plates post-

1272   bombardment and for the first two days post-selection were maintained in a low light

1273   environment (10 µE m^{-2} s^{-1}) prior to return to standard growth conditions.

1274

1275   Positive transformant colonies, as verified by Western Blot with a mouse anti-GFP

1276   antibody (Thermo Fisher), were visualised using a SP8 inverted spinning disc

1277   confocal microscopy (Leica) under 400 x magnification, with excitation wavelength

1278   485 nm and emission wavelength filters 500-550 nm. GFP-negative colonies were

1279   used to confirm detection specificity, and empty-vector GFP (with cytoplasmic

1280   localizations) were used as fluorescence positive controls. A minimum of 12 GFP

1281   expressing clones were visualised for each construct with consistent localization.

1282

1283   *CRISPR mutagenesis*

1284

1285   CRISPR target sequences for cpEnolase and cpPGAM1A genes were identified

1286   using PhytoCRISP-Ex (Rastogi, Murik et al. 2016), privileging positions in the N-

1287   terminal region of the conserved domain to minimize the probability of enzyme

1288   functionality in knockout lines, and uniqueness across the entire *P. tricornutum*

1289   genome within the final 11 bp of the target sequence to minimize off-target effects.

1290   Primers were designed for each target sequence, and introduced into a pu6:SG1

1291   CRISPR target sequence plasmid by PCR, as previously described (Nymark,

1292   Sharma et al. 2016). 2 µg insertion-positive pu6:SG1 plasmids, as confirmed by

1293   Sanger sequencing were co-introduced into wild type *P. tricornutum* Pt186 cells by

1294   bombardment along with 2 µg HA-tagged Cas9 and pPhat vectors, as described

1295   above. Mutant colonies were genotyped using a DNA lysis buffer containing 0.14 M

1296   NaCl, 5 mM KCl, 10 mM Tris-HCl pH 7.5, 1% v/v NP40 to generate crude DNA

1297   extracts, followed by PCR amplification across the CRISPR target sequences with

1298   DreamTaq PCR reagent (Promega) and Sanger sequencing (Eurofins genomics).

1299   Mixed mutant: wild-type colonies were segregated via repeated dilution on ESAW:

1300   zeocin plates until only homozygous mutant genotypes were detected (Nymark,

1301   Sharma et al. 2016, McCarthy, Smith et al. 2017). Empty vector control lines were

1302   generated using the same protocol, except with only HA-Cas9 and pPhat plasmids,

1303   cotransformed without a CRISPR target sequence.

1304

1305   Tabulated cleaned knockout mutants, their associated genotypes and the expression

1306   levels of mutated gene copies are shown in **Supplemental Dataset S4**, sheets 1-2.

1307   Mutant colony genotypes were periodically confirmed (approx. once per month) by

1308   PCR and Sanger sequencing throughout the duration of all subsequent experiments,

1309   and the CRISPR-induced gene modifications were found to remain stable. *P.*

1310   *tricornutum* Enolase proteins were determined by Western blot to be crossreactive to

1311   an anti-*Arabidopsis thaliana* Enolase-2 antibody (Agrisera), and thus knockout line

1312   protein expression was confirmed by qRT-PCR, as described below.

1313

1314   *Complementation of knockout lines*

1315

1316   Knockout lines were complemented with pPhat:GFP vectors carrying overexpressing

1317   copies (under an FcpA promoter) of cpEnolase and cpPGAM1A synthetic constructs,

1318   with all CRISPR target sequences replaced with silent mutations (Eurofins). Genes

1319   were fused to C-terminal GFP, allowing the verification of protein expression and

1320   localization. Vectors were identical to those previously used for localization, but with

39

1321   a blasticidin S-deaminase gene in lieu of SHBLE (Buck, Río Bártulos et al. 2018)

1322   introduced by NEB Hi-Fi kit as before. Complementation constructs were transformed

1323   via bombardment, and cotransformed colonies were selected on ½ ESAW- 1%

1324   agarose plates supplemented with 100 μg ml^{-1} ampicillin, 100 μg ml^{-1} streptomycin,

1325   30 μg ml^{-1} chloramphenicol, 100 μg ml^{-1} zeocin, 4 μg ml^{-1} blasticidin.

1326

1327   For each complementation, three cpEnolase and cpPGAM1A knockout lines

1328   (including at least one for each CRISPR target sequence) were complemented both

1329   with the conjugate construct, and an empty blasticidin resistance vector as a placebo;

1330   and two empty vector lines were further complemented with both cpEnolase and

1331   cpPGAM1A overexpressor constructs, plus an empty blasticidin resistance vector, to

1332   exclude possible effects from ectopic overexpression of each gene on cell

1333   physiology. A total of 47 colonies, with a minimum of 6 colonies for each knockout:

1334   complementation combination, including lines complemented from at least two

1335   distinct primary knockout mutant genotypes, were selected for subsequent study

1336   (**Supplemental Dataset S4**, sheet 7). The retention of the primary knockout mutant

1337   genotype in each complemented line was verified by colony PCR and sequencing as

1338   above, and the overexpression and correct localization of the complementing protein

1339   sequence (i.e., to the chloroplast for cpEnolase:GFP and cpPGAM1:GFP, or the

1340   cytoplasm for ectopic GFP) was verified by western blot with an anti-GFP antibody

1341   (Thermo Fisher) (Erdene-Ochir, Shin et al. 2019) and confocal microscopy.

1342

1343   *Growth rate measurements*

1344

1345   A starting density of 10^4 ml^{-1} stationary phase *P. tricornutum* cells of a given culture

1346   line, as verified with a Malassez haemocytometer, were inoculated into a 15 ml

1347   volume antibiotic-free ESAW within a sterile, ventilated cap plastic culture flask

1348   (Celltreat) and grown under LD, CL, or 8C culture conditions as described. Cell

1349   densities were recorded: every day from one day post-inoculation (CL); every day

1350   from two days post-inoculation (LD); or every two days from five days post-

1351   inoculation (8C) at the mid-point of the LD light induction phase using a counting

1352   CyFlow Cube 8 cytometer (ParTec).

1353

1354   Typically, 15 µl cell culture, passed at 0.5 µl s^{-1}, were used for each measurement,

1355   with three technical replicates performed for each culture of which the first (enriched

1356   in non-cellular particles) was excluded from downstream calculations. Cytometer

1357   particle counts were correlated to actual cell densities using a calibration curve

1358   realised from haemocytometer counted densities of wild-type cell culture, and

1359   cultures with observed densities > 2×10^6 cells ml^{-1} were diluted ten-fold in blank

1360   growth media to avoid saturation of the cytometer.

1361

1362   Cell densities were measured until cell lines were confirmed to have exited log phase

1363   (i.e., reached a stationary phase plateau). Primary knockout mutant growth curves

1364   were repeated a minimum of six times (three biological replicates per-inoculation,

1365   with two independent repetitions) for each mutant line. Growth curves were tested for

1366   seven cpEnolase knockout, five cpPGAM1A knockout and four empty vector control

1367   lines, providing a minimum of 24 measurements (i.e., four distinct mutant lines) per

1368   each genotype studied (cpEnolase knockout, cpPGAM1A knockout and empty vector

1369   control lines).

1370

1371   To avoid artifacts based on the proximity of the seed cell culture to exponential phase

1372   at the time of inoculation (which may impact on lag phase length) or the relative

1373   diameter of each cell in culture (which may impact on carrying capacity), cell growth

1374   rates were measured exclusively from the log-phase relative division rate. This was

1375   calculated via considering $\Delta\log_2$ (cell density) / $\Delta\log_2$ (time) for a time-period

1376   corresponding to 5×10^4 to 4×10^6 cells/ ml, covering in most cases six successive

1377   measurements of each individual growth curve. To confirm that the cells were

1378   measured in exponential phase and were neither influenced by particle

1379   contamination of the cytometer or cell exhaustion of the growth medium, the linear

1380   correlation was calculated between the log value, with most calculated correlations

1381   (129/ 132) showing linearity (r> 0.95). Three exemplar growth curve outputs are

1382   provided in **Supplemental Dataset S4**, sheets 3-5; and an overview of relative

1383   growth rates expressed as a function of mean empty vector control growth rates are

1384   provided in **Supplemental Dataset S4**, sheet 6.

1385

1386   Complementation growth curves were repeated with at least two independent

1387   repetitions for each cell line, with five timepoints taken to project growth rates, and

1388   therefore a minimum of sixty independent measurements for each mutant:

1389   complementation genotype under each growth condition, with the average of the two

1390   fastest growth rates of each culture calculated as estimates for the growth rate. A

1391   heatmap of all estimated complementation line growth rates is provided in

1392   **Supplemental Dataset S4**, sheet 7.

1393

1394   *Photophysiology*

1395

1396   Cultures for photophysiological analysis were grown in 10ml ventilated plastic flasks,

1397   without shaking, under 19C CL and 19C LD as described above. Cultures were

1398   grown from a starting inoculum of 10^5 cells ml^{-1} as measured with a Malassez

1399   haemocytometer. Cell cultures that had reached a measured density of 10^6 cells ml^{-1}

1400   were then refreshed into fresh media at the initial starting concentration of 10^5 cells

1401 ml^{-1} to allow a prolonged adaptation to each photophysiological condition under a

1402   continuous exponential phase. Cells from refreshed culture lines were harvested in

1403   exponential phase (between 1 and 3×10^6 cells ml^{-1}, and good physiology was

1404   verified by Fv/Fm measurements > 0.6 across all measured lines (**Supplemental**

1405   **Dataset S4**, sheet 8).

1406

1407   Steady-state light curves (SSLC) were conducted with a fluorescence CCD camera

1408   recorder (SpeedZen, jBeamBio, France) in a selected set of control lines (n=2),

1409   cpPGAM (n=3) and cpEnolase knockouts (n=6), as well in complemented cpEnolase

1410   (n=2) and cpPGAM1A (n=3) knockout lines in which we observed a suppression of

1411   the knockout growth defect compared to complemented control lines. Measurements

1412   were repeated a minimum of two and in most cases four times per line and treatment

1413   condition, with a minimum of six unique measurements performed for each genotype

1414   and treatment. Curves were measured on cell cultures concentrated to between 2

1415   and 5×10^7 cells ml^{-1}. Samples were exposed to an initial 5 min illumination of 35

1416 μmol photons $m^{-2} s^{-1}$ green actinic light (532 nm), followed by a 6 steps of 3 min each

1417   of increasing intensity to 750 μmol photons $m^{-2} s^{-1}$.

1418

1419   Minimum (F_0) and maximum (F_M) fluorescence were measured in dark-adapted (at

1420   least 1 min) samples, before and at the end of a 250 ms saturating (multiple turnover)

1421   pulse of light (532 nm, 5000 μmol photons $m^{-2} s^{-1}$) and the maximum quantum yield

1422   of PSII in the dark was calculated as $F_V/F_M = (F_M - F_0)/F_M$. Every minute of light

1423   exposure, steady-state fluorescence (F_S) and maximum fluorescence under Light

1424   (F_M') were measured. PSII quantum yield (φPSII) and nonphotochemical quenching

1425   (NPQ) were calculated on the last time point of each light step as φPSII = $(F_M'-F_s)/F_M'$

1426   and NPQ = $F_M/F_M'-1$, and rETR at PSII as rETR = φPSII.E.

1427

1428   The whole rETR vs E curve was fitted as rETR = $rETR_M.(1-exp(-α.E/rETR_M))$ where

1429 $rETR_M$ is the maximum rETR and α is the light-limited slope of rETR vs E (Jassby and

1430   Platt 1976). Only rETR values from 0 to 450 µmol photons m^{-2} were used for the fit

1431   because values from 600 and 750 µmol photons m^{-2} were too noisy. The light

1432   saturation parameter E_K was calculated as $rETR_M/α$ and the fitted values of the

1433   parameters were used to estimate φPSII under the growth light intensity of 50 µmol

1434   photons m^{-2} s^{-1} as $φPSII_{50µE}= (rETR_M.(1-exp(-α.50/rETR_M)))/ 50$. The NPQ vs E curve

1435   was fitted as NPQ = $NPQ_M × E^n/ (E_{50}NPQ^n+E^n)$, where NPQ_M is the maximal NPQ,

1436 $E_{50}NPQ$ is the half- saturation intensity for NPQ and n is the sigmoidicity coefficient

1437   (Serôdio and Lavaud 2011).

1438

1439   The PSII functional absorption cross-section, σPSII, was calculated from the

1440   fluorescence induction upon a single turnover flash of blue light (100 µs, 455 nm, 60

1441   nm bandwidth) on non-concentrated cell culture. The induction curve was measured

1442   on 20 min dark-acclimated samples before centrifugation (average of 2-4

1443   independent replicates) with a Fluorescence Induction and Relaxation (miniFIRe)

1444   fluorometer (Gorbunov, Shirsin et al. 2020), which also measures single turnover

1445 F_V/F_M and PSII connectivity. Parameters measured with the miniFIRe fluorometer (as

1446   defined below) were also quantified for cultures grown under 8C CL, as the

1447   measurements were sufficiently rapid to allow the culture to be maintained at growth

1448   temperatures (Gorbunov, Shirsin et al. 2020). Measured photophysiological values

1449   are tabulated in **Supplemental Dataset S4**, sheet 8. Violin plots of

1450   photophysiological parameters were generated with BoxPlotR (Spitzer, Wildenhain et

1451   al. 2014).

1452

1453   *Gene expression analysis*

1454

1455   Libraries were prepared from 200 ng DNAse-treated RNA for each mutant line and

1456   treatment condition, with at least three replicates per sample. Sequencing was

1457   performed by Fasteris (Plan-les-Ouates, Switzerland). After initial quality control

1458   checks, stranded Illumina mRNA libraries were prepared with a Novaseq V1.5 kit and

1459   sequenced with an SP-flow cell with 2x 100 bp over 200 cycles, yielding circa 130-

1460   160 Gb sequence data per sample with ≥85% of bases higher than Q30.

1461

1462   FastQ files were mapped using Nextflow's RNA sequencing assembly pipeline

1463   https://nf-co.re/rnaseq/usage, to gff3 annotations of the *P. tricornutum* version 3

1464   genome (Rastogi, Maheswari et al. 2018, Lataretu and Hölzer 2020). Total mapped

1465   read counts were then compared between all biological and technical replicates for (i)

1466   each mutant line sequenced, (ii) each genotype (cpEnolase knockout, cpPGAM1A

1467   knockout, control), and (iii) each treatment condition performed (LD, CL, 8C) by

1468   principal component analysis (PCA) using the R package factoextra, with highly

1469   variant libraries removed (Kassambara and Mundt 2017). The final dataset included

1470   63 RNAseq libraries, including five cpEnolase and five cpPGAM1A knockout lines

1471   and four empty vector controls, and a minimum of four RNA libraries prepared from

1472   at least two genetically distinct mutant constructs for each genotype (cpEnolase,

1473   cpPGAM1A and control) considered (**Supplemental Dataset S5**, sheets 1-2).,

1474   Differentially expressed genes (DEGs) were then calculated between each genotype

1475   for each treatment condition using DESeq2 with cutoff fold-change 2 and P-value

1476   0.05 (Liu, Wang et al. 2021) (**Supplemental Dataset S5**, sheets 2-3).

1477

1478   The mean transcript abundances of DEGs in knockout compared to control lines

1479   were first assessed in RNAseq data of N and P-limited *P. tricornutum* cell lines under

1480   two and nine time-points respectively (**Supplemental Dataset S5**, sheet 4) (Cruz de

1481   Carvalho, Sun et al. 2016, McCarthy, Smith et al. 2017). No significant differences

1482   were found between DEGs and other genes in the *P. tricornutum* genome (one-way

1483   ANOVA, P > 0.05; **Supplemental Dataset S5**, sheet 5), confirming that the RNAseq

1484   samples were not generated from N- or P-limited cultures. Next, functional

1485   enrichments in DEGs from previously tabulated values for the entire *P. tricornutum*

1486   genome (**Supplemental Dataset S5**, sheets 6-10) (Rastogi, Maheswari et al. 2018,

1487   Ait-Mohamed, Novák Vanclová et al. 2020). Functional enrichments were tested by

1488   two-tailed chi-square (P < 0.05) of a differentially expressed gene occurring in either

1489   one (cpEnolase v control; cpPGAM1A v control) knockout-versus-control line tests, or

1490   in both tests realised under each physiological condition. Finally, the distribution of

1491   DEGs across *P. tricornutum* core plastid and mitochondrial metabolism pathways

1492   were mapped onto a previously defined proteomic model of each organelle (Ait-

1493   Mohamed, Novák Vanclová et al. 2020); with the strongest DEG enrichment taken in

1494   the case of enzymes with multiple homologues (**Supplemental Dataset S5**, sheet

1495   11).

1496

1497   Quantitative RT-PCR (qRT-PCR) validations were performed using cDNA

1498   synthesised from 5 ng dNase-treated RNA (per qRT-PCR reaction) and a RT

1499   Maxima First Strand synthesis kit (Thermo Fisher), following the manufacturer's

1500   instruction; using a 384-well Lightcycler (Roche) and Takyon™ No ROX SYBR 2X

1501   MasterMix (Eurogentec), following the manufacturers' protocols. Typical amplification

1502   conditions were: 10 minutes at 95°C, followed by 40 cycles of 30 seconds at 95°C,

1503   30 seconds at 55°C, and 30 seconds at 72°C. Primer pairs for qRT-PCR

1504   amplifications were designed using NCBI Primer-BLAST (Ye, Coulouris et al. 2012),

1505   privileging unique amplification targets within the genomic sequence, an amplicon

1506   size of 100 to 150 base pairs, primer positions at different regions of the gene

1507   studied, and a 3' terminal G or C on each primer. Primer efficiencies were tested by

1508   qPCR with serial dilutions of *P. tricornutum* gDNA, with only primer pairs that yielded

1509   a Cp increment of between 0.9 and 1.1 per half dilution of DNA retained for qRT-PCR

1510   analysis. qRT-PCRs were at least three times for each amplicon: sample pair. RT-

1511   equivalents were performed to subtract residual genomic DNA from each Cp value

1512   obtained, and two housekeeping genes (Ribosomal protein S1, RPS; and TATA

1513   binding protein, TBP) previously shown to have conditionally invariant expression

1514   patterns in *P. tricornutum* were used as quantification references (Sachse, Sturm et

1515   al. 2013). Tabulated qRT-PCR outputs are shown in **Supplemental Dataset S5**,

1516   sheet 13; and sample information and reaction conditions per MIQE guidelines

1517   (Bustin, Benes et al. 2009) are tabulated in **Supplemental Dataset S5**, sheet 14.

1518

1519   *Metabolite analysis*

1520

1521   Cell pellets were taken from exponential-phase *P. tricornutum* culture (counted

1522   density 1-2 x 10^6 cells ml^{-1}, 1.5 x 10^8 cells per sample) for metabolite and lipid

1523 analysis. Cell pellets were collected without washing to minimise impacts on

1524 metabolite turnover, then transferred to a pre-weighed, double-pierced and double-

1525 autoclaved 1.5 ml Eppendorf tube for lyophilization. Cell pellet masses were

1526 recorded, and samples were immediately snap-frozen in liquid nitrogen and stored at

1527 -80 °C for subsequent analysis.

1528

1529 Metabolite profiling was carried out by gas chromatography–mass spectrometry

1530 (ChromaTOF software, Pegasus driver 1.61; LECO) as described previously (Lisec,

1531 Schauer et al. 2006). The chromatograms and mass spectra were evaluated using

1532 TagFinder software (Luedemann, von Malotky et al. 2012). Metabolite identification

1533 was manually checked by the mass spectral and retention index collection of the

1534 Golm Metabolome Database (Kopka, Schauer et al. 2005). Peak heights of the mass

1535 fragments were normalized successively on the basis of the fresh weight of the

1536 sample, the added amount of an internal standard (ribitol) and values obtained for

1537 loading column controls obtained from the same experiment.

1538

1539 *Glycerolipid analysis*

1540

1541 Glycerolipids were extracted by suspending cell pellets in 4 mL of boiling ethanol for

1542 5 minutes to prevent lipid degradation. Lipids were extracted by addition of 2 mL

1543 methanol and 8 mL chloroform at room temperature (Folch, Lees et al. 1957). The

1544 mixture was then saturated with argon and stirred for 1 hour at room temperature.

1545 After filtration through glass wool, cell remains were rinsed with 3 mL

1546 chloroform/methanol 2:1, v/v and 5 mL of NaCl 1% was added to the filtrate to initiate

1547 biphase formation. The chloroform phase was dried under argon and stored at -20

1548 °C. The lipid extract was resuspended in pure chloroform when needed.

1549

1550 Total glycerolipids were quantified from their fatty acids: in an aliquot fraction, 5 µg of

1551 15:0 was added and the fatty acids present were converted to methyl esters (FAME)

1552 by a 1-hour incubation in 3 mL 2.5% H_2SO_4 in pure methanol at 100 °C (Jouhet,

1553 Maréchal et al. 2003). The reaction was stopped by addition of 3 mL water and 3 mL

1554 hexane. The hexane phase was analyzed by a gas chromatography-flame ionization

1555 detector (GC-FID) (Perkin Elmer) on a BPX70 (SGE) column. FAMEs were identified

1556   by comparison of their retention times with those of standards (Sigma) and quantified

1557   using 15:0 for calibration.

1558

1559   Glycerolipids were further analyzed by high pressure liquid chromatography-tandem

1560   mass spectrometry (HPLC-MS/MS), based on a previously described procedure

1561   (Rainteau, Humbert et al. 2012). The lipid extracts corresponding to 25 nmol of total

1562   fatty acids were dissolved in 100 µL of chloroform/methanol [2/1, (v/v)] containing

1563   125 pmol of each internal standard. Internal standards used were

1564   phosphatidylethanolamine (PE) 18:0-18:0 and diacylglycerol (DAG) 18:0-22:6 from

1565   Avanti Polar Lipid, and sulfoquinovosyldiacylglycerol (SQDG) 16:0-18:0 extracted

1566   from spinach thylakoids (Demé, Cataye et al. 2014) and hydrogenated (Buseman,

1567   Tamura et al. 2006). Lipid classes were separated using an Agilent 1200 HPLC

1568   system using a 150 mm × 3 mm (length × internal diameter) 5 µm diol column

1569   (Macherey-Nagel), at 40 °C. The mobile phases consisted of hexane/ isopropanol/

1570   water/ 1 M ammonium acetate, pH 5.3 [625/350/24/1, (v/v/v/v)] (A) and isopropanol/

1571   water/ 1 M ammonium acetate, pH 5.3 [850/149/1, (v/v/v)] (B). The injection volume

1572   was 20 µL. After 5 min, the percentage of B was increased linearly from 0% to 100%

1573   in 30 min and kept at 100% for 15 min. This elution sequence was followed by a

1574   return to 100% A in 5 min and an equilibration for 20 min with 100% A before the

1575   next injection, leading to a total runtime of 70 min. The flow rate of the mobile phase

1576   was 200 µL min^{-1}. The distinct glycerophospholipid classes were eluted successively

1577   as a function of the polar head group. Mass spectrometric analysis was performed on

1578   a 6460 triple quadrupole mass spectrometer (Agilent) equipped with a Jet stream

1579   electrospray ion source under following settings: drying gas heater at 260 °C, drying

1580   gas flow at 13 L·min^{-1}, sheath gas heater at 300 °C, sheath gas flow at 11 L·min^{-1},

1581   nebulizer pressure at 25 psi, capillary voltage at ± 5000 V and nozzle voltage at ±

1582   1,000 V. Nitrogen was used as the collision gas. The quadrupoles Q1 and Q3 were

1583   operated at widest and unit resolution, respectively.

1584

1585   Phosphatidylcholine (PC) and diacylglyceryl hydroxymethyltrimethyl-β-alanine

1586   (DGTA) analyses were carried out in positive ion modes by scanning for precursors

1587   of m/z 184 and 236 respectively at a collision energy (CE) of 34 and 52 eV. SQDG

1588   analysis was carried out in negative ion mode by scanning for precursors of m/z -225

1589   at a CE of -56eV. PE, phosphatidylinositol (PI), phosphatidylglycerol (PG),

1590   monogalactosyldiacylglycerol (MGDG) and digalactosyldiacylglycerol (DGDG)

1591   measurements were performed in positive ion modes by scanning for neutral losses

1592   of 141 Da, 277 Da, 189 Da, 179 Da and 341 Da at cEs of 20 eV, 12 eV, 16 eV, 8 eV

1593   and 8 eV, respectively. DAG and triacylglycerol (TAG) species were identified and

1594   quantified by multiple reaction monitoring (MRM) as singly charged ions [M+NH4]$^+$ at

1595   a CE of 16 and 22 eV respectively. Quantification was done for each lipid species by

1596   MRM with 50 ms dwell time with the various transitions previously recorded (Abida,

1597   Dolch et al. 2015). Mass spectra were processed using the MassHunter Workstation

1598   software (Agilent) for lipid identification and quantification. Lipid amounts (pmol) were

1599   corrected for response differences between internal standards and endogenous lipids

1600   as described previously (Jouhet, Lupette et al. 2017).

1601

1602   Normalised metabolite and lipid abundances were screened by PCA, as per the

1603   RNAseq analysis above, and outliers and biologically non-representative samples

1604   were removed. The final datasets consist of 139 libraries (metabolite GC-MS), 55

1605   libraries (lipid GC-MS) and 49 libraries (lipid LC-MS), with a minimum of three

1606   libraries prepared from at least two genetically distinct mutant constructs for each

1607   genotype considered (**Supplemental Dataset S6**, sheet 1). Violin plots of

1608   differentially accumulated lipids were generated with BoxPlotR (Spitzer, Wildenhain

1609   et al. 2014).

1610

1611   *Expressed enzyme reaction kinetics*

1612

1613   Measurements of cpEnolase and cpPGAM1A reaction rates were performed

1614   following a previously defined protocol (Zhang, Sampathkumar et al. 2020) (**Fig.**

1615   **S20**). First, codon-optimised constructs for *E. coli* expression were synthesized

1616   (Eurofins) using full-length cpEnolase and cpPGAM1A mRNA sequences as

1617   template. Constructs were cloned into a Gateway pDest-CTD-His vector via a

1618   pDONR intermediate and BP /LR clonase (all reagents Thermo Fisher) following the

1619   manufacturer's instructions (Hartley, Temple et al. 2000). To enable optimal

1620   expression in *E. coli*, multiple N-terminal length variants were synthesized from each

1621   gene, with those corresponding to the full gene length minus the predicted N-terminal

1622   signal peptide domain as inferred with SignalP (Almagro Armenteros, Tsirigos et al.

1623 2019). Complete constructs and primers tested are provided in **Supplemental**

1624 **Dataset S6**, sheet 7.

1625

1626 cpEnolase and cpPGAM1A –CTDHis vectors were cloned into Rosetta (DE3) strain

1627 *E. coli* (Novagen) and coselected on ampicillin (100 μg /ml) and chloramphenicol (34

1628 μg /ml). Proteins were induced in overnight cultures at 28°C, purified on a His-Trap

1629 column (GE Healthcare) following the manufacturers' instructions, and eluted in a

1630 buffer consisting of 125 mM NaCl, 250 mM Imidiazol (Sigma) and protease inhibitors.

1631 Eluted proteins were desalted using a Q10/ PD10 column (GE Healthcare) and

1632 quantified using a Bradford. Protein integrity and quantity were assessed routinely

1633 throughout the purification using SDS-PAGE.

1634

1635 Reaction rates were measured on purified 100 μg cpPGAM1A and 100 μg

1636 cpEnolase, as quantified with a nanodrop spectrometer. Rates were measured

1637 separately for glycolytic and gluconeogenic activity. Briefly, to measure glycolytic

1638 reaction rates, both enzymes were combined with 10 units pyruvate kinase and 10

1639 units lactate dehydrogenase (both Sigma-Aldrich) at 25°C, alongside varying

1640 concentrations 9 mM D(-)3-Phosphoglyceric Acid, 25 mM Adenosine ''-Diphosphate,

1641 and 25 mM reduced ß-Nicotinamide Adenine Dinucleotide (NADH). Enzymatic

1642 activity was measured by considering 340 nm colorimetry as a proxy for NADH

1643 consumption following a previously defined protocol (Sigma protocols EC 5.4.2.1)

1644 (Sutherland, Posternak et al. 1949). To measure gluconeogenic reaction rates, a

1645 similar reaction was performed with both enzymes combined with 10 units

1646 phosphoglycerate kinase and 10 units glyceraldehyde-3-phosphate dehydrogenase

1647 (both Sigma-Aldrich), alongside 9 mM phospho-enol-pyruvate, 25 mM Adenosine 5'-

1648 Diphosphate, and 25 mM reduced ß-Nicotinamide Adenine Dinucleotide (NADH).

1649 Enzymatic activity was similarly measured by 340 nm colorimetry. A schematic of the

1650 measured reactions is provided in **Fig. S20**. Complete measured reaction rates over

1651 all technical replicates are provided in **Supplemental Dataset S6**, sheet 8.

1652

1653 **Accession Numbers**

1654

1655 RNAseq data associated with this project is deposited with NCBI BioProject with

1656 project number PRJNA788211.

49

1657

1658 **Materials Distribution Statement**

1659

1660 The author(s) responsible for distribution of materials integral to the findings

1661 presented in this article in accordance with the policy described in the Instructions for

1662 Authors (https://academic.oup.com/plcell/pages/General-Instructions) are: Richard G.

1663 Dorrell (richard.dorrell.algae@gmail.com) and Chris Bowler

1664 (cbowler@bio.ens.psl.eu).

1665

1666 **List of Supporting Files**

1667

1668 **Supplemental Dataset S1. Phylogenetic diversity of Enolase and PGAM**

1669 **sequences from across the tree of life.**

1670

1671 **Supplemental Dataset S2. Transcriptional and localization patterns of cpPGAM**

1672 **and cpEnolase genes in *Phaeodactylum tricornutum*.**

1673

1674 **Supplemental Dataset S3. *Tara* Oceans analysis of diatom plastid glycolysis.**

1675

1676 **Supplemental Dataset S4. Genotyping, growth dynamics and photophysiology**

1677 **in *P. tricornutum* plastid glycolysis mutant lines.**

1678

1679 **Supplemental Dataset S5. Differentially and conditionally expressed genes in**

1680 ***P. tricornutum* plastid glycolysis mutants.**

1681

1682 **Supplemental Dataset S6. Lipid and metabolite profiles of *P. tricornutum***

1683 **plastid glycolysis mutant lines revealed by GC- and LC-mass spectrometry,**

1684 **and measured reaction kinetics of expressed enzymes.**

1685

1686 All remaining supporting data not provided directly in paper supporting tables are

1687 provided in the linked Open Science Foundation Supporting database

1688 https://osf.io/89vm3/ (Dorrell, Novak Vanclova et al. 2022). Project contents are

1689 ordered hierarchically by theme, with an overview of all contents provided on the site

1690 wiki page. A dedicated README file in each project folder explains the data

1691 presented and provides detailed methodology for each analysis.

1692

1693 **Author Contributions**

1694

1695 RGD designed the research, with critical input from YZ, YZ, DC, BB, ARF, JJ, EM

1696 and CB. RGD, YZ, NG, TN, DC, MP, and VG performed the research. RGD, YZ, YL,

1697 DC and MP analysed the data. SA provided new analytical tools for cell growth

1698 measurements, and JJPK and NZ provided new computational tools for meta-

1699 genomic and RNA-seq analysis. RGD wrote the paper, with critical input from YL,

1700 TN, MP, SA, BB, JJPK, JJ, EM and CB. All coauthors read and approved the

1701 manuscript draft prior to final submission.

1702

1703 **Acknowledgments**

1704

1743

References

1745

1746 Abida, H., L. J. Dolch, C. Meï, V. Villanova, M. Conte, M. A. Block, G. Finazzi, O. Bastien, L.
1747 Tirichine, C. Bowler, F. Rébeillé, D. Petroutsos, J. Jouhet and E. Maréchal (2015).
1748 Membrane glycerolipid remodeling triggered by nitrogen and phosphorus starvation in
1749 Phaeodactylum tricornutum. Plant Physiol **167**(1): 118-136.
1750 Ait-Mohamed, O., A. M. G. Novák Vanclová, N. Joli, Y. Liang, X. Zhao, A. Genovesio, L.
1751 Tirichine, C. Bowler and R. G. Dorrell (2020). PhaeoNet: a holistic RNAseq-based portrait
1752 of transcriptional coordination in the model diatom *Phaeodactylum tricornutum*.
1753 Frontiers Plant Sci **11**: 590949.
1754 Allen, A. E., C. L. Dupont, M. Obornik, A. Horak, A. Nunes-Nesi, J. P. McCrow, H. Zheng, D.
1755 A. Johnson, H. Hu, A. R. Fernie and C. Bowler (2011). Evolution and metabolic
1756 significance of the urea cycle in photosynthetic diatoms. Nature **473**(7346): 203-+.
1757 Almagro Armenteros, J. J., K. D. Tsirigos, C. K. Sønderby, T. N. Petersen, O. Winther, S.
1758 Brunak, G. von Heijne and H. Nielsen (2019). SignalP 5.0 improves signal peptide
1759 predictions using deep neural networks. Nat Biotechnol **37**(4): 420-423.
1760 Andriotis, V. M., N. J. Kruger, M. J. Pike and A. M. Smith (2010). Plastidial glycolysis in
1761 developing *Arabidopsis* embryos. New Phytol **185**(3): 649-662.

Anoman, A. D., M. Flores-Tornero, S. Rosa-Telléz, J. Muñoz-Bertomeu, J. Segura and R. Ros (2016). The specific role of plastidial glycolysis in photosynthetic and heterotrophic cells under scrutiny through the study of glyceraldehyde-3-phosphate dehydrogenase. Plant Signal Behav **11**(3): e1128614.

Ashworth, J., S. Turkarslan, M. Harris, M. V. Orellana and N. S. Baliga (2016). Pan-transcriptomic analysis identifies coordinated and orthologous functional modules in the diatoms *Thalassiosira pseudonana* and *Phaeodactylum tricornutum*. Mar Genomics **26**: 21-28.

Bai, Y., T. Cao, O. Dautermann, P. Buschbeck, M. B. Cantrell, Y. Chen, C. D. Lein, X. Shi, M. A. Ware, F. Yang, H. Zhang, L. Zhang, G. Peers, X. Li and M. Lohr (2022). Green diatom mutants reveal an intricate biosynthetic pathway of fucoxanthin. Proc Natl Acad Sci USA **119**(38): e2203708119.

Bailleul, B., N. Berne, O. Murik, D. Petroutsos, J. Prihoda, A. Tanaka, V. Villanova, R. Bligny, S. Flori, D. Falconet, A. Krieger-Liszkay, S. Santabarbara, F. Rappaport, P. Joliot, L. Tirichine, P. G. Falkowski, P. Cardol, C. Bowler and G. Finazzi (2015). Energetic coupling between plastids and mitochondria drives CO2 assimilation in diatoms. Nature **524**(7565): 366-3267.

Behrenfeld, M. J., K. H. Halsey, E. Boss, L. Karp-Boss, A. J. Milligan and G. Peers (2021). Thoughts on the evolution and ecological niche of diatoms. Ecol Monograph **91**(3): e01457.

Broddrick, J. T., N. Du, S. R. Smith, Y. Tsuji, D. Jallet, M. A. Ware, G. Peers, Y. Matsuda, C. L. Dupont, B. G. Mitchell, B. O. Palsson and A. E. Allen (2019). Cross-compartment metabolic coupling enables flexible photoprotective mechanisms in the diatom *Phaeodactylum tricornutum*. New Phytol **222**: 1364-1379.

Bromke, M. A. (2013). Amino Acid biosynthesis pathways in diatoms. Metabolites **3**(2): 294-311.

Buck, J. M., C. Río Bártulos, A. Gruber and P. G. Kroth (2018). Blasticidin-S deaminase, a new selection marker for genetic transformation of the diatom. PeerJ **6**: e5884.

Buck, J. M., J. Sherman, C. R. Bártulos, M. Serif, M. Halder, J. Henkel, A. Falciatore, J. Lavaud, M. Y. Gorbunov, P. G. Kroth, P. G. Falkowski and B. Lepetit (2019). Lhcx proteins provide photoprotection via thermal dissipation of absorbed light in the diatom *Phaeodactylum tricornutum*. Nat Commun **10**(1): 4167.

Buseman, C. M., P. Tamura, A. A. Sparks, E. J. Baughman, S. Maatta, J. Zhao, M. R. Roth, S. W. Esch, J. Shah, T. D. Williams and R. Welti (2006). Wounding stimulates the accumulation of glycerolipids containing oxophytodienoic acid and dinor-oxophytodienoic acid in *Arabidopsis* leaves. Plant Physiol **142**(1): 28-39.

Bustin, S. A., V. Benes, J. A. Garson, J. Hellemans, J. Huggett, M. Kubista, R. Mueller, T. Nolan, M. W. Pfaffl, G. L. Shipley, J. Vandesompele and C. T. Wittwer (2009). The MIQE Guidelines: Minimum Information for publication of Quantitative real-time PCR Experiments. Clin Chem **55**(4): 611-622.

Capella-Gutiérrez, S., J. M. Silla-Martínez and T. Gabaldón (2009). trimAl: a tool for automated alignment trimming in large-scale phylogenetic analyses. Bioinformatics **25**(15): 1972-1973.

Carradec, Q., E. Pelletier, C. Da Silva, A. Alberti, Y. Seeleuthner, R. Blanc-Mathieu, G. Lima-Mendez, F. Rocha, L. Tirichine, K. Labadie, A. Kirilovsky, A. Bertrand, S. Engelen, M. A. Madoui, R. Méheust, J. Poulain, S. Romac, D. J. Richter, G. Yoshikawa, C. Dimier, S. Kandels-Lewis, M. Picheral, S. Searson, O. Jaillon, J. M. Aury, E. Karsenti, M. B. Sullivan, S. Sunagawa, P. Bork, F. Not, P. Hingamp, J. Raes, L. Guidi, H. Ogata, C. de Vargas, D.

Iudicone, C. Bowler, P. Wincker and *Tara* Oceans Coordinators (2018). A global ocean atlas of eukaryotic genes. Nat Commun **9**(1): 373.

Carrera, D., G. M. George, M. Fischer-Stettler, F. Galbier, S. Eicke, E. Truernit, S. Streb and S. C. Zeeman (2021). Distinct plastid fructose bisphosphate aldolases function in photosynthetic and non-photosynthetic metabolism in *Arabidopsis*. J Exp Bot **72**(10): 3739-3755.

Chang, Y. F., J. S. Imam and M. F. Wilkinson (2007). The nonsense-mediated decay RNA surveillance pathway. Annu Rev Biochem **76**: 51-74.

Cruz de Carvalho, M. H., H. X. Sun, C. Bowler and N. H. Chua (2016). Noncoding and coding transcriptome responses of a marine diatom to phosphate fluctuations. New Phytol **210**(2): 497-510.

Delmont, T. O., M. Gaia, D. D. Hinsinger, P. Frémont, C. Vanni, A. Fernandez-Guerra, A. M. Eren, A. Kourlaiev, L. d'Agata, Q. Clayssen, E. Villar, K. Labadie, C. Cruaud, J. Poulain, C. Da Silva, M. Wessner, B. Noel, J.-M. Aury, S. Sunagawa, S. G. Acinas, P. Bork, E. Karsenti, C. Bowler, C. Sardet, L. Stemmann, C. de Vargas, P. Wincker, M. Lescot, M. Babin, G. Gorsky, N. Grimsley, L. Guidi, P. Hingamp, O. Jaillon, S. Kandels, D. Iudicone, H. Ogata, S. Pesant, M. B. Sullivan, F. Not, K.-B. Lee, E. Boss, G. Cochrane, M. Follows, N. Poulton, J. Raes, M. Sieracki, S. Speich and E. Pelletier (2022). Functional repertoire convergence of distantly related eukaryotic plankton lineages abundant in the sunlit ocean. Cell Genom **2**(5): 100123.

Demé, B., C. Cataye, M. A. Block, E. Maréchal and J. Jouhet (2014). Contribution of galactoglycerolipids to the 3-dimensional architecture of thylakoids. FASEB J **28**(8): 3373-3383.

Dolch, L. J. and E. Maréchal (2015). Inventory of fatty acid desaturases in the pennate diatom *Phaeodactylum tricornutum*. Mar Drugs **13**(3): 1317-1339.

Dorrell, R. G., G. Gile, G. McCallum, R. Méheust, E. P. Bapteste, C. M. Klinger, L. Brillet-Guéguen, K. D. Freeman, D. J. Richter and C. Bowler (2017). Chimeric origins of ochrophytes and haptophytes revealed through an ancient plastid proteome. Elife **6,** 23717.

Dorrell, R. G., A. M. G. Novák Vanclová, M. Penot, J. J. Pierella Karlusich, C. Bowler, S. Liu, E. Maréchal, J. Jouhet, B. Bailleul and D. Croteau (2022). Functional physiology of novel diatom chloroplast proteins. Open Science Foundation. https://osf.io/89vm3/.

Emanuelsson, O., S. Brunak, G. von Heijne and H. Nielsen (2007). Locating proteins in the cell using TargetP, SignalP and related tools. Nat Protocol **2**(4): 953-971.

Erdene-Ochir, E., B. K. Shin, B. Kwon, C. Jung and C. H. Pan (2019). Identification and characterisation of the novel endogenous promoter HASP1 and its signal peptide from *Phaeodactylum tricornutum*. Sci Rep **9**(1): 9941.

Falciatore, A., R. Casotti, C. Leblanc, C. Abrescia and C. Bowler (1999). Transformation of Nonselectable Reporter Genes in Marine Diatoms. Mar Biotechnol (NY) **1**(3): 239-251.

Folch, J., M. Lees and G. H. S. Stanley (1957). A simple method for the isolation and purification of total lipids from animal tissues. J Biol Chem **226**(1): 497-509.

Friedlingstein, P., M. W. Jones, M. O'Sullivan, R. M. Andrew, D. C. Bakker, J. Hauck, C. Le Quéré, G. P. Peters, W. Peters and J. Pongratz (2022). Global carbon budget 2021. Earth System Science Data **14**(4): 1917-2005.

Fukasawa, Y., J. Tsuji, S. C. Fu, K. Tomii, P. Horton and K. Imai (2015). MitoFates: improved prediction of mitochondrial targeting sequences and their cleavage sites. Mol Cell Proteom **14**(4): 1113-1126.

Fukayama, H., C. Masumoto, Y. Taniguchi, A. Baba-Kasai, Y. Katoh, H. Ohkawa and M. Miyao (2015). Characterization and expression analyses of two plastidic enolase genes in rice. Biosci Biotechnol Biochem **79**(3): 402-409.

Fuss, J., O. Liegmann, K. Krause and S. A. Rensing (2013). Green Targeting Predictor and Ambiguous Targeting Predictor 2: the pitfalls of plant protein targeting prediction and of transient protein expression in heterologous systems. New Phytol **200**: 1022-1033.

Gachon, C. M. M., S. Heesch, F. C. Kuepper, U. E. M. Achilles-Day, D. Brennan, C. N. Campbell, A. Clarke, R. G. Dorrell, J. Field, S. Gontarek, C. R. Menendez, R. J. Saxon, A. Veszelovszki, M. D. Guiry, K. Gharbi, M. Blaxter and J. G. Day (2013). The CCAP KnowledgeBase: linking protistan and cyanobacterial biological resources with taxonomic and molecular data. Systemat Biodiv **11**(4): 407-413.

Gilbertson, R., E. Langan and T. Mock (2022). Diatoms and their microbiomes in complex and changing polar oceans. Front Microbiol **13**: 786764.

Gorbunov, M. Y., E. Shirsin, E. Nikonova, V. V. Fadeev and P. G. Falkowski (2020). A multi-spectral fluorescence induction and relaxation (FIRe) technique for physiological and taxonomic analysis of phytoplankton communities. Mar Ecol Prog Series **644**: 1-13.

Grigoriev, I. V., R. D. Hayes, S. Calhoun, B. Kamel, A. Wang, S. Ahrendt, S. Dusheyko, R. Nikitin, S. J. Mondo, A. Salamov, I. Shabalov and A. Kuo (2021). PhycoCosm, a comparative algal genomics resource. Nucleic Acids Res **49**(D1): D1004-D1011.

Gruber, A., G. Rocap, P. G. Kroth, E. V. Armbrust and T. Mock (2015). Plastid proteome prediction for diatoms and other algae with secondary plastids of the red lineage. Plant J **81**(3): 519-528.

Gschloessl, B., Y. Guermeur and J. M. Cock (2008). HECTAR: a method to predict subcellular targeting in heterokonts. BMC Bioinformatics **9**: 393.

Hannaert, V., M.A. Albert, D.J. Ridgen, M.T. da Silva Giotto, O. Thiemann, R.C. Garratt, J. Van Roy, F. R. Opperdoes and P.A.M. Michels. Kinetic characterization, structure modelling studies and crystallization of *Trypanosoma brucei* enolase. Eur J Biochem **270**, 3205-3213.

Hartley, J. L., G. F. Temple and M. A. Brasch (2000). DNA cloning using in vitro site-specific recombination. Genome Res **10**(11): 1788-1795.

Hippmann, A. A., N. Schuback, K.-M. Moon, J. P. McCrow, A. E. Allen, L. F. Foster, B. R. Green and M. T. Maldonado (2022). Proteomic analysis of metabolic pathways supports chloroplast–mitochondria cross-talk in a Cu-limited diatom. Plant Direct **6**(1): e376.

Horton, P., K. J. Park, T. Obayashi, N. Fujita, H. Harada, C. J. Adams-Collier and K. Nakai (2007). WoLF PSORT: protein localization predictor. Nucl Acids Res **35**: W585-W587.

Huang, A., L. Liu, C. Yang and G. Wang (2015). *Phaeodactylum tricornutum* photorespiration takes part in glycerol metabolism and is important for nitrogen-limited response. Biotechnol Biofuels **8**(1): 1-16.

Huang, T., Y. Pan, E. Maréchal and H. Hu (2024). Proteomes reveal the lipid metabolic network in the complex plastid of *Phaeodactylum tricornutum*. Plant J **117**: 385-403.

Initiative, O. T. P. T. (2019). One thousand plant transcriptomes and the phylogenomics of green plants. Nature **574**(7780): 679-685.

Jassby, A. D. and T. Platt (1976). Mathematical formulation of the relationship between photosynthesis and light for phytoplankton. Limnol Oceanograph **21**(4): 540-547.

Jiang, Y., T. Cao, Y. Yang, H. Zhang, J. Zhang and X. Li (2023). A chlorophyll c synthase widely co-opted across phytoplankton. Science **382**(6666): 92-98.

Joli, N., L. Concia, K. Mocaer, J. Guterman, J. Laude, S. Guerin, T. Sciandra, F. Bruyant, O. Ait-Mohamed, M. Beguin, M.-H. Forget, C. Bourbousse, T. Lacour, B. Bailleul, C. Nef, M. Savoie, J.-E. Tremblay, D. A. Campbell, J. Lavaud, Y. Schwab, M. Babin and C. Bowler

(2024). Hypometabolism to survive the long polar night and subsequent successful return to light in the diatom *Fragilariopsis cylindrus*. New Phytol **241**(2193-2208).

Jones, P., D. Binns, H. Y. Chang, M. Fraser, W. Li, C. McAnulla, H. McWilliam, J. Maslen, A. Mitchell, G. Nuka, S. Pesseat, A. F. Quinn, A. Sangrador-Vegas, M. Scheremetjew, S. Y. Yong, R. Lopez and S. Hunter (2014). InterProScan 5: genome-scale protein function classification. Bioinformatics **30**(9): 1236-1240.

Jouhet, J., J. Lupette, O. Clerc, L. Magneschi, M. Bedhomme, S. Collin, S. Roy, E. Maréchal and F. Rébeillé (2017). LC-MS/MS versus TLC plus GC methods: Consistency of glycerolipid and fatty acid profiles in microalgae and higher plant cells and effect of a nitrogen starvation. PLoS One **12**(8): e0182423.

Jouhet, J., E. Maréchal, R. Bligny, J. Joyard and M. A. Block (2003). Transient increase of phosphatidylcholine in plant cells in response to phosphate deprivation. FEBS Lett**544**(1): 63-68.

Kassambara, A. and F. Mundt (2017). Package 'factoextra'. Extract and visualize the results of multivariate data analyses **76**(2).

Katoh, K., J. Rozewicki and K. D. Yamada (2017). MAFFT online service: multiple sequence alignment, interactive sequence choice and visualization. Brief Bioinform **20**: 1160-1166.

Kazamia, E., R. Sutak, J. Paz-Yepes, R. G. Dorrell, F. R. J. Vieira, J. Mach, J. Morrissey, S. Leon, F. Lam, E. Pelletier, J. M. Camadro, C. Bowler and E. Lesuisse (2018). Endocytosis-mediated siderophore uptake as a strategy for Fe acquisition in diatoms. Sci Adv **4**(5): eaar4536.

Kearse, M., R. Moir, A. Wilson, S. Stones-Havas, M. Cheung, S. Sturrock, S. Buxton, A. Cooper, S. Markowitz, C. Duran, T. Thierer, B. Ashton, P. Meintjes and A. Drummond (2012). Geneious Basic: An integrated and extendable desktop software platform for the organization and analysis of sequence data. Bioinform **28**(12): 1647-1649.

Keeling, P. J., F. Burki, H. M. Wilcox, B. Allam, E. E. Allen, L. A. Amaral-Zettler, E. V. Armbrust, J. M. Archibald, A. K. Bharti, C. J. Bell, B. Beszteri, K. D. Bidle, C. T. Cameron, L. Campbell, D. A. Caron, R. A. Cattolico, J. L. Collier, K. Coyne, S. K. Davy, P. Deschamps, S. T. Dyhrman, B. Edvardsen, R. D. Gates, C. J. Gobler, S. J. Greenwood, S. M. Guida, J. L. Jacobi, K. S. Jakobsen, E. R. James, B. Jenkins, U. John, M. D. Johnson, A. R. Juhl, A. Kamp, L. A. Katz, R. Kiene, A. Kudryavtsev, B. S. Leander, S. Lin, C. Lovejoy, D. Lynn, A. Marchetti, G. McManus, A. M. Nedelcu, S. Menden-Deuer, C. Miceli, T. Mock, M. Montresor, M. A. Moran, S. Murray, G. Nadathur, S. Nagai, P. B. Ngam, B. Palenik, J. Pawlowski, G. Petroni, G. Piganeau, M. C. Posewitz, K. Rengefors, G. Romano, M. E. Rumpho, T. Rynearson, K. B. Schilling, D. C. Schroeder, A. G. Simpson, C. H. Slamovits, D. R. Smith, G. J. Smith, S. R. Smith, H. M. Sosik, P. Stief, E. Theriot, S. N. Twary, P. E. Umale, D. Vaulot, B. Wawrik, G. L. Wheeler, W. H. Wilson, Y. Xu, A. Zingone and A. Z. Worden (2014). The Marine Microbial Eukaryote Transcriptome Sequencing Project (MMETSP): illuminating the functional diversity of eukaryotic life in the oceans through transcriptome sequencing. PLoS Biol **12**(6): e1001889.

Kopka, J., N. Schauer, S. Krueger, C. Birkemeyer, B. Usadel, E. Bergmüller, P. Dörmann, W. Weckwerth, Y. Gibon, M. Stitt, L. Willmitzer, A. R. Fernie and D. Steinhauser (2005). GMD@CSB.DB: the Golm Metabolome Database. Bioinformatics **21**(8): 1635-1638.

Krebs, H. A. (1963). Renal gluconeogenesis. Adv Enzyme Regul **1**: 385-400.

Kroth, P. G., A. Chiovitti, A. Gruber, V. Martin-Jezequel, T. Mock, M. S. Parker, M. S. Stanley, A. Kaplan, L. Caron, T. Weber, U. Maheswari, E. V. Armbrust and C. Bowler (2008). A model for carbohydrate metabolism in the diatom *Phaeodactylum tricornutum* deduced from comparative whole genome analysis. PLoS One **3**(1): e1426.

Lataretu, M. and M. Hölzer (2020). RNAflow: an effective and simple RNA-Seq differential gene expression pipeline using Nextflow. Genes (Basel) **11**(12).

Lepetit, B., D. A. Campbell, J. Lavaud, C. Büchel, R. Goss and B. Bailleul (2022). Photosynthetic Light Reactions in diatoms. II. The dynamic regulation of the various light reactions. The Molecular Life of Diatoms. A. Falciatore and T. Mock. Cham, Springer International Publishing**:** 423-464.

Levering, J., J. Broddrick, C. L. Dupont, G. Peers, K. Beeri, J. Mayers, A. A. Gallina, A. E. Allen, B. O. Palsson and K. Zengler (2016). Genome-scale model reveals metabolic basis of biomass partitioning in a model diatom. Plos One **11**(5), 0155038.

Lisec, J., N. Schauer, J. Kopka, L. Willmitzer and A. R. Fernie (2006). Gas chromatography mass spectrometry–based metabolite profiling in plants. Nat Protocol **1**(1): 387-396.

Liu, S., M. Storti, C. Bowler, G. Finazzi and R. G. Dorrell (2022). A metabolic, phylogenomic and environmental atlas of diatom plastid transporters from the model species *Phaeodactylum*. Front Plant Sci **13**, 950467.

Liu, S., Z. Wang, R. Zhu, F. Wang, Y. Cheng and Y. Liu (2021). Three Differential Expression Analysis Methods for RNA Sequencing: limma, EdgeR, DESeq2. J Vis Exp(175).

Lovejoy, C., W. F. Vincent, S. Bonilla, S. Roy, M. J. Martineau, R. Terrado, M. Potvin, R. Massana and C. Pedros-Alio (2007). Distribution, phylogeny, and growth of cold-adapted picoprasinophytes in Arctic seas. J Phycol **43**(1): 78-89.

Luedemann, A., L. von Malotky, A. Erban and J. Kopka (2012). TagFinder: preprocessing software for the fingerprinting and the profiling of gas chromatography-mass spectrometry based metabolome analyses. Methods Mol Biol **860**: 255-286.

Malviya, S., E. Scalco, S. Audic, F. Vincent, A. Veluchamy, J. Poulain, P. Wincker, D. Iudicone, C. de Vargas, L. Bittner, A. Zingone and C. Bowler (2016). Insights into global diatom distribution and diversity in the world's ocean. Proc Natl Acad Sci USA **113**(11): 1516-1525.

Maréchal, E. and J. Lupette (2020). Relationship between acyl-lipid and sterol metabolisms in diatoms. Biochimie **169**: 3-11.

McCarthy, J. K., S. R. Smith, J. P. McCrow, M. Tan, H. Zheng, K. Beeri, R. Roth, C. Lichtle, U. Goodenough, C. P. Bowler, C. L. Dupont and A. E. Allen (2017). Nitrate Reductase knockout uncouples nitrate transport from nitrate assimilation and drives repartitioning of carbon flux in a model pennate diatom. Plant Cell **29**(8): 2047-2070.

Miller, M. A., T. Schwartz, B. E. Pickett, S. He, E. B. Klem, R. H. Scheuermann, M. Passarotti, S. Kaufman and M. A. O'Leary (2015). A RESTful API for access to phylogenetic tools via the CIPRES Science Gateway. Evol Bioinform Online **11**: 43-48.

Mistry, J., S. Chuguransky, L. Williams, M. Qureshi, G. A. Salazar, E. L. L. Sonnhammer, S. C. E. Tosatto, L. Paladin, S. Raj, L. J. Richardson, R. D. Finn and A. Bateman (2020). PFAM: the protein families database in 2021. Nucleic Acids Res.

Moog, D., A. Nozawa, Y. Tozawa and R. Kamikawa (2020). Substrate specificity of plastid phosphate transporters in a non-photosynthetic diatom and its implication in evolution of red alga-derived complex plastids. Sci Rep **10**(1): 1167.

Moog, D., S. A. Rensing, J. M. Archibald, U. G. Maier and K. K. Ullrich (2015). Localization and evolution of putative triose phosphate translocators in the diatom *Phaeodactylum tricornutum*. Genom Biol Evol **7**(11): 2955-2969.

Murik, O., L. Tirichine, J. Prihoda, Y. Thomas, W. L. Araújo, A. E. Allen, A. R. Fernie and C. Bowler (2019). Downregulation of mitochondrial alternative oxidase affects chloroplast function, redox status and stress response in a marine diatom. New Phytol **221**(3): 1303-1316.

Nash, E. A., A. C. Barbrook, R. K. Edwards-Stuart, K. Bernhardt, C. J. Howe and R. E. R. Nisbet (2007). Organization of the mitochondrial genome in the dinoflagellate Amphidinium carterae. Mol Biol Evol **24**(7): 1528-1536.

Nawaly, H., H. Matsui, Y. Tsuji, K. Iwayama, H. Ohashi, K. Nakajima and Y. Matsuda (2023). Multiple plasma membrane SLC4s contribute to external HCO3– acquisition during CO2 starvation in the marine diatom *Phaeodactylum tricornutum*. J Exp Bot **74**(1): 296-307.

Nonoyama, T., E. Kazamia, H. Nawaly, X. Gao, Y. Tsuji, Y. Matsuda, C. Bowler, T. Tanaka and R. G. Dorrell (2019). Metabolic innovations underpinning the origin and diversification of the diatom chloroplast. Biomolecules **9**(8), 484.

Nymark, M., A. K. Sharma, T. Sparstad, A. M. Bones and P. Winge (2016). A CRISPR/Cas9 system adapted for gene editing in marine algae. Sci Rep **6**: 24951.

Pesant, S., F. Not, M. Picheral, S. Kandels-Lewis, N. Le Bescot, G. Gorsky, D. Iudicone, E. Karsenti, S. Speich, R. Trouble, C. Dimier, S. Searson and C. Tara Oceans (2015). Open science resources for the discovery and analysis of Tara Oceans data. Sci Data **2**.

Pierella Karlusich, J. J., C. Nef, C. Bowler and R. Dorrell (2023). Modèles biogéographiques et génomes des photoautotrophes aquatiques**:** 45-82.

Popko, J., C. Herrfurth, K. Feussner, T. Ischebeck, T. Iven, R. Haslam, M. Hamilton, O. Sayanova, J. Napier, I. Khozin-Goldberg and I. Feussner (2016). Metabolome analysis reveals betaine lipids as major source for triglyceride formation, and the accumulation of sedoheptulose during nitrogen-starvation of *Phaeodactylum tricornutum*. PLoS One **11**(10): e0164673.

Prabhakar, V., T. Löttgert, T. Gigolashvili, K. Bell, U. I. Flügge and R. E. Häusler (2009). Molecular and functional characterization of the plastid-localized phosphoenolpyruvate enolase (ENO1) from *Arabidopsis thaliana*. FEBS Lett **583**(6): 983-991.

Raines, C. A. (2003). The Calvin Cycle revisited. Photosynth Res **75**(1): 1-10.

Rainteau, D., L. Humbert, E. Delage, C. Vergnolle, C. Cantrel, M.-A. Maubert, S. Lanfranchi, R. Maldiney, S. Collin, C. Wolf, A. Zachowski and E. Ruelland (2012). Acyl chains of phospholipase D transphosphatidylation products in *Arabidopsis* cells: a study using multiple reaction monitoring mass spectrometry. PLoS One **7**(7): e41985.

Rastogi, A., U. Maheswari, R. G. Dorrell, F. R. J. Vieira, F. Maumus, A. Kustka, J. McCarthy, A. E. Allen, P. Kersey, C. Bowler and L. Tirichine (2018). Integrative analysis of large scale transcriptome data draws a comprehensive landscape of *Phaeodactylum tricornutum* genome and evolutionary origin of diatoms. Sci Rep **8**(1): 4834.

Rastogi, A., O. Murik, C. Bowler and L. Tirichine (2016). PhytoCRISP-Ex: a web-based and stand-alone application to find specific target sequences for CRISPR/CAS editing. BMC Bioinform **17**(1): 261.

Rastogi, A., F. R. J. Vieira, A. F. Deton-Cabanillas, A. Veluchamy, C. Cantrel, G. Wang, P. Vanormelingen, C. Bowler, G. Piganeau, H. Hu and L. Tirichine (2020). A genomics approach reveals the global genetic polymorphism, structure, and functional diversity of ten accessions of the marine model diatom *Phaeodactylum tricornutum*. ISME J **14**(2): 347-363.

Reinoso, R. F., B. A. Telfer and M. Rowland (1997). Tissue water content in rats measured by desiccation. J Pharmacol Toxicol Methods **38**(2): 87-92.

Royo-Llonch, M., P. Sánchez, C. Ruiz-González, G. Salazar, C. Pedrós-Alió, K. Labadie, L. Paoli, C. Tara Oceans, S. Chaffron, D. Eveillard, E. Karsenti, S. Sunagawa, P. Wincker, L. Karp-Boss, C. Bowler and S. G. Acinas (2021). Compendium of 530 metagenome-assembled bacterial and archaeal genomes from the polar Arctic Ocean. Nat Microbiol **2021**: 1561-1574.

Rider, CC. and C.B. Taylor, Enolase isoenzymes in rat tissues: electrophoretic, chromatographic, immunological and kinetic properties. Biochim Biophys Acta **365**(1): 285-300.

Río Bártulos, C., M. B. Rogers, T. A. Williams, E. Gentekaki, H. Brinkmann, R. Cerff, M. F. Liaud, A. B. Hehl, N. R. Yarlett, A. Gruber, P. G. Kroth and M. van der Giezen (2018). Mitochondrial Glycolysis in a Major Lineage of Eukaryotes. Genom Biol Evol **10**(9): 2310-2325.

Sachse, M., S. Sturm, A. Gruber and P. Kroth (2013). Identification and evaluation of endogenous reference genes for steady state transcript quantification by qPCR in the diatom *Phaeodactylum tricornutum* with constitutive expression independent from time and light. Endocytobiosis Cell Res **24**: 7.

Scialdone, A., S. T. Mugford, D. Feike, A. Skeffington, P. Borrill, A. Graf, A. M. Smith and M. Howard (2013). Arabidopsis plants perform arithmetic division to prevent starvation at night. eLife **2**: e00669.

Scrutton, M. C. and M. F. Utter (1968). The Regulation of Glycolysis and Gluconeogenesis in Animal Tissues. Annu Rev Biochem **37**(1): 249-302.

Serôdio, J. and J. Lavaud (2011). A model for describing the light response of the nonphotochemical quenching of chlorophyll fluorescence. Photosynth Res **108**(1): 61-76.

Shtaida, N., I. Khozin-Goldberg and S. Boussiba (2015). The role of pyruvate hub enzymes in supplying carbon precursors for fatty acid synthesis in photosynthetic microalgae. Photosynth Res **125**(3): 407-422.

Siegel, P., K. G. Baker, E. Low-Décarie and R. J. Geider (2020). High predictability of direct competition between marine diatoms under different temperatures and nutrient states. Ecol Evol **10**(14): 7276-7290.

Smith, S. R., R. M. Abbriano and M. Hildebrand (2012). Comparative analysis of diatom genomes reveals substantial differences in the organization of carbon partitioning pathways. Algal Res **1**(1): 2-16.

Smith, S. R., C. L. Dupont, J. K. McCarthy, J. T. Broddrick, M. Oborník, A. Horák, Z. Füssy, J. Cihlář, S. Kleessen, H. Zheng, J. P. McCrow, K. K. Hixson, W. L. Araújo, A. Nunes-Nesi, A. Fernie, Z. Nikoloski, B. O. Palsson and A. E. Allen (2019). Evolution and regulation of nitrogen flux through compartmentalized metabolic networks in a marine diatom. Nat Commun **10**(1): 4552.

Smith, S. R., J. T. Gillard, A. B. Kustka, J. P. McCrow, J. H. Badger, H. Zheng, A. M. New, C. L. Dupont, T. Obata, A. R. Fernie and A. E. Allen (2016). Transcriptional orchestration of the global cellular response of a model pennate diatom to diel light cycling under iron limitation. PLoS Genet **12**(12): e1006490.

Spitzer, M., J. Wildenhain, J. Rappsilber and M. Tyers (2014). BoxPlotR: a web tool for generation of box plots. Nat Methods **11**(2): 121-122.

Stamatakis, A. (2014). RAxML version 8: a tool for phylogenetic analysis and post-analysis of large phylogenies. Bioinformatics **30**(9): 1312-1313.

Strassert, J. F. H., I. Irisarri, T. A. Williams and F. Burki (2021). A molecular timescale for eukaryote evolution with implications for the origin of red algal-derived plastids. Nat Commun **12**(1): 1879.

Sutherland, E. W., T. Posternak and C. F. Cori (1949). Mechanism of the phosphoglyceric mutase reaction. J Biol Chem **181**(1): 153-159.

Tanaka, R. and A. Tanaka (2007). Tetrapyrrole biosynthesis in higher plants. Annu Rev Plant Biol **58**: 321-346.

Tardif, M., A. Atteia, M. Specht, G. Cogne, N. Rolland, S. Brugière, M. Hippler, M. Ferro, C. Bruley, G. Peltier, O. Vallon and L. Cournac (2012). PredAlgo: a new subcellular localization prediction tool dedicated to green algae. Mol Biol Evol **29**(12): 3625-3639.

Troncoso-Ponce, M. A., J. Rivoal, S. Dorion, R. Sánchez, M. Venegas-Calerón, A. J. Moreno-Pérez, S. Baud, R. Garcés and E. Martínez-Force (2018). Molecular and biochemical characterization of the sunflower (Helianthus annuus L.) cytosolic and plastidial enolases in relation to seed development. Plant Sci **272**: 117-130.

Uwizeye, C., J. Decelle, P. Jouneau, B. Gallet, J. Keck, C. Moriscot, F. Chevalier, N. Schieber, R. Templin, G. Curien, Y. Schwab, G. Schoehn, S. C. Zeeman, D. Falconet and G. Finazzi (2020). Morphological bases of phytoplankton energy management and physiological responses unveiled by 3D subcellular imaging. Nat Commun **12**: 1à49.

Worden, A. Z., J. H. Lee, T. Mock, P. Rouze, M. P. Simmons, A. L. Aerts, A. E. Allen, M. L. Cuvelier, E. Derelle, M. V. Everett, E. Foulon, J. Grimwood, H. Gundlach, B. Henrissat, C. Napoli, S. M. McDonald, M. S. Parker, S. Rombauts, A. Salamov, P. Von Dassow, J. H. Badger, P. M. Coutinho, E. Demir, I. Dubchak, C. Gentemann, W. Eikrem, J. E. Gready, U. John, W. Lanier, E. A. Lindquist, S. Lucas, K. F. X. Mayer, H. Moreau, F. Not, R. Otillar, O. Panaud, J. Pangilinan, I. Paulsen, B. Piegu, A. Poliakov, S. Robbens, J. Schmutz, E. Toulza, T. Wyss, A. Zelensky, K. Zhou, E. V. Armbrust, D. Bhattacharya, U. W. Goodenough, Y. Van de Peer and I. V. Grigoriev (2009). Green evolution and dynamic adaptations revealed by genomes of the marine picoeukaryotes *Micromonas*. Science **324**(5924): 268-272.

Yang, L., Z. Wang, A. Zhang, R. Bhawal, C. Li, S. Zhang, L. Cheng and J. Hua (2022). Reduction of the canonical function of a glycolytic enzyme enolase triggers immune responses that further affect metabolism and growth in *Arabidopsis*. Plant Cell **34**(5): 1745-1767.

Ye, J., G. Coulouris, I. Zaretskaya, I. Cutcutache, S. Rozen and T. L. Madden (2012). Primer-BLAST: a tool to design target-specific primers for polymerase chain reaction. BMC Bioinform **13**: 134.

Yin, W. and H. Hu (2023). CRISPR/Cas9-Mediated Genome Editing via Homologous Recombination in a Centric Diatom Chaetoceros muelleri. ACS Synth Biol **12**(4): 1287-1296.

Young, E. F. and J. T. Holt (2007). Prediction and analysis of long-term variability of temperature and salinity in the Irish Sea. J Geophys Res **112**(C1).

Yu, G., K. Nakajima, A. Gruber, C. Rio Bartulos, A. F. Schober, B. Lepetit, E. Yohannes, Y. Matsuda and P. G. Kroth (2022). Mitochondrial phosphoenolpyruvate carboxylase contributes to carbon fixation in the diatom *Phaeodactylum tricornutum* at low inorganic carbon concentrations. New Phytol **235**: 1379-1393.

Zhang, Y., A. Sampathkumar, S. M.-L. Kerber, C. Swart, C. Hille, K. Seerangan, A. Graf, L. Sweetlove and A. R. Fernie (2020). A moonlighting role for enzymes of glycolysis in the co-localization of mitochondria and chloroplasts. Nat Commun **11**(1): 4509.

Zhao, Z. and S. M. Assmann (2011). The glycolytic enzyme, phosphoglycerate mutase, has critical roles in stomatal movement, vegetative growth, and pollen production in *Arabidopsis thaliana*. J Exp Bot **62**(14): 5179-5189.

Zheng, Y. T., A. H. Quinn and G. Sriram (2013). Experimental evidence and isotopomer analysis of mixotrophic glucose metabolism in the marine diatom *Phaeodactylum tricornutum*. Microbial Cell Factories **12**: 16.

Zhu, B.-H., H.-P. Shi, G.-P. Yang, N.-N. Lv, M. Yang and K.-H. Pan (2016). Silencing UDP-glucose pyrophosphorylase gene in *Phaeodactylum tricornutum* affects carbon allocation. New Biotechnol **33**(1): 237-244.

2149 Zulu, N. N., K. Zienkiewicz, K. Vollheyde and I. Feussner (2018). Current trends to
2150 comprehend lipid metabolism in diatoms. Progr Lipid Res **70**: 1-16.
2151

2152 **Figures**

2153

2154 **Fig. 1. Metabolic context and evolution of the lower half of diatom plastid**

2155 **glycolysis-gluconeogenesis. A:** schematic comparison of diatom and plant core

2156 carbon metabolism, highlighting the localization and functions of two enzymes in the

2157 lower half of glycolysis-gluconeogenesis (phospho-glycerate mutase, and enolase)

2158 whose localization to the chloroplast can connect endogenous enzymes in the Calvin

2159 cycle and pyruvate hub to create a complete glycolytic-gluconeogenic-gluconeogenic

2160 pathway. Abbreviations: GA3P- glyceraldehyde-3-phosphate; 1,3-PGA and 2,3-PGA-

2161 1,3 and 2,3 bis-phosphoglycerate; Glu-6-P- glucose-6-phosphate; PEP- phospho-

2162 enol-pyruvate; RuBP- ribulose *bis*-phosphate; PGAM- phospho-glycerate mutase;

2163 cER- chloroplast: ndoplasmic reticulum. **B, C:** consensus MrBayes topologies

2164 realised with three substitution matrices (GTR, Jones, WAG) of a 163 taxa x 413 aa

2165 alignment of organelle-targeted enolase and 105 taxa x 220 aa alignment of selected

2166 organelle-targeted PGAM1 enzymes from diatoms and their closest relatives,

2167 identifying recent duplications and recruitments of respiratory glycolytic-

2168 gluconeogenic enzymes from the mitochondria to plastid in diatoms and their closest

2169 relatives. Branch lines correspond to the frequency with which a given branching

2170 relationship was recovered, with thick branches identified by all three substitution

2171 matrices.

2172

2173 **Fig. 2. Localisation and expression of *Phaeodactylum tricornutum* cpEnolase**

2174 **and cpPGAM1A. A:** individual channel and overlay images of GFP-tagged full-length

2175 cpEnolase (Phatr3_J41515) and cpPGAM1A (Phatr3_J17086) constructs (green),

2176 chlorophyll (red) and bright-field images of transformant *P. tricornutum* lines. Scale

2177 bar: 10 µm. **B:** quantitative RT-PCR (qRT-PCR) of cpEnolase and cpPGAM1A

2178 expression in mid-exponential phase cells harvested at the mid-point of a 19C 12h

2179 light: 12h dark cycle (19LD); at the same timepoint but under 24h continuous light

2180 (19CL); and under 8C and continuous light (8CL). Relative expression levels were

2181 normalised against two housekeeping genes (RPS, RNA polymerase subunit 1; TBP,

2182 Tata binding protein) that show invariant expression in response to light cycles in

2183   *Phaeodactylum* per (Sachse, Sturm et al. 2013). *: significantly different expression

2184   levels, one-way ANOVA, P < 0.05; **, the same, P < 0.001.

2185

2186   **Fig. 3. Environmental distributions of diatom plastidial lower half glycolysis-**

2187   **gluconeogenesis meta-genes.** Total transcriptome **(A)** and genome **(B)** relative

2188   abundances, sampled from all (0.8-2000μm) size fractions and surface layer **(i,iii)** or

2189   DCM **(ii,iv)** stations for *Tara* Oceans meta-genes phylogenetically resolved to diatom

2190   cpEnolase **(i,ii)** and cpPGAM1 **(iii,iv).** These data provide a global overview of *Tara*

2191   Oceans meta-gene abundances, in complement to data from individual size fractions

2192   shown in **Fig. S9.** These data demonstrate higher meta-transcript abundance without

2193   commensurate increases in meta-gene abundance at high northern and southern

2194   latitudes.

2195

2196   **Fig. 4. Growth phenotypes of cpEnolase and cpPGAM1A CRISPR-Cas9**

2197   **knockout mutant and zeocin-resistant empty vector control *P. tricornutum***

2198   **lines. A:** exemplar growth curves from single experiments realised for *P. tricornutum*

2199   lines in 50 μE m^{-2} s^{-1} illumination, non-shaken cultures and replete ESAW media,

2200   under three conditions- (i) 19°C and 12h light: 12h dark Circadian cycles (« 19C

2201   LD »); (ii) 19°C and 24h continuous light (« 19C CL »); and (iii) 8°C and 24h

2202   continuous light (« 8C CL »). Hashed black lines show the approximative

2203   concentrations (between 5 x10^4 and 4 x 10^6 cells ml^{-1}) over which growth rates were

2204   calculated). **B:** mean relative log phase growth rates of each genotype under each

2205   condition, measured through a minimum of three biological replicates and two

2206   technical repetitions (six measurements per line, minimum 24 measurements per

2207   genotype), over five time-points with linear (r^2 > 0.95 relationship between log cell

2208   density and time). Asterisks indicate significant differences as inferred by one-way

2209   ANOVA. An alternative version of this figure showing absolute growth rates of

2210   individual cell lines is provided in **Fig. S14.**

2211

2212   **Fig. 5. Changes in plastid and mitochondrial metabolic architecture inferred**

2213   **from gene expression analyses. A:** predicted consensus localizations (either:

2214   chloroplast, or non-chloroplast) from ASAFind (Gruber, Rocap et al. 2015) and

2215   HECTAR (Gschloessl, Guermeur et al. 2008) of all genes inferred (P < 0.05, fold-

2216   change expression >2) to be up- or down-regulated in both cpEnolase and

2217 cpPGAM1A knockout compared to control lines under 19C LD, 19C CL and 8C CL.

2218 Significantly enriched localizations (two-tailed chi-squared test) are asterisked. **B:**

2219 relative mRNA abundances of eleven genes encoding exemplar chloroplast- and

2220 mitochondria-targeted proteins, verified by qRT-PCR. Genes differentially expressed

2221 (two-tailed *t*-test, P < 0.05) in each condition are asterisked.

2222

2223 **Fig. 6. Volcano plots of differentially accumulated metabolites assessed by GC-**

2224 **MS.** Scatterplots of the $\log_2$ accumulation ratios and $-\log_{10}$ P-values of difference in

2225 the mass, ribitol and quality-control-normalised abundances of 39 sugars and amino

2226 acid metabolites in cpEnolase and cpPGAM1A knockout compared to empty vector

2227 control lines, measured by GC-MS in all three experimental conditions tested.

2228 Metabolites that show a differential accumulation in each plot (P < 10^{-05}) are labelled,

2229 with metabolites that show a differential accumulation in both knockout lines in each

2230 condition shown in black text, and five metabolites that are uniquely over-

2231 accumulated in cpEnolase knockout lines under all three conditions shown in dark

2232 red text.

2233

2234 **Fig. 7. LC-MS lipid distributions in glycolysis-gluconeogenesis mutant lines. A:**

2235 scatterplots of relative proportions of MGDG and TAG in total lipid LC-MS samples in

2236 cpEnolase and cpPGAM1A knockout lines and empty vector controls under each

2237 growth condition, showing increased MGDG: TAG in glycolysis knockout lines under

2238 19C, and the inverse relationship in cpEnolase knockout lines only under 8C. **B:**

2239 violin plots of relative abundances of three further lipid categories inferred to

2240 differentially accumulate in glycolysis knockout lines under different growth

2241 conditions. Significant differences between knockout and control lines (one-way

2242 ANOVA) are asterisked.

2243

2244 **Fig. 8. Proposed activities of *P. tricornutum* plastid lower glycolysis-**

2245 **gluconeogenesis.** Schematic diagram showing potential inferred roles of lower half

2246 diatom plastid glycolysis-gluconeogenesis in each environmental condition tested.

2247 The measured V_{max} of purified cpEnolase and cPGAM1A supplemented with 3-PGA

2248 (glycolytic direction) or PEP (gluconeogenic direction) are provided for 9mM

2249 substrate in each case**.**

2250

Fig. S1. Distribution of lower plastid glycolysis-glucneogenesis across photosynthetic eukaryotes. A: Occurrence of plastid-targeted enolase and PGAM enzymes across 1,673 plant and algal genomes and transcriptomes, inferred using reciprocal BLAST best hit of *P. tricornutum* query enzymes as per **Fig. 1B** and **1C,** PFAM domain annotations, and in silico targeting predictions with TargetP and PredAlgo (primary chloroplast bearing lineages) and HECTAR and ASAFind (secondary lineages). **B:** scatterplots of collection site latitude for (**i**) diatoms, (ii) other stramenopiles, **(iii)** cryptomonads and haptophytes and **(iv)** green algae with detectable enolase and PGAM enzymes, divided by presence of inferred plastid-targeted isoforms. Notably, diatoms lacking both plastid-targeted glycolysis enzymes do not occur outside of low and intermediate latitudes (50°N in the northern and 60°S in the southern hemisphere) compared to other groups, which show no significant association between plastid glycolysis and latitude. The data in this figure were subselected for the phylogenies shown in **Fig. 1** and support the latitudinal correlations revealed by Tara analysis of **Fig. 3.**

Fig. S2. Consensus topology of a 380 taxa x 413 aa alignment of Enolase sequences. Sequences represent a sample of all organelle-targeted isoforms from cryptomonads, haptophytes and stramenopiles and representatives from a densely-sampled dataset of 151 taxonomic groups across the tree of life (Dorrell et al., 2021). The tree topology shown is the consensus of the best-scoring rAxML trees identified using three substitution matrices: GTR, JTT, and WAG. Branch thickness corresponds to frequency of consensus tree topology recovery in individual trees; branches are coloured by taxonomic affiliation; and tips (cryptomonads, haptophytes and stramenopiles only) by predicted *in silico* localization. Individual clades (considering both taxonomic origins and inferred localization) of organelle-targeted enolase isoform are labelled with coloured brackets. This figure extends on the topology shown in **Fig. 1B**.

Fig. S3. Consensus topology of a 220 aa x 560 taxa alignment of PGAM isoform 1 sequences. Data are shown as per **Fig. S1**, extending on the topology of **Fig. 1C.**

Fig. S4. Consensus phylogeny of a 235 aa x 66 taxa alignment of PGAM isoform 2 sequences. Data are shown as per **Fig. S1,** forming a complement to the PGAM1 topologies shown in **Fig. 1C** and **S3.**

64

Fig. S5. PGAM2 and control confocal microscopy images for *P. tricornutum* plastid glycolysis proteins. Images complement those shown in Fig. 2A.

Fig. S6. Relative abundances and transcriptional coordination of plastidial enolase, PGAM1 and PGAM2. A: relative % accumulation of different plastid- and mitochondrial-associated carbon metabolism proteins (large points) and all known plastid-encoded or inferred plastid-targeted proteins (small points, with power-law trendline) for experimental proteomics of *Phaeodactylum tricornutum* total cell proteomes (horizontal axis) or plastid-enriched protein fractions (vertical axis), following (Huang, Pan et al. 2024). Only proteins detected in at least two replicates of plastid-enriched and total cell fractions are included, and abundances are renormalized based on the total abundances of these proteins. Both cpEnolase (Phatr3_J41515) and cpPGAM1A (Phatr3_J17086) are detected in the plastid-associated proteome fraction with similar frequencies to other plastid carbon metabolism proteins, whereas other predicted plastid-targeted PGAMs (e.g. cpPGAM1B, Phatr3_J51404; cPGAM2, Phatr3_J37201) are not. B: Spearman correlation coefficients of all genes across the version 3 annotation of the *Phaeodactylum tricornutum* genome against cpEnolase and cpPGAM1A; calculated from ranked transcript data (Liu, Storti et al. 2022) from two merged datasets, PhaeoNet (Ait-Mohamed, Novák Vanclová et al. 2020) and DiatomPortal (Ashworth, Turkarslan et al. 2016). Genes are coloured by inferred *in silico* localisation; and other annotated enolase and PGAM enzymes in the *Phaeodactylum* genome are shown as large, labelled points. Notably, while cpEnolase and cpPGAM1A show a strong positive *(r* > 0.8) coregulation to one another, other PGAM isoforms (e.g. cpPGAM1B, cpPGAM2) show less apparent coregulation to either of these two genes. These data support the experimental localisations shown in **Fig. 2A**, and identify cPGAM1A as the PGAM most likely to work cooperatively with cpEnolase from the homologues shown in **Fig. 1C.**

Fig. S7. Relative transcriptional regulation of cpEnolase and cpPGAM under nutrient, light and temperature stress conditions. A-C: the relative ratio of plastid to mitochondria-targeted gene isoform expression for enolase (vertical axis), PGAM1 (horizontal axis), and PGAM2 (bubble size) in published *Phaeodactylum* RNAseq

2318 data subject to nitrate limitation (McCarthy, Smith et al. 2017), phosphate starvation

2319 and addition (Cruz de Carvalho, Sun et al. 2016) and Circadian Fe enrichment and

2320 limitation (Smith, Gillard et al. 2016). While limited transcriptional responses are

2321 identifiable in response to changing N, P or Fe availability, the relative transcription of

2322 plastidial to mitochondrial-targeted enolase is substantially greater in RNA sampled

2323 in long day (> 12h post-illumination) conditions in **C**. **D**: relative fold changes in

2324 plastidial enolase and PGAM1 expression in published microarray data assembled in

2325 (Ashworth, Turkarslan et al. 2016), under different illumination conditions. Both

2326 Enolase and PGAM1 show substantial downregulation in dark-incubated (48h) and

2327 short post-illumination-incubated (< 0.5h) cultures, and show the greatest positive

2328 fold expression changes respectively > 16h and > 12h post-illumination. Specific data

2329 points showing either very high or low cpEnolase and cpPGAM1A expression are

2330 labelled.These data support the qRT-PCR and *Tara* Oceans observations of

2331 correlation of diatom cpEnolase and cpPGAM expression in **Fig. 2** and **Fig. 3**.

2332

2333 **Fig. S8. Identification of *Tara* Oceans homologs of diatom plastid-targeted**

2334 **enolase and PGAM enzymes. A:** Consensus rAxML JTT topologies of the

2335 phylogenetically verified *Tara* Oceans homologs of diatom plastidial enolase and

2336 PGAM enzymes and cultured species sequences, demonstrating reconciliation of

2337 retained homologs within monophyletic clades containing exclusively diatom

2338 plastidial isoforms amongst cultured species. **B:** *in silico* targeting predictions of all

2339 retrieved homologs inferred by BLAST alignment to be probably N-terminally

2340 complete, showing a strong enrichment in homologs with predicted plastid-targeting

2341 sequences. Sequences shown in this figure are analysed globally in **Fig. 3**.

2342

2343 **Fig. S9. Relative abundances of *Tara* Oceans diatom plastid glycolysis meta-**

2344 **genes.** Plots show relative abundances of meta-genes that group with **(i, iii)**

2345 cpEnolase and **(ii, iv)** cpPGAM1 sequences over individual size fractions of **(i, ii)**

2346 surface and **(iii, iv)** DCM meta-transcriptome **(left)** and -genome **(right)** data. These

2347 data, which allows us to identify whether specific trends are observed in different

2348 kinds of diatom cells, ranging from the nano to micro-metre scale, support global

2349 trends observed across from 0.8- 2000 μm filtered size fractions and surface layers

2350 shown in **Fig. 3**.

2351

Fig. S10. Normalised atitudinal regressions of *Tara* cpEnolase and cpPGAM1 sequences. Scatterplots of *Tara* Ocean expression patterns of sequences assigned phylogenetically to diatom cpEnolase and cpPGAM1A against station latitude. Abundances are shown for 0.8-2000 μm surface and DCM sample meta-transcriptome data, and are normalised relative to **(A)** total diatom metaT abundances at each station and **(B)** the corresponding metaG abundances for diatom cpEnolase and cpPGAM1A. Best-fit (linear) regression lines are provided for each depth. In each case, a significant positive correlation between latitude and relative expression is observed, consistent with global distributions observed in **Fig. 3.**

Fig. S11. Total relative abundances of meta-genes phylogenetically reconciled to diatom PGAM2 in 0.8- 2000 μm filtered surface samples. Plots showing **(A)** meta-transcriptome and **(B)** meta-genome data, showing effective congruence between both, in contrast to the high latitudinal abundance specific to meta-transcriptome data for diatom cpEnolase and cpPGAM1 as per **Fig. 3**.

Fig. S12. Occurrence and mean coverage depth of *Tara* Oceans MAGs divided by chloroplast glycolysis state. This figure shows mapped distributions for *Tara* meta-genome assembled genomes (MAGs (Delmont, Gaia et al. 2022)) pertaining to **(A)** diatoms, **(B)** chlorophytes, and **(C)** other algal groups (haptophytes, pelagophytes, dictyochophytes, chrysophytes, bolidophytes, cryptomonads) containing members with inferred lower half plastidial glycolysis. MAGs are divided by the inferred occurrence of which chloroplast-targeted enolase and PGAM enzymes could be inferred using combined RbH to *Phaeodactylum* queries, PFAM annotation, and in silico targeting prediction (TargetP, WolfPSort, PredAlgo, HECTAR, ASAFind): **(i)** detection of plastid-targeted homologues of both enzymes; **(ii)** detection of cpEnolase or cpPGAM only; **(iii)** detection of neither. Bubble sizes correspond to the mean vertical coverage of meta-gene reads recruited to each MAG as a proxy of abundance. In each case the linear correlation and P-value (two-tailed *t*-test) of correlation between mean vertical mapped depth and absolute latitude is provided. Notably there is a positive correlation between the retrieval of either plastid glycolysis protein and greater mapped read depth at high latitudes in diatoms, and also the retrieval of both plastid glycolysis proteins and greater mapped read depth at

67

high latitudes in chlorophytes, although no such trend is observed in other algal groups. The latitudinal associations observed for diatom MAG abundances support expression trends shown in **Fig. 3,** although the chlorophyte MAG abundances point to the presence of novel plastid glycolytic pathways absent from the cultured species shown in **Fig. 1**.

Fig. S13. Genotypes of *P. tricornutum* glycolysis knockout lines. A: alignments of the two CRISPR regions targeted for mutagenesis of cpEnolase (Phatr3_J41515) and cpPGAM1A (Phatr3_J17086), and the genotypes obtained from Sanger sequences of homozygous CRISPR knockouts obtained for each gene. **B:** average relative expression level of each mutated gene, assessed by quantitative RT-PCR with two primer combinations and normalised against two housekeeping genes (RNA polymerase II and TATA binding protein), expressed as a % of the relative expression levels calculated in two empty vector expression controls. One-way *t*-test significance levels of the knockdown of gene expression in each knockout line compared to the empty vector controls are provided. Knockout lines shown in this figure were used for growth and integrative 'omic analyses as per **Figs. 3-6**.

Fig. S14. Absolute and individual growth phenotypes of cpEnolase and cpPGAM1A CRISPR-Cas9 knockout mutant lines. A: growth curves of knockout lines, shown as per **Fig. 4**, but with absolute as opposed to logarithmic cell concentrations B: scatterplot showing the average and standard deviation relative growth rates for each cell line studied under 19C CL (vertical) and 19C LD (horizontal axis). Each point corresponds to an individual line, with genotype indicated by point colours, and standard deviations of growth rates by error bars. Despite individual variances in growth rate between lines, knockout lines show consistently slower growth than empty vector controls under both conditions, particularly 19C CL.

Fig. S15. Measured photo-physiology of glycolysis knockout lines A: Curves for **(i-ii)** relative electron transport (rETR) of photosystem II fitted as a function of light intensity) and **(iii-iv)** photoprotective non-photochemical quenching (NPQ) fitted as a function of E. Separate values are shown for cultures in CL **(i, iii)** and LD **(ii, iv)** growth conditions. Data points are the mean between the average values (*n*=2-4) measured in each strain within each genotype (Control = 2, cpEnolase

2420 complemented = 2, cpPGAM1A complemented = 3, cpEnolase knockout = 6,

2421 cpPGAM1A knockout = 3). **B:** Violin plots of PSII functional absorption cross-section

2422 (σPSII), measured with a MINIFIRe spectrometer for glycolysis mutant versus control

2423 lines under each growth conditions. Significantly different values observed for

2424 knockout and complementation mutants relative to control lines (one-way ANOVA, P

2425 < 0.05) are asterisked, with asterisk colour corresponding to the line considered.

2426 Each boxplot includes all measured/ fitted values for each strain within a mutant line.

2427 The absence of clear photosynthetic defects contrasts with the diminished growth of

2428 knockout lines, as per **Fig. 4.**

2429

2430 **Fig. S16: Bar plots of the mean and standard deviation of the ratios of 39**

2431 **metabolites assessed by GC-MS in plastid glycolysis mutant lines under the**

2432 **three tested experimental conditions.** Data support the Volcano Plots shown in

2433 **Fig. 6**. Metabolites are sorted in ranked decreasing accumulation in mutant lines over

2434 all three conditions. Metabolites inferred to be differentially accumulated (one-way

2435 ANOVA) in each mutant line and condition are asterisked.

2436

2437 **Fig. S17. Lipid accumulation profiles under 19C LD conditions**. **A:** Volcano Plots

2438 showing (horizontal axis) $\log_2$ accumulation ratios and (vertical axis) $-\log_{10}$ one-way

2439 ANOVA, two-tailed Pvalues for separation of mean proportions of specific fatty acids,

2440 across all fatty acids observed in a specific lipid class in glycolysis mutants versus

2441 control lines, supporting the global scatter- and violin plots shown in **Fig. 7**. Specific

2442 lipids that show extreme (P < 0.01) differences in accumulation between both mutant

2443 genotypes and control lines are labelled, and coloured by lipid class. **B:** Bar plots

2444 showing total DGTA lipid class distributions in all three lines under these conditions.

2445 These data suggest limited changes in glycolysis mutant lipid architecture, barring a

2446 probable over-accumulation of *sn*-1 C16 in gycolysis mutant lipid pools, and

2447 corresponding under-accumulation of *sn*-1 C20 in mutant DGTA pools.

2448

2449 **Fig. S18. Lipid accumulation profiles under 19C CL conditions. A:** Volcano plots

2450 showing (horizontal axis) $\log_2$ accumulation ratios and (vertical axis) $-\log_{10}$ one-way

2451 ANOVA, two-tailed Pvalues for separation of mean proportions of specific fatty acids,

2452 across all fatty acids observed in a specific lipid class in glycolysis mutants versus

2453 control lines, and **B: bar plots** of SQDG and DGTA accumulation in lines harvested

2454   under **19C CL.** Data are shown as per **Fig. S17** and support global scatter- and violin

2455   plots shown in **Fig. 7.** These data suggest similar changes in glycolysis mutant lipid

2456   architecture to **19C LD**, including probable over-accumulations of *sn*-1 C16 in lieu of

2457   C20 and C14 in cpEnolase and cpPGAM1A mutant SQDG and MGDG pools.

2458

2459   **Fig. S19. Lipid accumulation profiles under 8C CL conditions.** Volcano plots

2460   showing (horizontal axis) $\log_2$ accumulation ratios and (vertical axis) $-\log_{10}$ ANOVA

2461   Pvalues for separation of mean proportions of specific fatty acids, across all fatty

2462   acids observed in a specific lipid class in cpEnolase mutants versus control lines, and

2463   cpEnolase mutants versus cpPGAM1A mutants harvested under 8C CL conditions.

2464   Data are shown as per **Fig. S17** and support global scatter- and violin plots shown in

2465   **Fig. 7.** No sigificantly differentially accumulated ($P < 10^{-05}$) lipids were observed in

2466   corresponding comparisons of cpPGAM1A mutants and control lines. These data

2467   suggest specific overaccumulations in short-chain *sn*-1 MGDG, and *sn*-2 SQDG, and

2468   C20 *sn-1* DGTA in cpEnolase mutants compared to other lines.

2469

2470   **Fig. S20. Schematic diagram of the reaction kinetics measured for *P.***

2471   ***tricornutum* cpEnolase and cPGAM1A enzymes**. The measured activities of this

2472   assay are shown in **Fig. 8.** Common enzymes are shown in green, enzymes unique

2473   to the glycolytic assay in blue, and enzymes unique to the gluconeogenic assay in

2474   red. Reaction intermediates and reversible substrates are shown in yellow and gray

2475   respectively.

2476

2477   **Supplemental Dataset S1. Phylogenetic diversity of Enolase and PGAM**

2478   **sequences from across the tree of life.**

2479

2480   **Supplemental Dataset S2. Transcriptional and localisation patterns of ptPGAM**

2481   **and ptEnolase genes in *Phaeodactylum tricornutum*.**

2482

2483   **Supplemental Dataset S3. *Tara* Oceans analysis of diatom plastidial glycolysis.**

2484

2485   **Supplemental Dataset S4. Genotyping, growth dynamics and photophysiology**

2486   **in *P. tricornutum* plastidial glycolysis mutant lines.**

2487

2488 **Supplemental Dataset S5. Differentially and conditionally expressed genes in**

2489 ***P. tricornutum* plastidial glycolysis mutants.**

2490

2491 **Supplemental Dataset S6. Lipid and metabolite profiles of *P. tricornutum***

2492 **plastidial glycolysis mutant lines, and measured reaction kinetics of expressed**

2493 **enzymes.**
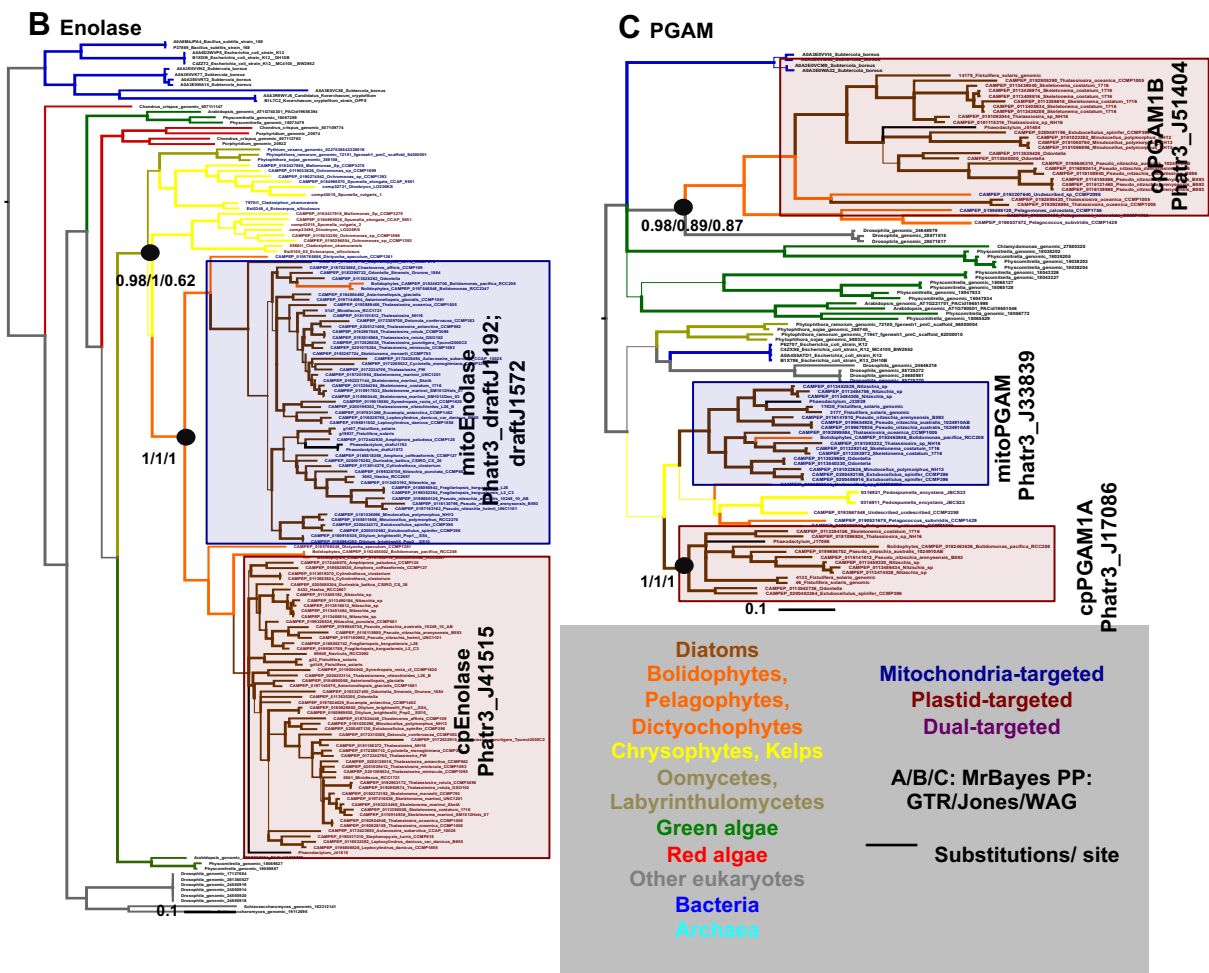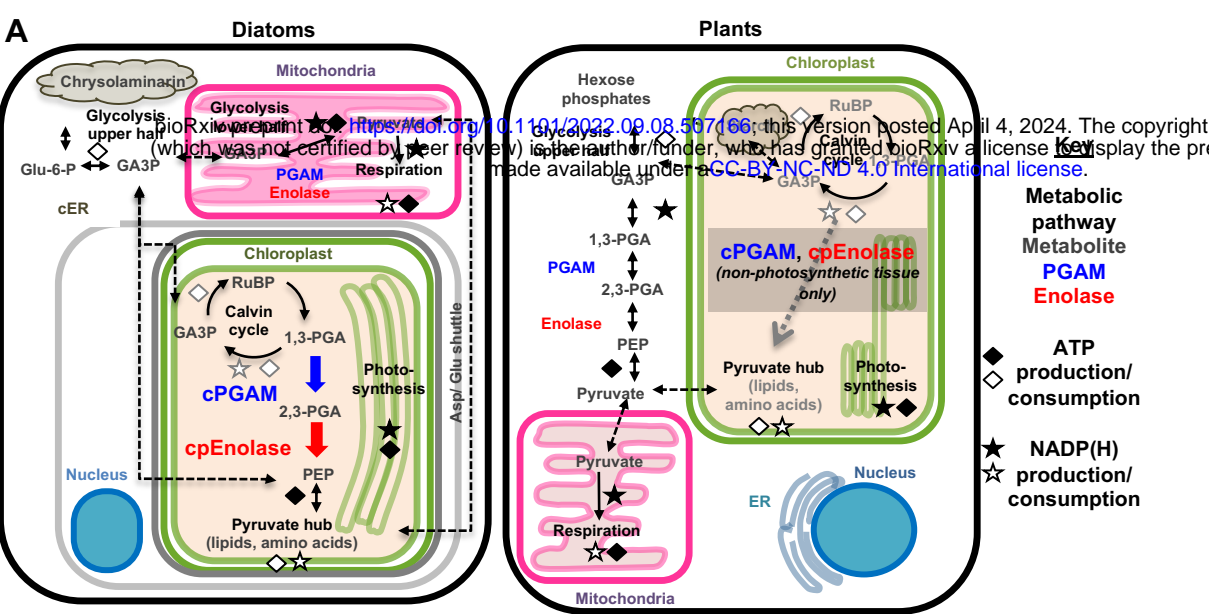
Fig. 1. Metabolic context and evolution of the lower half of diatom plastidial glycolysis-gluconeogenesis. A: schematic comparison of diatom and plant core carbon metabolism, highlighting the localization and functions of two enzymes in the lower half of glycolysis-gluconeogenesis (phospho-glycerate mutase, and enolase) whose localization to the chloroplast can connect endogenous enzymes in the Calvin cycle and pyruvate hub to create a complete glycolytic-gluconeogenic-gluconeogenic pathway. Abbreviations: GA3P- glyceraldehyde-3-phosphate; 1,3-PGA and 2,3-PGA- 1,3 and 2,3 bis-phosphoglycerate; Glu-6-P-glucose-6-phosphate; PEP- phospho-enol-pyruvate; RuBP- ribulose *bis*-phosphate; PGAM- phospho-glycerate mutase; cER- chloroplast: endoplasmic reticulum. **B, C:** consensus MrBayes topologies realised with three substitution matrices (GTR, Jones, WAG) of a 163 taxa x 413 aa alignment of organelle-targeted enolase and 105 taxa x 220 aa alignment of selected organelle-targeted PGAM1 enzymes from diatoms and their closest relatives, identifying recent duplications and recruitments of respiratory glycolytic-gluconeogenic enzymes from the mitochondria to plastid in diatoms and their closest relatives. Branch lines correspond to the frequency with which a given branching relationship was recovered, with thick branches identified by all three substitution matrices.

A

	GFP	Chlorophyll	Bright-Field	Merge

Phatr3_J41515 (cpEnolase): GFP
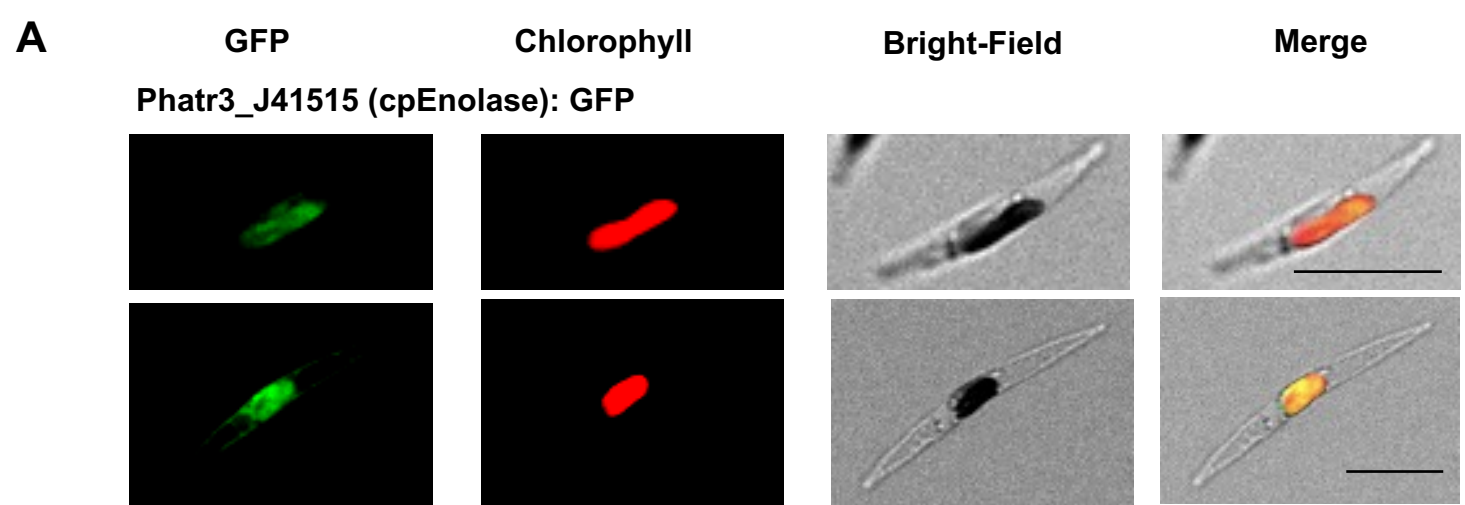
Phatr3_J17086 (cPGAM1): GFP
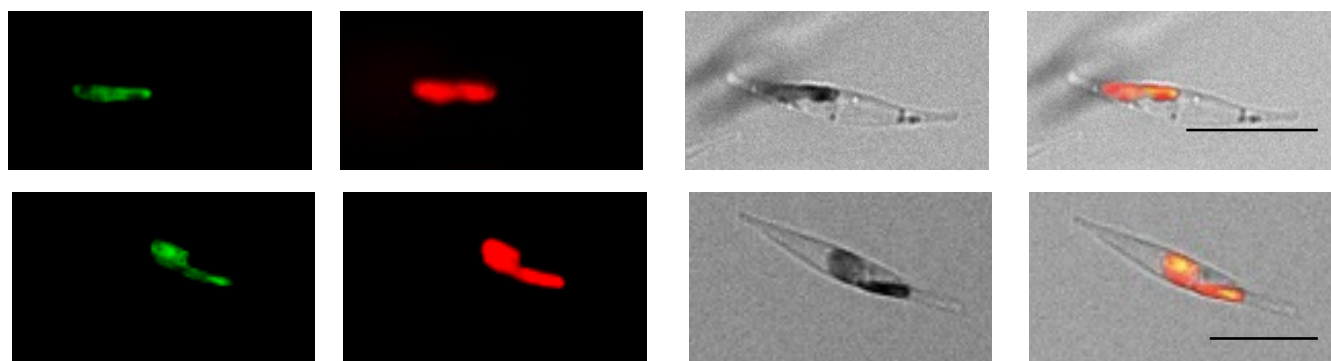
B
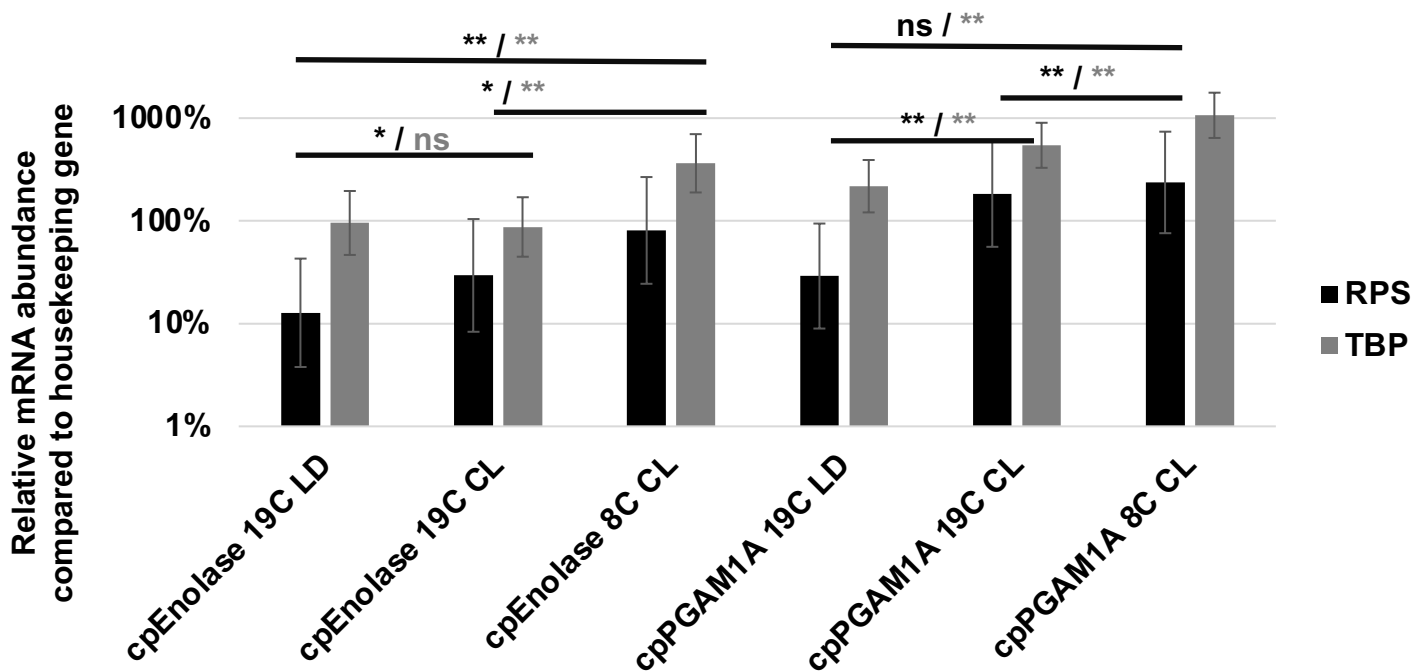
Fig. 2. Localisation and expression of *Phaeodactylum tricornutum* cpEnolase and cpPGAM1A.
A: : overlay images of GFP-tagged full-length cpEnolase (Phatr3_J41515) and cpPGAM1A
(Phatr3_J17086) constructs (green), chlorophyll (red) and bright-field images of transformant *P.
tricornutum* lines. Scale bar: 10 μm. **B:** quantitative RT-PCR (qRT-PCR) of cpEnolase and cpPGAM1A
expression in mid-exponential phase cells harvested at the mid-point of a 19C 12h light: 12h dark cycle
(19LD); at the same timepoint but under 24h continuous light (19CL); and under 8C and continuous light
(8CL). Relative expression levels were normalised against two housekeeping genes (RPS, RNA
polymerase subunit 1; TBP, Tata binding protein) that show invariant expression in response to light
cycles in *Phaeodactylum* per (Sachse, Sturm et al. 2013). *: significantly different expression levels,
one-way ANOVA, P < 0.05; **, the same, P < 0.001.
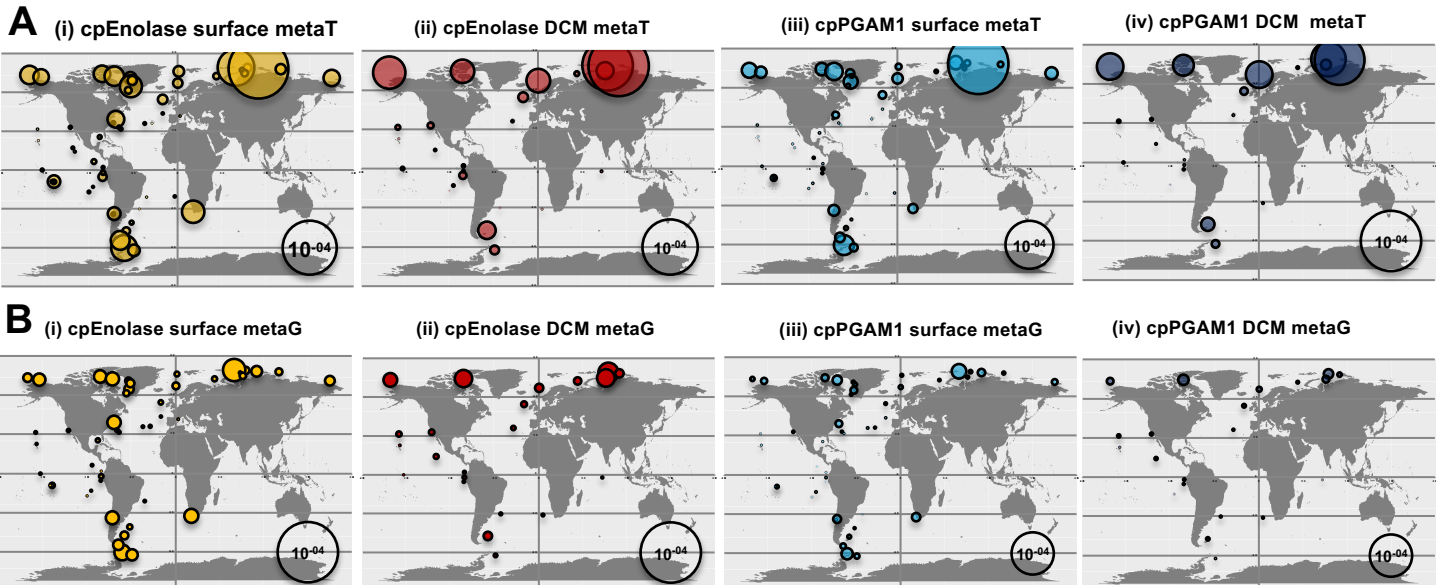
Fig. 3. Environmental distributions of diatom plastidial lower half glycolysis-gluconeogenesis meta-genes. Total transcriptome (**A**) and genome (**B**) relative abundances, sampled from all (0.8-2000µm) size fractions and surface layer (**i,iii**) or DCM (**ii,iv**) stations for *Tara* Oceans meta-genes phylogenetically resolved to diatom cpEnolase (**i,ii**) and cpPGAM1 (**iii,iv**). These data provide a global overview of *Tara* Oceans meta-gene abundances, in complement to data from individual size fractions shown in **Fig. S9**. These data demonstrate higher meta-transcript abundance without commensurate increases in meta-gene abundance at high northern and southern latitudes.
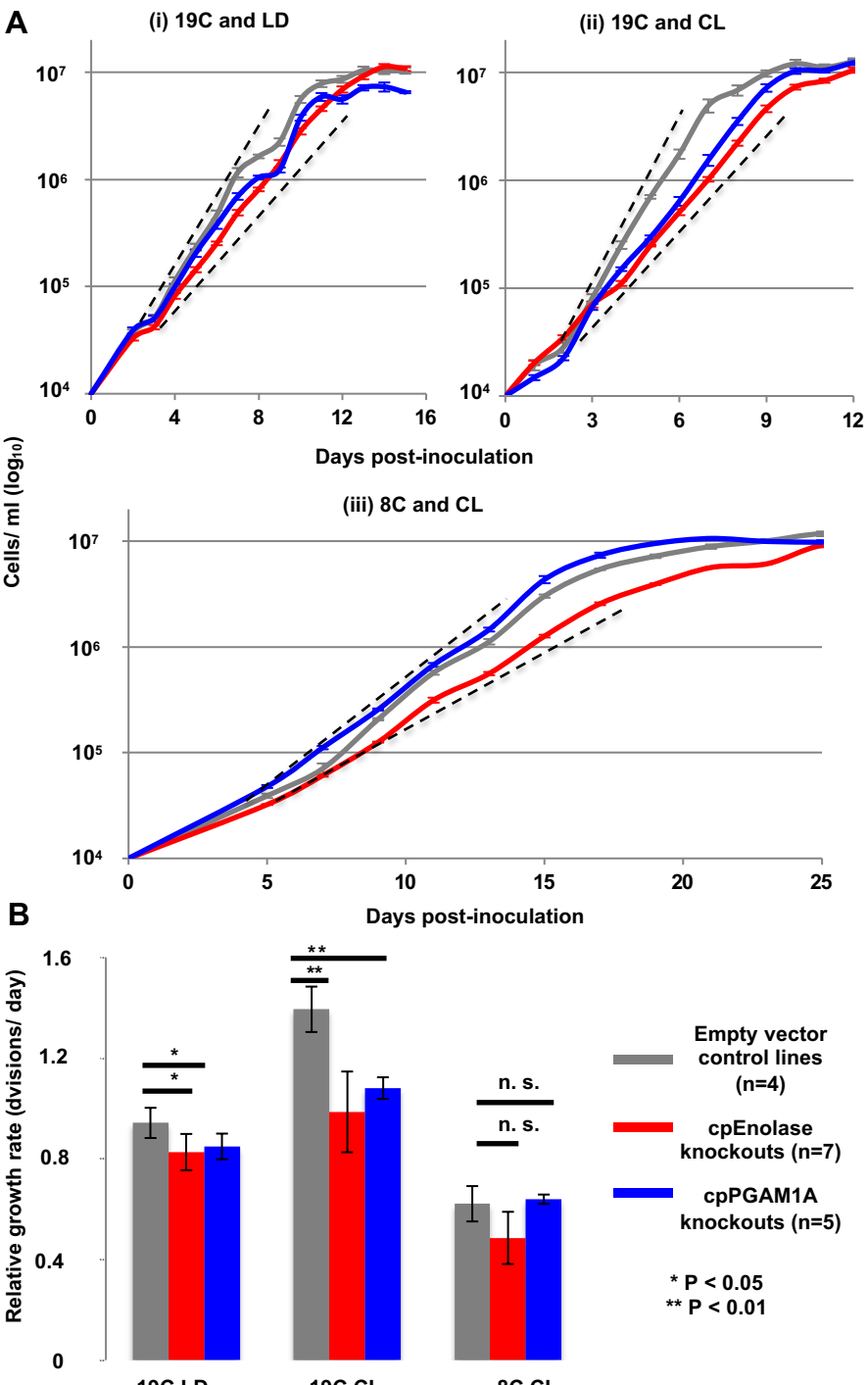
Fig. 4. Growth phenotypes of cpEnolase and cpPGAM1A CRISPR-Cas9 knockout mutant and zeocin-resistant empty vector control *P. tricornutum* lines. A: exemplar growth curves from single experiments realised for *P. tricornutum* lines in 50 µE m^{-2} s^{-1} illumination, non-shaken cultures and replete ESAW media, under three conditions- **(i)** 19°C and 12h light: 12h dark Circadian cycles (« 19C LD »); **(ii)** 19°C and 24h continuous light (« 19C CL »); and **(iii)** 8°C and 24h continuous light (« 8C CL »). Hashed black lines show the approximative concentrations (between 5 x10^4 and 4 x 10^6 cells ml^{-1}) over which growth rates were calculated). **B:** mean relative log phase growth rates of each genotype under each condition, measured through a minimum of three biological replicates and two technical repetitions (six measurements per line, minimum 24 measurements per genotype), over five time-points with linear ($r^2 > 0.95$ relationship between log cell density and time). Asterisks indicate significant differences as inferred by one-way ANOVA. An alternative version of this figure showing absolute growth rates of individual cell lines is provided in **Fig. S14**.
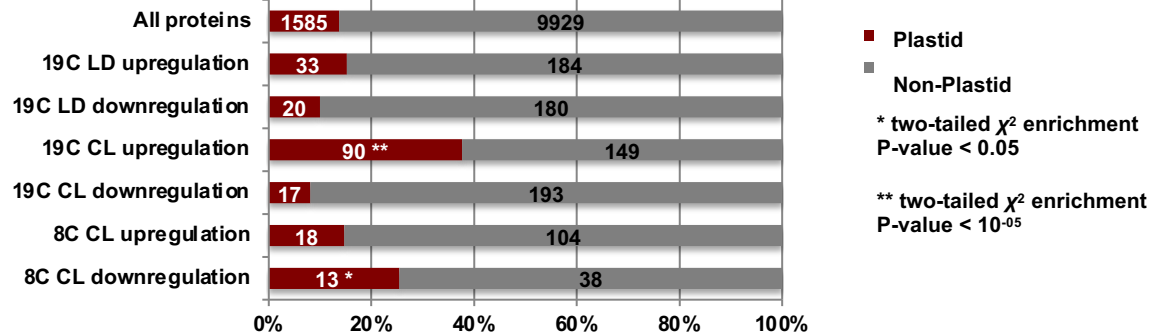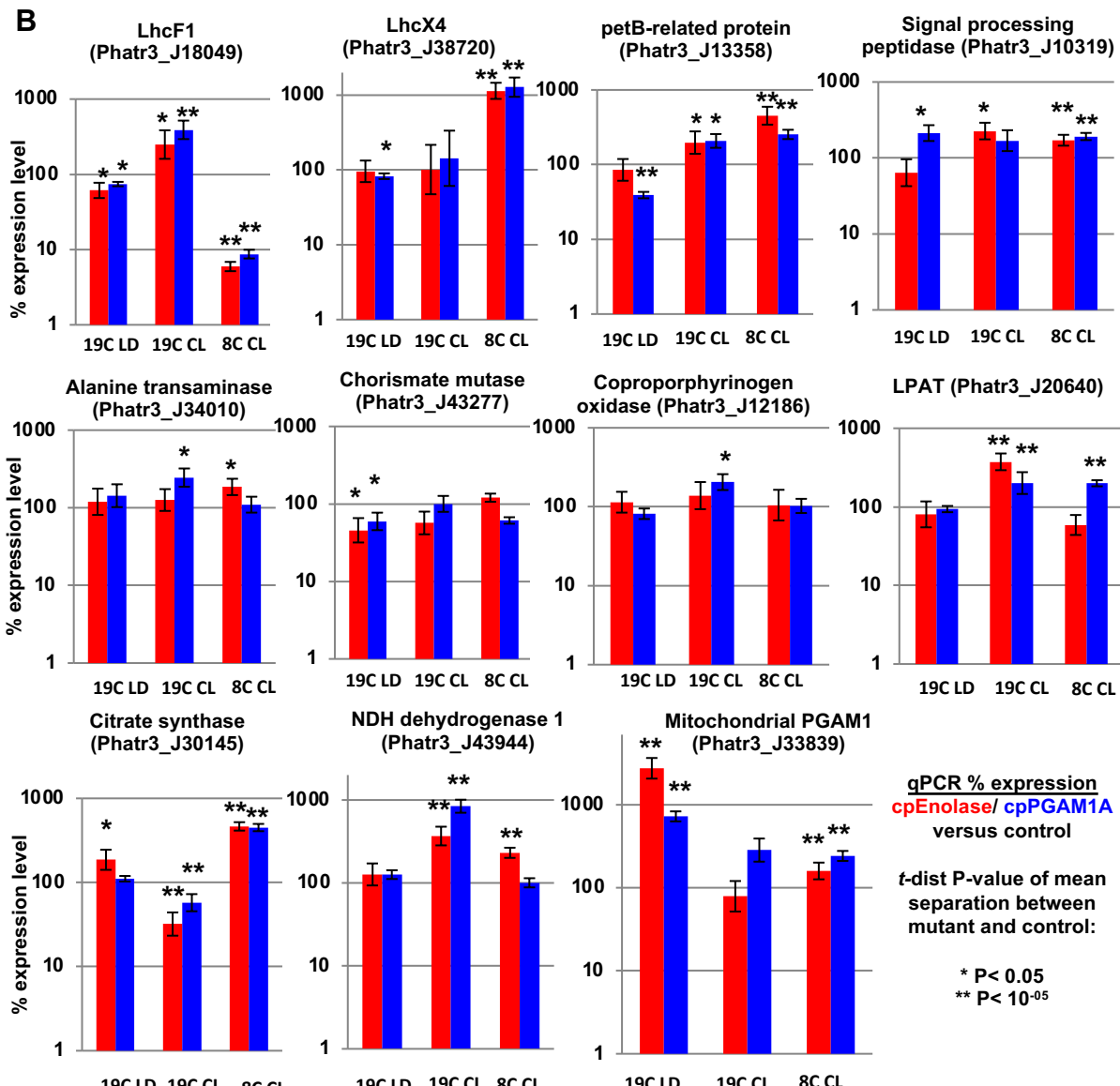
Fig. 5. Changes in plastid and mitochondrial metabolic architecture inferred from gene expression analyses. A: predicted consensus localizations (either: chloroplast, or non-chloroplast) from ASAFind (Gruber, Rocap et al. 2015) and HECTAR (Gschloessl, Guermeur et al. 2008) of all genes inferred (P < 0.05, fold-change expression >2) to be up- or down-regulated in both cpEnolase and cpPGAM1A knockout compared to control lines under 19C LD, 19C CL and 8C CL conditions. Significantly enriched localisations (two-tailed chi-squared test) are asterisked. **B:** relative mRNA abundances of eleven genes encoding exemplar
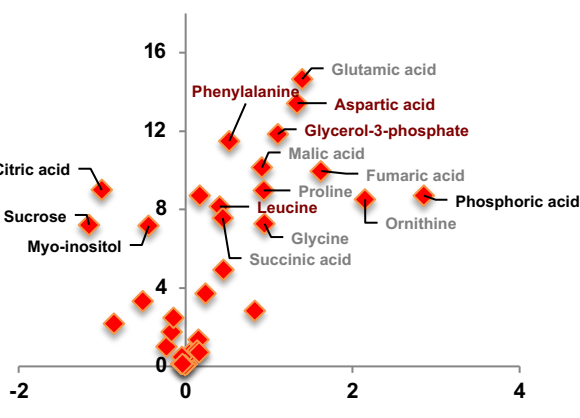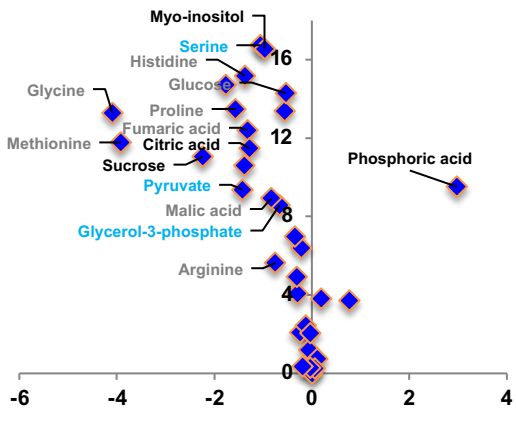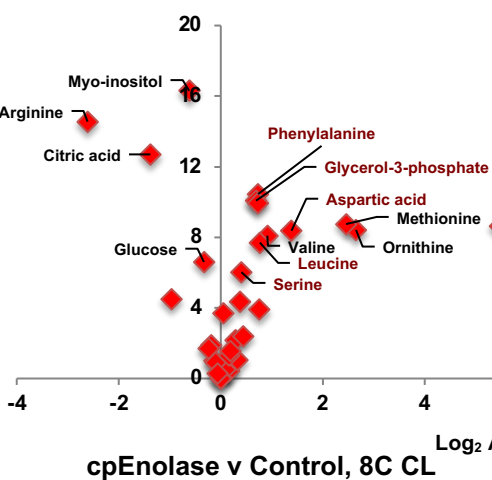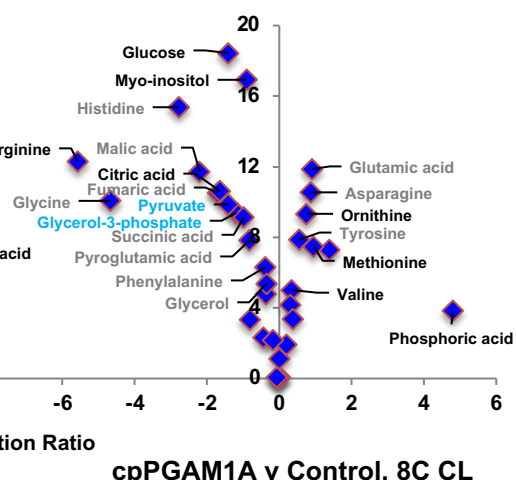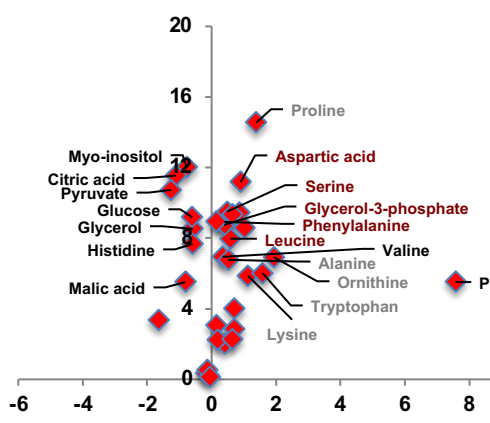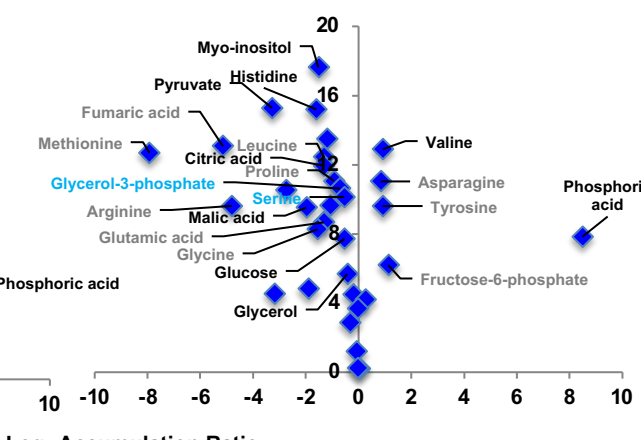
Fig. 6. Volcano plots of differentially accumulated metabolites assessed by GC-MS. Scatterplots of the $\log_2$ accumulation ratios and $-\log_{10}$ P-values of difference in the mass, ribitol and quality-control-normalised abundances of 39 sugar and amino acid metabolites in cpEnolase and cpPGAM1A knockout compared to empty vector control lines, measured by GC-MS in all three experimental conditions tested. Metabolites that show a differential accumulation in each plot ($P < 10^{-05}$) are labelled, with metabolites that show a differential accumulation in both knockout lines in each condition shown in black text, and five metabolites that are uniquely over-accumulated in cpEnolase knockout lines under all three conditions shown in dark red text.
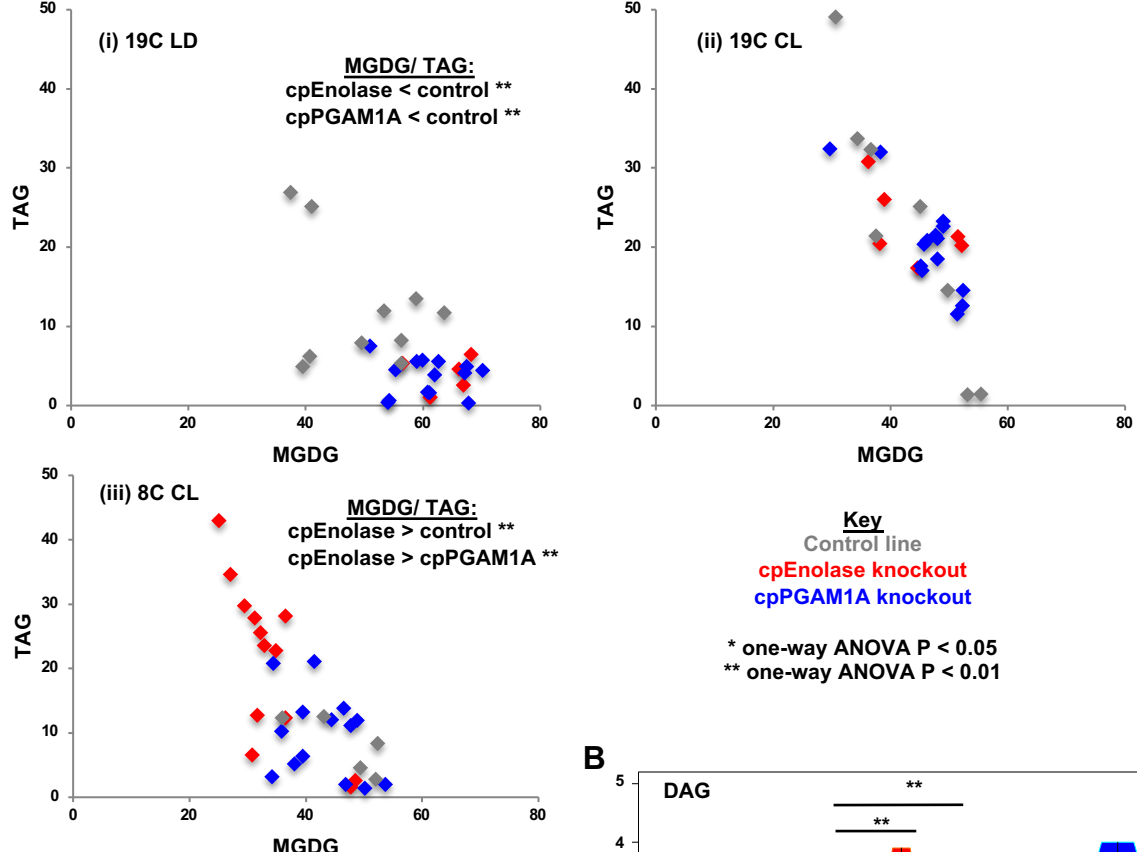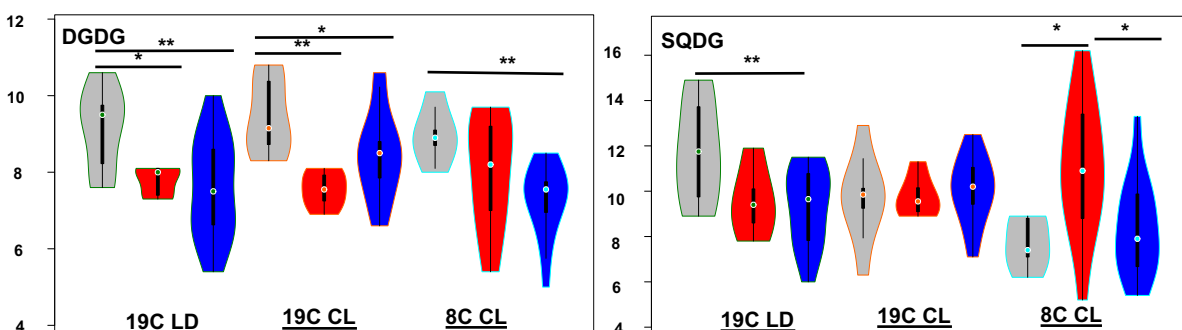
Fig. 7. LC-MS lipid distributions in glycolysis-gluconeogenesis mutant lines.
A: scatterplots of relative proportions of MGDG and TAG in total lipid LC-MS samples in cpEnolase and cpPGAM1A knockout lines and empty vector controls under each growth condition, showing increased MGDG: TAG in glycolysis knockout lines under 19C, and the inverse relationship in cpEnolase knockout lines only under 8C. **B**: violin plots of relative abundances of three further lipid categories inferred to differentially accumulate in glycolysis knockout lines under different growth conditions. Significant differences between knockout and control lines (one-way ANOVA) are asterisked.
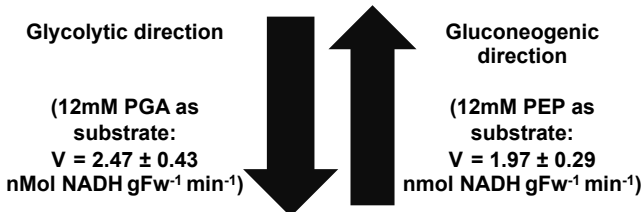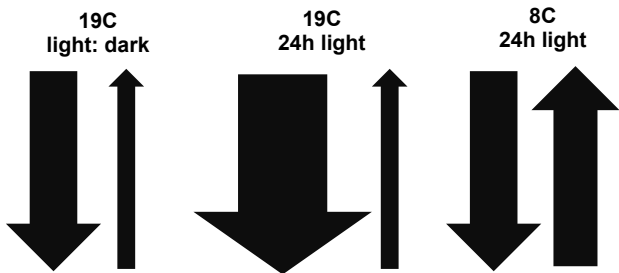
Fig. 8. Proposed kinetic activities of *P. tricornutum* plastid lower glycolysis-gluconeogenesis. Schematic diagram showing potential inferred roles of lower half diatom plastid glycolysis-gluconeogenesis in each environmental condition tested. The measured V_{max} of purified cpEnolase and cPGAM1A supplemented with 3-PGA (glycolytic direction) or PEP (gluconeogenic direction) are provided for 12mM substrate in each case

Parsed Citations

Abida, H., L. J. Dolch, C. Meï, V. Villanova, M. Conte, M. A. Block, G. Finazzi, O. Bastien, L. Tirichine, C. Bowler, F. Rébeillé, D. Petroutsos, J. Jouhet and E. Maréchal (2015). Membrane glycerolipid remodeling triggered by nitrogen and phosphorus starvation in Phaeodactylum tricornutum. Plant Physiol 167(1): 118-136.
Google Scholar: Author Only Title Only Author and Title

Ait-Mohamed, O., A. M. G. Novák Vanclová, N. Joli, Y. Liang, X. Zhao, A. Genovesio, L. Tirichine, C. Bowler and R. G. Dorrell (2020). PhaeoNet: a holistic RNAseq-based portrait of transcriptional coordination in the model diatom Phaeodactylum tricornutum. Frontiers Plant Sci 11: 590949.
Google Scholar: Author Only Title Only Author and Title

Allen, A. E., C. L. Dupont, M. Obornik, A. Horak, A. Nunes-Nesi, J. P. McCrow, H. Zheng, D. A. Johnson, H. Hu, A. R. Fernie and C. Bowler (2011). Evolution and metabolic significance of the urea cycle in photosynthetic diatoms. Nature 473(7346): 203-+.
Google Scholar: Author Only Title Only Author and Title

Almagro Armenteros, J. J., K. D. Tsirigos, C. K. Sønderby, T. N. Petersen, O. Winther, S. Brunak, G. von Heijne and H. Nielsen (2019). SignalP 5.0 improves signal peptide predictions using deep neural networks. Nat Biotechnol 37(4): 420-423.
Google Scholar: Author Only Title Only Author and Title

Andriotis, V. M., N. J. Kruger, M. J. Pike and A. M. Smith (2010). Plastidial glycolysis in developing Arabidopsis embryos. New Phytol 185(3): 649-662.
Google Scholar: Author Only Title Only Author and Title

Anoman, A. D., M. Flores-Tornero, S. Rosa-Telléz, J. Muñoz-Bertomeu, J. Segura and R. Ros (2016). The specific role of plastidial glycolysis in photosynthetic and heterotrophic cells under scrutiny through the study of glyceraldehyde-3-phosphate dehydrogenase. Plant Signal Behav 11(3): e1128614.
Google Scholar: Author Only Title Only Author and Title

Ashworth, J., S. Turkarslan, M. Harris, M. V. Orellana and N. S. Baliga (2016). Pan-transcriptomic analysis identifies coordinated and orthologous functional modules in the diatoms Thalassiosira pseudonana and Phaeodactylum tricornutum. Mar Genomics 26: 21-28.
Google Scholar: Author Only Title Only Author and Title

Bai, Y., T. Cao, O. Dautermann, P. Buschbeck, M. B. Cantrell, Y. Chen, C. D. Lein, X. Shi, M. A. Ware, F. Yang, H. Zhang, L. Zhang, G. Peers, X. Li and M. Lohr (2022). Green diatom mutants reveal an intricate biosynthetic pathway of fucoxanthin. Proc Natl Acad Sci USA 119(38): e2203708119.
Google Scholar: Author Only Title Only Author and Title

Bailleul, B., N. Berne, O. Murik, D. Petroutsos, J. Prihoda, A. Tanaka, V. Villanova, R. Bligny, S. Flori, D. Falconet, A. Krieger-Liszkay, S. Santabarbara, F. Rappaport, P. Joliot, L. Tirichine, P. G. Falkowski, P. Cardol, C. Bowler and G. Finazzi (2015). Energetic coupling between plastids and mitochondria drives CO2 assimilation in diatoms. Nature 524(7565): 366-3267.
Google Scholar: Author Only Title Only Author and Title

Behrenfeld, M. J., K. H. Halsey, E. Boss, L. Karp-Boss, A. J. Milligan and G. Peers (2021). Thoughts on the evolution and ecological niche of diatoms. Ecol Monograph 91(3): e01457.
Google Scholar: Author Only Title Only Author and Title

Broddrick, J. T., N. Du, S. R. Smith, Y. Tsuji, D. Jallet, M. A. Ware, G. Peers, Y. Matsuda, C. L. Dupont, B. G. Mitchell, B. O. Palsson and A. E. Allen (2019). Cross-compartment metabolic coupling enables flexible photoprotective mechanisms in the diatom Phaeodactylum tricornutum. New Phytol 222: 1364-1379.
Google Scholar: Author Only Title Only Author and Title

Bromke, M. A. (2013). Amino Acid biosynthesis pathways in diatoms. Metabolites 3(2): 294-311.
Google Scholar: Author Only Title Only Author and Title

Buck, J. M., C. Río Bártulos, A. Gruber and P. G. Kroth (2018). Blasticidin-S deaminase, a new selection marker for genetic transformation of the diatom. PeerJ 6: e5884.
Google Scholar: Author Only Title Only Author and Title

Buck, J. M., J. Sherman, C. R. Bártulos, M. Serif, M. Halder, J. Henkel, A. Falciatore, J. Lavaud, M. Y. Gorbunov, P. G. Kroth, P. G. Falkowski and B. Lepetit (2019). Lhcx proteins provide photoprotection via thermal dissipation of absorbed light in the diatom Phaeodactylum tricornutum. Nat Commun 10(1): 4167.
Google Scholar: Author Only Title Only Author and Title

Buseman, C. M., P. Tamura, A. A. Sparks, E. J. Baughman, S. Maatta, J. Zhao, M. R. Roth, S. W. Esch, J. Shah, T. D. Williams and R. Welti (2006). Wounding stimulates the accumulation of glycerolipids containing oxophytodienoic acid and dinor-oxophytodienoic acid in Arabidopsis leaves. Plant Physiol 142(1): 28-39.
Google Scholar: Author Only Title Only Author and Title

Bustin, S. A., V. Benes, J. A. Garson, J. Hellemans, J. Huggett, M. Kubista, R. Mueller, T. Nolan, M. W. Pfaffl, G. L. Shipley, J. Vandesompele and C. T. Wittwer (2009). The MIQE Guidelines: Minimum Information for publication of Quantitative real-time PCR Experiments. Clin Chem 55(4): 611-622.
Google Scholar: Author Only Title Only Author and Title

Capella-Gutiérrez, S., J. M. Silla-Martínez and T. Gabaldón (2009). trimAl: a tool for automated alignment trimming in large-scale phylogenetic analyses. Bioinformatics 25(15): 1972-1973.
Google Scholar: Author Only Title Only Author and Title

Carradec, Q., E. Pelletier, C. Da Silva, A. Alberti, Y. Seeleuthner, R. Blanc-Mathieu, G. Lima-Mendez, F. Rocha, L. Tirichine, K. Labadie, A. Kirilovsky, A. Bertrand, S. Engelen, M. A. Madoui, R. Méheust, J. Poulain, S. Romac, D. J. Richter, G. Yoshikawa, C. Dimier, S. Kandels-Lewis, M. Picheral, S. Searson, O. Jaillon, J. M. Aury, E. Karsenti, M. B. Sullivan, S. Sunagawa, P. Bork, F. Not, P. Hingamp, J. Raes, L. Guidi, H. Ogata, C. de Vargas, D. Iudicone, C. Bowler, P. Wincker and Tara Oceans Coordinators (2018). A global ocean atlas of eukaryotic genes. Nat Commun 9(1): 373.
Google Scholar: Author Only Title Only Author and Title

Carrera, D., G. M. George, M. Fischer-Stettler, F. Galbier, S. Eicke, E. Truernit, S. Streb and S. C. Zeeman (2021). Distinct plastid fructose bisphosphate aldolases function in photosynthetic and non-photosynthetic metabolism in Arabidopsis. J Exp Bot 72(10): 3739-3755.
Google Scholar: Author Only Title Only Author and Title

Chang, Y. F., J. S. Imam and M. F. Wilkinson (2007). The nonsense-mediated decay RNA surveillance pathway. Annu Rev Biochem 76: 51-74.
Google Scholar: Author Only Title Only Author and Title

Cruz de Carvalho, M. H., H. X. Sun, C. Bowler and N. H. Chua (2016). Noncoding and coding transcriptome responses of a marine diatom to phosphate fluctuations. New Phytol 210(2): 497-510.
Google Scholar: Author Only Title Only Author and Title

Delmont, T. O., M. Gaia, D. D. Hinsinger, P. Frémont, C. Vanni, A. Fernandez-Guerra, A. M. Eren, A. Kourlaiev, L. d'Agata, Q. Clayssen, E. Villar, K. Labadie, C. Cruaud, J. Poulain, C. Da Silva, M. Wessner, B. Noel, J.-M. Aury, S. Sunagawa, S. G. Acinas, P. Bork, E. Karsenti, C. Bowler, C. Sardet, L. Stemmann, C. de Vargas, P. Wincker, M. Lescot, M. Babin, G. Gorsky, N. Grimsley, L. Guidi, P. Hingamp, O. Jaillon, S. Kandels, D. Iudicone, H. Ogata, S. Pesant, M. B. Sullivan, F. Not, K.-B. Lee, E. Boss, G. Cochrane, M. Follows, N. Poulton, J. Raes, M. Sieracki, S. Speich and E. Pelletier (2022). Functional repertoire convergence of distantly related eukaryotic plankton lineages abundant in the sunlit ocean. Cell Genom 2(5): 100123.
Google Scholar: Author Only Title Only Author and Title

Demé, B., C. Cataye, M. A. Block, E. Maréchal and J. Jouhet (2014). Contribution of galactoglycerolipids to the 3-dimensional architecture of thylakoids. FASEB J 28(8): 3373-3383.
Google Scholar: Author Only Title Only Author and Title

Dolch, L. J. and E. Maréchal (2015). Inventory of fatty acid desaturases in the pennate diatom Phaeodactylum tricornutum. Mar Drugs 13(3): 1317-1339.
Google Scholar: Author Only Title Only Author and Title

Dorrell, R. G., G. Gile, G. McCallum, R. Méheust, E. P. Bapteste, C. M. Klinger, L. Brillet-Guéguen, K. D. Freeman, D. J. Richter and C. Bowler (2017). Chimeric origins of ochrophytes and haptophytes revealed through an ancient plastid proteome. Elife 6, 23717.
Google Scholar: Author Only Title Only Author and Title

Dorrell, R. G., A. M. G. Novák Vanclová, M. Penot, J. J. Pierella Karlusich, C. Bowler, S. Liu, E. Maréchal, J. Jouhet, B. Bailleul and D. Croteau (2022). Functional physiology of novel diatom chloroplast proteins. Open Science Foundation. https://osf.io/89vm3/.
Google Scholar: Author Only Title Only Author and Title

Emanuelsson, O., S. Brunak, G. von Heijne and H. Nielsen (2007). Locating proteins in the cell using TargetP, SignalP and related tools. Nat Protocol 2(4): 953-971.
Google Scholar: Author Only Title Only Author and Title

Erdene-Ochir, E., B. K. Shin, B. Kwon, C. Jung and C. H. Pan (2019). Identification and characterisation of the novel endogenous promoter HASP1 and its signal peptide from Phaeodactylum tricornutum. Sci Rep 9(1): 9941.
Google Scholar: Author Only Title Only Author and Title

Falciatore, A., R. Casotti, C. Leblanc, C. Abrescia and C. Bowler (1999). Transformation of Nonselectable Reporter Genes in Marine Diatoms. Mar Biotechnol (NY) 1(3): 239-251.
Google Scholar: Author Only Title Only Author and Title

Folch, J., M. Lees and G. H. S. Stanley (1957). A simple method for the isolation and purification of total lipids from animal tissues. J Biol Chem 226(1): 497-509.
Google Scholar: Author Only Title Only Author and Title

Friedlingstein, P., M. W. Jones, M. O'Sullivan, R. M. Andrew, D. C. Bakker, J. Hauck, C. Le Quéré, G. P. Peters, W. Peters and J. Pongratz (2022). Global carbon budget 2021. Earth System Science Data 14(4): 1917-2005.
Google Scholar: Author Only Title Only Author and Title

Fukasawa, Y., J. Tsuji, S. C. Fu, K. Tomii, P. Horton and K. Imai (2015). MitoFates: improved prediction of mitochondrial targeting sequences and their cleavage sites. Mol Cell Proteom 14(4): 1113-1126.
Google Scholar: Author Only Title Only Author and Title

Fukayama, H., C. Masumoto, Y. Taniguchi, A. Baba-Kasai, Y. Katoh, H. Ohkawa and M. Miyao (2015). Characterization and expression analyses of two plastidic enolase genes in rice. Biosci Biotechnol Biochem 79(3): 402-409.
Google Scholar: Author Only Title Only Author and Title

Fuss, J., O. Liegmann, K. Krause and S. A. Rensing (2013). Green Targeting Predictor and Ambiguous Targeting Predictor 2: the pitfalls of plant protein targeting prediction and of transient protein expression in heterologous systems. New Phytol 200: 1022-1033.
Google Scholar: Author Only Title Only Author and Title

Gachon, C. M. M., S. Heesch, F. C. Kuepper, U. E. M. Achilles-Day, D. Brennan, C. N. Campbell, A. Clarke, R. G. Dorrell, J. Field, S. Gontarek, C. R. Menendez, R. J. Saxon, A. Veszelovszki, M. D. Guiry, K. Gharbi, M. Blaxter and J. G. Day (2013). The CCAP KnowledgeBase: linking protistan and cyanobacterial biological resources with taxonomic and molecular data. Systemat Biodiv 11(4): 407-413.
Google Scholar: Author Only Title Only Author and Title

Gilbertson, R., E. Langan and T. Mock (2022). Diatoms and their microbiomes in complex and changing polar oceans. Front Microbiol 13: 786764.
Google Scholar: Author Only Title Only Author and Title

Gorbunov, M. Y., E. Shirsin, E. Nikonova, V. V. Fadeev and P. G. Falkowski (2020). A multi-spectral fluorescence induction and relaxation (FIRe) technique for physiological and taxonomic analysis of phytoplankton communities. Mar Ecol Prog Series 644: 1-13.
Google Scholar: Author Only Title Only Author and Title

Grigoriev, I. V., R. D. Hayes, S. Calhoun, B. Kamel, A. Wang, S. Ahrendt, S. Dusheyko, R. Nikitin, S. J. Mondo, A. Salamov, I. Shabalov and A. Kuo (2021). PhycoCosm, a comparative algal genomics resource. Nucleic Acids Res 49(D1): D1004-D1011.
Google Scholar: Author Only Title Only Author and Title

Gruber, A., G. Rocap, P. G. Kroth, E. V. Armbrust and T. Mock (2015). Plastid proteome prediction for diatoms and other algae with secondary plastids of the red lineage. Plant J 81(3): 519-528.
Google Scholar: Author Only Title Only Author and Title

Gschloessl, B., Y. Guermeur and J. M. Cock (2008). HECTAR: a method to predict subcellular targeting in heterokonts. BMC Bioinformatics 9: 393.
Google Scholar: Author Only Title Only Author and Title

Hannaert, V., M.A. Albert, D.J. Ridgen, M.T. da Silva Giotto, O. Thiemann, R.C. Garratt, J. Van Roy, F. R. Opperdoes and P.A.M. Michels. Kinetic characterization, structure modelling studies and crystallization of Trypanosoma brucei enolase. Eur J Biochem 270, 3205-3213.
Google Scholar: Author Only Title Only Author and Title

Hartley, J. L., G. F. Temple and M. A. Brasch (2000). DNA cloning using in vitro site-specific recombination. Genome Res 10(11): 1788-1795.
Google Scholar: Author Only Title Only Author and Title

Hippmann, A. A., N. Schuback, K.-M. Moon, J. P. McCrow, A. E. Allen, L. F. Foster, B. R. Green and M. T. Maldonado (2022). Proteomic analysis of metabolic pathways supports chloroplast–mitochondria cross-talk in a Cu-limited diatom. Plant Direct 6(1): e376.
Google Scholar: Author Only Title Only Author and Title

Horton, P., K. J. Park, T. Obayashi, N. Fujita, H. Harada, C. J. Adams-Collier and K. Nakai (2007). WoLF PSORT: protein localization predictor. Nucl Acids Res 35: W585-W587.
Google Scholar: Author Only Title Only Author and Title

Huang, A., L. Liu, C. Yang and G. Wang (2015). Phaeodactylum tricornutum photorespiration takes part in glycerol metabolism and is important for nitrogen-limited response. Biotechnol Biofuels 8(1): 1-16.
Google Scholar: Author Only Title Only Author and Title

Huang, T., Y. Pan, E. Maréchal and H. Hu (2024). Proteomes reveal the lipid metabolic network in the complex plastid of Phaeodactylum tricornutum. Plant J 117: 385-403.
Google Scholar: Author Only Title Only Author and Title

Initiative, O. T. P. T. (2019). One thousand plant transcriptomes and the phylogenomics of green plants. Nature 574(7780): 679-685.
 Google Scholar: Author Only Title Only Author and Title

Jassby, A. D. and T. Platt (1976). Mathematical formulation of the relationship between photosynthesis and light for phytoplankton. Limnol Oceanograph 21(4): 540-547.
 Google Scholar: Author Only Title Only Author and Title

Jiang, Y., T. Cao, Y. Yang, H. Zhang, J. Zhang and X. Li (2023). A chlorophyll c synthase widely co-opted across phytoplankton. Science 382(6666): 92-98.
 Google Scholar: Author Only Title Only Author and Title

Joli, N., L. Concia, K. Mocaer, J. Guterman, J. Laude, S. Guerin, T. Sciandra, F. Bruyant, O. Ait-Mohamed, M. Beguin, M.-H. Forget, C. Bourbousse, T. Lacour, B. Bailleul, C. Nef, M. Savoie, J.-E. Tremblay, D. A. Campbell, J. Lavaud, Y. Schwab, M. Babin and C. Bowler (2024). Hypometabolism to survive the long polar night and subsequent successful return to light in the diatom Fragilariopsis cylindrus. New Phytol 241(2193-2208).
 Google Scholar: Author Only Title Only Author and Title

Jones, P., D. Binns, H. Y. Chang, M. Fraser, W. Li, C. McAnulla, H. McWilliam, J. Maslen, A. Mitchell, G. Nuka, S. Pesseat, A. F. Quinn, A. Sangrador-Vegas, M. Scheremetjew, S. Y. Yong, R. Lopez and S. Hunter (2014). InterProScan 5: genome-scale protein function classification. Bioinformatics 30(9): 1236-1240.
 Google Scholar: Author Only Title Only Author and Title

Jouhet, J., J. Lupette, O. Clerc, L. Magneschi, M. Bedhomme, S. Collin, S. Roy, E. Maréchal and F. Rébeillé (2017). LC-MS/MS versus TLC plus GC methods: Consistency of glycerolipid and fatty acid profiles in microalgae and higher plant cells and effect of a nitrogen starvation. PLoS One 12(8): e0182423.
 Google Scholar: Author Only Title Only Author and Title

Jouhet, J., E. Maréchal, R. Bligny, J. Joyard and M. A. Block (2003). Transient increase of phosphatidylcholine in plant cells in response to phosphate deprivation. FEBS Lett 544(1): 63-68.
 Google Scholar: Author Only Title Only Author and Title

Kassambara, A. and F. Mundt (2017). Package 'factoextra'. Extract and visualize the results of multivariate data analyses 76(2).
 Google Scholar: Author Only Title Only Author and Title

Katoh, K., J. Rozewicki and K. D. Yamada (2017). MAFFT online service: multiple sequence alignment, interactive sequence choice and visualization. Brief Bioinform 20: 1160-1166.
 Google Scholar: Author Only Title Only Author and Title

Kazamia, E., R. Sutak, J. Paz-Yepes, R. G. Dorrell, F. R. J. Vieira, J. Mach, J. Morrissey, S. Leon, F. Lam, E. Pelletier, J. M. Camadro, C. Bowler and E. Lesuisse (2018). Endocytosis-mediated siderophore uptake as a strategy for Fe acquisition in diatoms. Sci Adv 4(5): eaar4536.
 Google Scholar: Author Only Title Only Author and Title

Kearse, M., R. Moir, A. Wilson, S. Stones-Havas, M. Cheung, S. Sturrock, S. Buxton, A. Cooper, S. Markowitz, C. Duran, T. Thierer, B. Ashton, P. Meintjes and A. Drummond (2012). Geneious Basic: An integrated and extendable desktop software platform for the organization and analysis of sequence data. Bioinform 28(12): 1647-1649.
 Google Scholar: Author Only Title Only Author and Title

Keeling, P. J., F. Burki, H. M. Wilcox, B. Allam, E. E. Allen, L. A. Amaral-Zettler, E. V. Armbrust, J. M. Archibald, A. K. Bharti, C. J. Bell, B. Beszteri, K. D. Bidle, C. T. Cameron, L. Campbell, D. A. Caron, R. A. Cattolico, J. L. Collier, K. Coyne, S. K. Davy, P. Deschamps, S. T. Dyhrman, B. Edvardsen, R. D. Gates, C. J. Gobler, S. J. Greenwood, S. M. Guida, J. L. Jacobi, K. S. Jakobsen, E. R. James, B. Jenkins, U. John, M. D. Johnson, A. R. Juhl, A. Kamp, L. A. Katz, R. Kiene, A. Kudryavtsev, B. S. Leander, S. Lin, C. Lovejoy, D. Lynn, A. Marchetti, G. McManus, A. M. Nedelcu, S. Menden-Deuer, C. Miceli, T. Mock, M. Montresor, M. A. Moran, S. Murray, G. Nadathur, S. Nagai, P. B. Ngam, B. Palenik, J. Pawlowski, G. Petroni, G. Piganeau, M. C. Posewitz, K. Rengefors, G. Romano, M. E. Rumpho, T. Rynearson, K. B. Schilling, D. C. Schroeder, A. G. Simpson, C. H. Slamovits, D. R. Smith, G. J. Smith, S. R. Smith, H. M. Sosik, P. Stief, E. Theriot, S. N. Twary, P. E. Umale, D. Vaulot, B. Wawrik, G. L. Wheeler, W. H. Wilson, Y. Xu, A. Zingone and A. Z. Worden (2014). The Marine Microbial Eukaryote Transcriptome Sequencing Project (MMETSP): illuminating the functional diversity of eukaryotic life in the oceans through transcriptome sequencing. PLoS Biol 12(6): e1001889.
 Google Scholar: Author Only Title Only Author and Title

Kopka, J., N. Schauer, S. Krueger, C. Birkemeyer, B. Usadel, E. Bergmüller, P. Dörmann, W. Weckwerth, Y. Gibon, M. Stitt, L. Willmitzer, A. R. Fernie and D. Steinhauser (2005). GMD@CSB.DB: the Golm Metabolome Database. Bioinformatics 21(8): 1635-1638.
 Google Scholar: Author Only Title Only Author and Title

Krebs, H. A. (1963). Renal gluconeogenesis. Adv Enzyme Regul 1: 385-400.
 Google Scholar: Author Only Title Only Author and Title

Kroth, P. G., A. Chiovitti, A. Gruber, V. Martin-Jezequel, T. Mock, M. S. Parker, M. S. Stanley, A. Kaplan, L. Caron, T. Weber, U.

Maheswari, E. V. Armbrust and C. Bowler (2008). A model for carbohydrate metabolism in the diatom Phaeodactylum tricornutum deduced from comparative whole genome analysis. PLoS One 3(1): e1426.
  Google Scholar: Author Only Title Only Author and Title

Lataretu, M. and M. Hölzer (2020). RNAflow: an effective and simple RNA-Seq differential gene expression pipeline using Nextflow. Genes (Basel) 11(12).
  Google Scholar: Author Only Title Only Author and Title

Lepetit, B., D. A. Campbell, J. Lavaud, C. Büchel, R. Goss and B. Bailleul (2022). Photosynthetic Light Reactions in diatoms. II. The dynamic regulation of the various light reactions. The Molecular Life of Diatoms. A. Falciatore and T. Mock. Cham, Springer International Publishing: 423-464.
  Google Scholar: Author Only Title Only Author and Title

Levering, J., J. Broddrick, C. L. Dupont, G. Peers, K. Beeri, J. Mayers, A. A. Gallina, A. E. Allen, B. O. Palsson and K. Zengler (2016). Genome-scale model reveals metabolic basis of biomass partitioning in a model diatom. Plos One 11(5), 0155038.
  Google Scholar: Author Only Title Only Author and Title

Lisec, J., N. Schauer, J. Kopka, L. Willmitzer and A. R. Fernie (2006). Gas chromatography mass spectrometry–based metabolite profiling in plants. Nat Protocol 1(1): 387-396.
  Google Scholar: Author Only Title Only Author and Title

Liu, S., M. Storti, C. Bowler, G. Finazzi and R. G. Dorrell (2022). A metabolic, phylogenomic and environmental atlas of diatom plastid transporters from the model species Phaeodactylum. Front Plant Sci 13, 950467.
  Google Scholar: Author Only Title Only Author and Title

Liu, S., Z. Wang, R. Zhu, F. Wang, Y. Cheng and Y. Liu (2021). Three Differential Expression Analysis Methods for RNA Sequencing: limma, EdgeR, DESeq2. J Vis Exp(175).
  Google Scholar: Author Only Title Only Author and Title

Lovejoy, C., W. F. Vincent, S. Bonilla, S. Roy, M. J. Martineau, R. Terrado, M. Potvin, R. Massana and C. Pedros-Alio (2007). Distribution, phylogeny, and growth of cold-adapted picoprasinophytes in Arctic seas. J Phycol 43(1): 78-89.
  Google Scholar: Author Only Title Only Author and Title

Luedemann, A., L. von Malotky, A. Erban and J. Kopka (2012). TagFinder: preprocessing software for the fingerprinting and the profiling of gas chromatography-mass spectrometry based metabolome analyses. Methods Mol Biol 860: 255-286.
  Google Scholar: Author Only Title Only Author and Title

Malviya, S., E. Scalco, S. Audic, F. Vincent, A. Veluchamy, J. Poulain, P. Wincker, D. Iudicone, C. de Vargas, L. Bittner, A. Zingone and C. Bowler (2016). Insights into global diatom distribution and diversity in the world's ocean. Proc Natl Acad Sci USA 113(11): 1516-1525.
  Google Scholar: Author Only Title Only Author and Title

Maréchal, E. and J. Lupette (2020). Relationship between acyl-lipid and sterol metabolisms in diatoms. Biochimie 169: 3-11.
  Google Scholar: Author Only Title Only Author and Title

McCarthy, J. K., S. R. Smith, J. P. McCrow, M. Tan, H. Zheng, K. Beeri, R. Roth, C. Lichtle, U. Goodenough, C. P. Bowler, C. L. Dupont and A. E. Allen (2017). Nitrate Reductase knockout uncouples nitrate transport from nitrate assimilation and drives repartitioning of carbon flux in a model pennate diatom. Plant Cell 29(8): 2047-2070.
  Google Scholar: Author Only Title Only Author and Title

Miller, M. A., T. Schwartz, B. E. Pickett, S. He, E. B. Klem, R. H. Scheuermann, M. Passarotti, S. Kaufman and M. A. O'Leary (2015). A RESTful API for access to phylogenetic tools via the CIPRES Science Gateway. Evol Bioinform Online 11: 43-48.
  Google Scholar: Author Only Title Only Author and Title

Mistry, J., S. Chuguransky, L. Williams, M. Qureshi, G. A. Salazar, E. L. L. Sonnhammer, S. C. E. Tosatto, L. Paladin, S. Raj, L. J. Richardson, R. D. Finn and A. Bateman (2020). PFAM: the protein families database in 2021. Nucleic Acids Res.
  Google Scholar: Author Only Title Only Author and Title

Moog, D., A. Nozawa, Y. Tozawa and R. Kamikawa (2020). Substrate specificity of plastid phosphate transporters in a non-photosynthetic diatom and its implication in evolution of red alga-derived complex plastids. Sci Rep 10(1): 1167.
  Google Scholar: Author Only Title Only Author and Title

Moog, D., S. A. Rensing, J. M. Archibald, U. G. Maier and K. K. Ullrich (2015). Localization and evolution of putative triose phosphate translocators in the diatom Phaeodactylum tricornutum. Genom Biol Evol 7(11): 2955-2969.
  Google Scholar: Author Only Title Only Author and Title

Murik, O., L. Tirichine, J. Prihoda, Y. Thomas, W. L. Araújo, A. E. Allen, A. R. Fernie and C. Bowler (2019). Downregulation of mitochondrial alternative oxidase affects chloroplast function, redox status and stress response in a marine diatom. New Phytol 221(3): 1303-1316.
  Google Scholar: Author Only Title Only Author and Title

Nash, E. A., A. C. Barbrook, R. K. Edwards-Stuart, K. Bernhardt, C. J. Howe and R. E. R. Nisbet (2007). Organization of the mitochondrial genome in the dinoflagellate Amphidinium carterae. Mol Biol Evol 24(7): 1528-1536.
Google Scholar: Author Only Title Only Author and Title

Nawaly, H., H. Matsui, Y. Tsuji, K. Iwayama, H. Ohashi, K. Nakajima and Y. Matsuda (2023). Multiple plasma membrane SLC4s contribute to external HCO3– acquisition during CO2 starvation in the marine diatom Phaeodactylum tricornutum. J Exp Bot 74(1): 296-307.
Google Scholar: Author Only Title Only Author and Title

Nonoyama, T., E. Kazamia, H. Nawaly, X. Gao, Y. Tsuji, Y. Matsuda, C. Bowler, T. Tanaka and R. G. Dorrell (2019). Metabolic innovations underpinning the origin and diversification of the diatom chloroplast. Biomolecules 9(8), 484.
Google Scholar: Author Only Title Only Author and Title

Nymark, M., A. K. Sharma, T. Sparstad, A. M. Bones and P. Winge (2016). A CRISPR/Cas9 system adapted for gene editing in marine algae. Sci Rep 6: 24951.
Google Scholar: Author Only Title Only Author and Title

Pesant, S., F. Not, M. Picheral, S. Kandels-Lewis, N. Le Bescot, G. Gorsky, D. Iudicone, E. Karsenti, S. Speich, R. Trouble, C. Dimier, S. Searson and C. Tara Oceans (2015). Open science resources for the discovery and analysis of Tara Oceans data. Sci Data 2.
Google Scholar: Author Only Title Only Author and Title

Pierella Karlusich, J. J., C. Nef, C. Bowler and R. Dorrell (2023). Modèles biogéographiques et génomes des photoautotrophes aquatiques: 45-82.

Popko, J., C. Herrfurth, K. Feussner, T. Ischebeck, T. Iven, R. Haslam, M. Hamilton, O. Sayanova, J. Napier, I. Khozin-Goldberg and I. Feussner (2016). Metabolome analysis reveals betaine lipids as major source for triglyceride formation, and the accumulation of sedoheptulose during nitrogen-starvation of Phaeodactylum tricornutum. PLoS One 11(10): e0164673.
Google Scholar: Author Only Title Only Author and Title

Prabhakar, V., T. Löttgert, T. Gigolashvili, K. Bell, U. I. Flügge and R. E. Häusler (2009). Molecular and functional characterization of the plastid-localized phosphoenolpyruvate enolase (ENO1) from Arabidopsis thaliana. FEBS Lett 583(6): 983-991.
Google Scholar: Author Only Title Only Author and Title

Raines, C. A. (2003). The Calvin Cycle revisited. Photosynth Res 75(1): 1-10.
Google Scholar: Author Only Title Only Author and Title

Rainteau, D., L. Humbert, E. Delage, C. Vergnolle, C. Cantrel, M.-A. Maubert, S. Lanfranchi, R. Maldiney, S. Collin, C. Wolf, A. Zachowski and E. Ruelland (2012). Acyl chains of phospholipase D transphosphatidylation products in Arabidopsis cells: a study using multiple reaction monitoring mass spectrometry. PLoS One 7(7): e41985.
Google Scholar: Author Only Title Only Author and Title

Rastogi, A., U. Maheswari, R. G. Dorrell, F. R. J. Vieira, F. Maumus, A. Kustka, J. McCarthy, A. E. Allen, P. Kersey, C. Bowler and L. Tirichine (2018). Integrative analysis of large scale transcriptome data draws a comprehensive landscape of Phaeodactylum tricornutum genome and evolutionary origin of diatoms. Sci Rep 8(1): 4834.
Google Scholar: Author Only Title Only Author and Title

Rastogi, A., O. Murik, C. Bowler and L. Tirichine (2016). PhytoCRISP-Ex: a web-based and stand-alone application to find specific target sequences for CRISPR/CAS editing. BMC Bioinform 17(1): 261.
Google Scholar: Author Only Title Only Author and Title

Rastogi, A., F. R. J. Vieira, A. F. Deton-Cabanillas, A. Veluchamy, C. Cantrel, G. Wang, P. Vanormelingen, C. Bowler, G. Piganeau, H. Hu and L. Tirichine (2020). A genomics approach reveals the global genetic polymorphism, structure, and functional diversity of ten accessions of the marine model diatom Phaeodactylum tricornutum. ISME J 14(2): 347-363.
Google Scholar: Author Only Title Only Author and Title

Reinoso, R. F., B. A. Telfer and M. Rowland (1997). Tissue water content in rats measured by desiccation. J Pharmacol Toxicol Methods 38(2): 87-92.
Google Scholar: Author Only Title Only Author and Title

Royo-Llonch, M., P. Sánchez, C. Ruiz-González, G. Salazar, C. Pedrós-Alió, K. Labadie, L. Paoli, C. Tara Oceans, S. Chaffron, D. Eveillard, E. Karsenti, S. Sunagawa, P. Wincker, L. Karp-Boss, C. Bowler and S. G. Acinas (2021). Compendium of 530 metagenome-assembled bacterial and archaeal genomes from the polar Arctic Ocean. Nat Microbiol 2021: 1561-1574.
Google Scholar: Author Only Title Only Author and Title

Rider, CC. and C.B. Taylor, Enolase isoenzymes in rat tissues: electrophoretic, chromatographic, immunological and kinetic properties. Biochim Biophys Acta 365(1): 285-300.

Río Bártulos, C., M. B. Rogers, T. A. Williams, E. Gentekaki, H. Brinkmann, R. Cerff, M. F. Liaud, A. B. Hehl, N. R. Yarlett, A. Gruber, P. G. Kroth and M. van der Giezen (2018). Mitochondrial Glycolysis in a Major Lineage of Eukaryotes. Genom Biol Evol

10(9): 2310-2325.
Google Scholar: Author Only Title Only Author and Title

Sachse, M., S. Sturm, A. Gruber and P. Kroth (2013). Identification and evaluation of endogenous reference genes for steady state transcript quantification by qPCR in the diatom Phaeodactylum tricornutum with constitutive expression independent from time and light. Endocytobiosis Cell Res 24: 7.
Google Scholar: Author Only Title Only Author and Title

Scialdone, A., S. T. Mugford, D. Feike, A. Skeffington, P. Borrill, A. Graf, A. M. Smith and M. Howard (2013). Arabidopsis plants perform arithmetic division to prevent starvation at night. eLife 2: e00669.
Google Scholar: Author Only Title Only Author and Title

Scrutton, M. C. and M. F. Utter (1968). The Regulation of Glycolysis and Gluconeogenesis in Animal Tissues. Annu Rev Biochem 37(1): 249-302.
Google Scholar: Author Only Title Only Author and Title

Serôdio, J. and J. Lavaud (2011). A model for describing the light response of the nonphotochemical quenching of chlorophyll fluorescence. Photosynth Res 108(1): 61-76.
Google Scholar: Author Only Title Only Author and Title

Shtaida, N., I. Khozin-Goldberg and S. Boussiba (2015). The role of pyruvate hub enzymes in supplying carbon precursors for fatty acid synthesis in photosynthetic microalgae. Photosynth Res 125(3): 407-422.
Google Scholar: Author Only Title Only Author and Title

Siegel, P., K. G. Baker, E. Low-Décarie and R. J. Geider (2020). High predictability of direct competition between marine diatoms under different temperatures and nutrient states. Ecol Evol 10(14): 7276-7290.
Google Scholar: Author Only Title Only Author and Title

Smith, S. R., R. M. Abbriano and M. Hildebrand (2012). Comparative analysis of diatom genomes reveals substantial differences in the organization of carbon partitioning pathways. Algal Res 1(1): 2-16.
Google Scholar: Author Only Title Only Author and Title

Smith, S. R., C. L. Dupont, J. K. McCarthy, J. T. Broddrick, M. Oborník, A. Horák, Z. Füssy, J. Cihlář, S. Kleessen, H. Zheng, J. P. McCrow, K. K. Hixson, W. L. Araújo, A. Nunes-Nesi, A. Fernie, Z. Nikoloski, B. O. Palsson and A. E. Allen (2019). Evolution and regulation of nitrogen flux through compartmentalized metabolic networks in a marine diatom. Nat Commun 10(1): 4552.
Google Scholar: Author Only Title Only Author and Title

Smith, S. R., J. T. Gillard, A. B. Kustka, J. P. McCrow, J. H. Badger, H. Zheng, A. M. New, C. L. Dupont, T. Obata, A. R. Fernie and A. E. Allen (2016). Transcriptional orchestration of the global cellular response of a model pennate diatom to diel light cycling under iron limitation. PLoS Genet 12(12): e1006490.
Google Scholar: Author Only Title Only Author and Title

Spitzer, M., J. Wildenhain, J. Rappsilber and M. Tyers (2014). BoxPlotR: a web tool for generation of box plots. Nat Methods 11(2): 121-122.
Google Scholar: Author Only Title Only Author and Title

Stamatakis, A. (2014). RAxML version 8: a tool for phylogenetic analysis and post-analysis of large phylogenies. Bioinformatics 30(9): 1312-1313.
Google Scholar: Author Only Title Only Author and Title

Strassert, J. F. H., I. Irisarri, T. A. Williams and F. Burki (2021). A molecular timescale for eukaryote evolution with implications for the origin of red algal-derived plastids. Nat Commun 12(1): 1879.
Google Scholar: Author Only Title Only Author and Title

Sutherland, E. W., T. Posternak and C. F. Cori (1949). Mechanism of the phosphoglyceric mutase reaction. J Biol Chem 181(1): 153-159.
Google Scholar: Author Only Title Only Author and Title

Tanaka, R. and A. Tanaka (2007). Tetrapyrrole biosynthesis in higher plants. Annu Rev Plant Biol 58: 321-346.
Google Scholar: Author Only Title Only Author and Title

Tardif, M., A. Atteia, M. Specht, G. Cogne, N. Rolland, S. Brugière, M. Hippler, M. Ferro, C. Bruley, G. Peltier, O. Vallon and L. Cournac (2012). PredAlgo: a new subcellular localization prediction tool dedicated to green algae. Mol Biol Evol 29(12): 3625-3639.
Google Scholar: Author Only Title Only Author and Title

Troncoso-Ponce, M. A., J. Rivoal, S. Dorion, R. Sánchez, M. Venegas-Calerón, A. J. Moreno-Pérez, S. Baud, R. Garcés and E. Martínez-Force (2018). Molecular and biochemical characterization of the sunflower (Helianthus annuus L.) cytosolic and plastidial enolases in relation to seed development. Plant Sci 272: 117-130.
Google Scholar: Author Only Title Only Author and Title

Uwizeye, C., J. Decelle, P. Jouneau, B. Gallet, J. Keck, C. Moriscot, F. Chevalier, N. Schieber, R. Templin, G. Curien, Y. Schwab, G. Schoehn, S. C. Zeeman, D. Falconet and G. Finazzi (2020). Morphological bases of phytoplankton energy management and physiological responses unveiled by 3D subcellular imaging. Nat Commun 12: 1à49.
  Google Scholar: Author Only Title Only Author and Title

Worden, A. Z., J. H. Lee, T. Mock, P. Rouze, M. P. Simmons, A. L. Aerts, A. E. Allen, M. L. Cuvelier, E. Derelle, M. V. Everett, E. Foulon, J. Grimwood, H. Gundlach, B. Henrissat, C. Napoli, S. M. McDonald, M. S. Parker, S. Rombauts, A. Salamov, P. Von Dassow, J. H. Badger, P. M. Coutinho, E. Demir, I. Dubchak, C. Gentemann, W. Eikrem, J. E. Gready, U. John, W. Lanier, E. A. Lindquist, S. Lucas, K. F. X. Mayer, H. Moreau, F. Not, R. Otillar, O. Panaud, J. Pangilinan, I. Paulsen, B. Piegu, A. Poliakov, S. Robbens, J. Schmutz, E. Toulza, T. Wyss, A. Zelensky, K. Zhou, E. V. Armbrust, D. Bhattacharya, U. W. Goodenough, Y. Van de Peer and I. V. Grigoriev (2009). Green evolution and dynamic adaptations revealed by genomes of the marine picoeukaryotes Micromonas. Science 324(5924): 268-272.
  Google Scholar: Author Only Title Only Author and Title

Yang, L., Z. Wang, A. Zhang, R. Bhawal, C. Li, S. Zhang, L. Cheng and J. Hua (2022). Reduction of the canonical function of a glycolytic enzyme enolase triggers immune responses that further affect metabolism and growth in Arabidopsis. Plant Cell 34(5): 1745-1767.
  Google Scholar: Author Only Title Only Author and Title

Ye, J., G. Coulouris, I. Zaretskaya, I. Cutcutache, S. Rozen and T. L. Madden (2012). Primer-BLAST: a tool to design target-specific primers for polymerase chain reaction. BMC Bioinform 13: 134.
  Google Scholar: Author Only Title Only Author and Title

Yin, W. and H. Hu (2023). CRISPR/Cas9-Mediated Genome Editing via Homologous Recombination in a Centric Diatom Chaetoceros muelleri. ACS Synth Biol 12(4): 1287-1296.
  Google Scholar: Author Only Title Only Author and Title

Young, E. F. and J. T. Holt (2007). Prediction and analysis of long-term variability of temperature and salinity in the Irish Sea. J Geophys Res 112(C1).
  Google Scholar: Author Only Title Only Author and Title

Yu, G., K. Nakajima, A. Gruber, C. Rio Bartulos, A. F. Schober, B. Lepetit, E. Yohannes, Y. Matsuda and P. G. Kroth (2022). Mitochondrial phosphoenolpyruvate carboxylase contributes to carbon fixation in the diatom Phaeodactylum tricornutum at low inorganic carbon concentrations. New Phytol 235: 1379-1393.
  Google Scholar: Author Only Title Only Author and Title

Zhang, Y., A. Sampathkumar, S. M.-L. Kerber, C. Swart, C. Hille, K. Seerangan, A. Graf, L. Sweetlove and A. R. Fernie (2020). A moonlighting role for enzymes of glycolysis in the co-localization of mitochondria and chloroplasts. Nat Commun 11(1): 4509.
  Google Scholar: Author Only Title Only Author and Title

Zhao, Z. and S. M. Assmann (2011). The glycolytic enzyme, phosphoglycerate mutase, has critical roles in stomatal movement, vegetative growth, and pollen production in Arabidopsis thaliana. J Exp Bot 62(14): 5179-5189.
  Google Scholar: Author Only Title Only Author and Title

Zheng, Y. T., A. H. Quinn and G. Sriram (2013). Experimental evidence and isotopomer analysis of mixotrophic glucose metabolism in the marine diatom Phaeodactylum tricornutum. Microbial Cell Factories 12: 16.
  Google Scholar: Author Only Title Only Author and Title

Zhu, B.-H., H.-P. Shi, G.-P. Yang, N.-N. Lv, M. Yang and K.-H. Pan (2016). Silencing UDP-glucose pyrophosphorylase gene in Phaeodactylum tricornutum affects carbon allocation. New Biotechnol 33(1): 237-244.
  Google Scholar: Author Only Title Only Author and Title

Zulu, N. N., K. Zienkiewicz, K. Vollheyde and I. Feussner (2018). Current trends to comprehend lipid metabolism in diatoms. Progr Lipid Res 70: 1-16.
  Google Scholar: Author Only Title Only Author and Title